3-2022

Determination of Nonlinear Optical Properties for Gallium Arsenide Phosphide Ternary Compounds and for Tin Thiohypodiphosphate

Peter F. Norris

DETERMINATION OF NONLINEAR OPTICAL PROPERTIES FOR GALLIUM ARSENIDE PHOSPHIDE TERNARY COMPOUNDS AND FOR TIN THIOHYPODIPHOSPHATE

THESIS

Peter F Norris, Captain, USSF

AFIT-ENG-MS-22-M-051

DEPARTMENT OF THE AIR FORCE
AIR UNIVERSITY

AIR FORCE INSTITUTE OF TECHNOLOGY

Wright-Patterson Air Force Base, Ohio

AFIT-ENG-MS-22-M-051

DETERMINATION OF NONLINEAR OPTICAL PROPERTIES FOR GALLIUM ARSENIDE PHOSPHIDE TERNARY COMPOUNDS AND FOR TIN THIOHYPODIPHOSPHATE

THESIS

Presented to the Faculty

Department of Electrical and Computer Engineering

Graduate School of Engineering and Management

Air Force Institute of Technology

Air University

Air Education and Training Command

in Partial Fulfillment of the Requirements for the

Degree of Master of Science in Electrical Engineering

Peter F Norris, B.S.E.E.

Captain, USSF

March 24, 2022

AFIT-ENG-MS-22-M-051

DETERMINATION OF NONLINEAR OPTICAL PROPERTIES FOR GALLIUM ARSENIDE PHOSPHIDE TERNARY COMPOUNDS AND FOR TIN THIOHYPODIPHOSPHATE

THESIS

Peter F Norris, B.S.E.E.
Captain, USSF

Committee Membership:

Lt Col James M Sattler, Ph.D.
Chair

Rita D Peterson, Ph.D.
Member

Jonathan W Evans, Ph.D.
Member

Acknowledgements

These eighteen months at AFIT have been quite a ride, full of joy, sorrows, late nights, and relaxing days. While I may not have gotten the results I wanted, I am grateful for all the experience I gained, thanks in large part to following individuals.

I first will give thanks to God for giving me the strength and perseverance to come out in the end with my thesis completed. Next, I sincerely thank Lt Col James Sattler for accepting me as his student. He allowed me the opportunity to pursue the work in this thesis which I otherwise may not have gotten. I am very appreciative of the help and guidance from Dr. Rita Peterson, who provided the topic of this thesis along with the lab, materials, and knowledge to help me through. I am indebted to Dr. Jonathan Evans for showing up to AFIT weeks before the Summer Quarter to teach me nonlinear optics, a subject I had no prior knowledge of before AFIT. And then there is Joel Murray; I am grateful for the code he provided and I used in this thesis, and for the hours he spent helping me determine how I managed to mess up his code.

Now it is time to acknowledge and deeply thank the ones at home who were my motivation throughout this journey. My wife had to watch our daughter, then daughters, many nights as I spent doing classwork or thesis writing on the computer. My oldest had to be torn away from me crying too often since I was not always there to play with her. And my youngest and new arrival − your smiles always make me happy and give me the motivation to keep on going.

Peter F Norris

AFIT-ENG-MS-22-M-051

Abstract

The Department of Defense and the commercial sector rely on coherent light sources to emit light that transmits through the atmosphere. Nonlinear optical effects in crystalline materials can be used to generate the laser waves, but certain nonlinear effects negatively impact the performance of laser generating materials. This thesis focuses on characterizing nonlinear optical properties for gallium arsenide phosphide ternary compounds and for tin thiohypodiphosphate. The Maker Fringe experiment is used to determine the d-coefficients of the materials, which describe the magnitude of the nonlinear response of the material. The Z-Scan experiment is used to calculate the nonlinear refractive index and the two photon absorption of the material. This thesis summarizes the pertinent theory surrounding nonlinear optics and the characterization experiments. The Maker Fringe experiment was constructed and verified as a part of this thesis, allowing the setup to be used for future research. The gallium arsenide phosphide ternary compounds were demonstrated to be able to frequency convert from 2090 nm to 1045 nm. Tin thiohypodisphosphate was demonstrated to not have appreciable two photon absorption at 1550 nm.

Table of Contents

Page

Page

List of Figures

Figure Page

List of Tables

DETERMINATION OF NONLINEAR OPTICAL PROPERTIES FOR GALLIUM ARSENIDE PHOSPHIDE TERNARY COMPOUNDS AND FOR TIN THIOHYPODIPHOSPHATE

I. Introduction

1.1 Problem Background

The Department of Defense (DoD) is reliant on long-distance laser transmission through the atmosphere for communications, countermeasures, and other applications. To keep the combat edge, the military needs to constantly improve current technologies. One way to improve current laser technology is to discover new gain media for the laser light generation, which could allow for more efficient or higher power lasers. This thesis will primarily focus on a group of materials intended to improve upon gallium arsenide (GaAs) and gallium phosphide (GaP) as gain media for infrared wavelengths shorter than 1800 nm. Additionally, this group of materials is sought for frequency conversion in the $3 - 5$ μm and possibly $8 - 12$ μm wavebands where laser sources are not as common as in the shorter wavebands This thesis will also reexamine another material for frequency conversion within the $3 - 5$ μm and $8 - 12$ μm wavebands.

One limiting factor for long-distance lasers is the atmospheric transmittance of light of differing wavelengths, as presented in Figure 1 for wavelengths shorter than 15 μm [1]. The molecules present in the atmosphere absorb certain wavelengths of light because those wavelengths match the molecule's resonance modes [2]. Thus, any laser needs to emit within one of the transmission wavebands to be viable as a

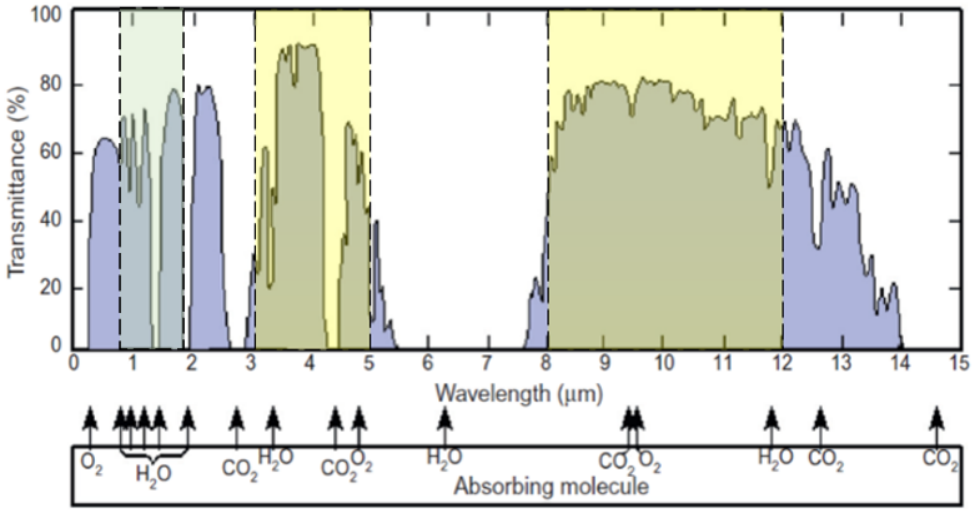

Figure 1: Atmospheric transmittance of light. This graph illustrates the transmittance of light based on wavelength below 15 μm. The highlighted regions are the desired output wavelengths for new coherent light sources. Additionally, it presents some of the molecules responsible for absorbing certain wavelengths of light. *This figure is modified from [1], adding the highlighted regions.*

long-distance laser.

Currently, there are many useful sources of laser light for the visible and short-wave IR (SWIR) wavebands ($0.4 - 0.7$ and $0.7 - 3$ μm); however, there are fewer usable sources for the mid-wave IR (MWIR) ($3 - 5$ μm) and long-wave IR (LWIR) ($8 - 12$ μm) wavebands [3]. Consequently, it is important to discover new optical emission sources for these wavebands as the atmospheric transmittance is high for most of these bands [1]. Such discoveries could prove vital to maintaining the combat edge or improving current communications technologies.

Nonlinear optical parametric generation is essential to producing the coherent light sources for use in long-distance laser transmission. Some materials have $\chi^{(2)}$ nonlinearity, explained in Chapter 2.1.2. Under the right conditions, $\chi^{(2)}$ materials will convert the input beam's frequency to a different frequency, though sometimes it requires two input beams [4]. The different processes of frequency conversion are listed here [4]:

- Sum Frequency Generation (SFG), where the output has a higher frequency than the inputs (SFG includes a special case called Second Harmonic Generation (SHG), where the output has twice the input's frequency);

- Difference Frequency Generation (DFG), where two higher frequency inputs generate a lower frequency output (DFG includes a special case is called Optical Parametric Amplification (OPA), where an input is amplified by a pump, producing a lower frequency idler);

- Optical Parametric Generation (OPG), where one higher frequency input generates two lower frequency outputs.

Of these processes, DFG is commonly used for frequency down conversion. The $\chi^{(2)}$ response of a material is summarized in a 3×6 matrix of d-coefficients. These d-coefficients completely characterize the dependence of the material's $\chi^{(2)}$ nonlinear response on the polarizations of the input and output beams [4]. These coefficients are the same for SFG as for DFG when the same wavelengths are used, since these processes can be shown to be the inverse of each other [4]. One way to determine some of these d-coefficients is with the Maker Fringe experiment, which is one of the two characterization experiments used in this thesis. The Maker Fringe experiment involves relating the intensity of a driving field to the SHG output intensity produced by the material to determine d-coefficients. The specific method used to implement the Maker Fringe experiment in this thesis is the Intensity-scan Method, which involves varying the intensity of the driving field instead of altering the position of the sample as done in the Rotation Method. These experiments will be explained in more detail in Chapter 2.2.1.

Along with $\chi^{(2)}$ nonlinearity, materials can also have $\chi^{(3)}$ nonlinear responses. The two $\chi^{(3)}$ responses of focus in this research are nonlinear refractive index n_2 and

nonlinear absorption β. Both of these responses increase in magnitude with increasing intensity of the light waves [4]. A change in n_2 changes the total refractive index of the material, which in turn alters the conditions for effective frequency conversion [4]. A larger β means that more multi-photon absorption is occurring, decreasing the amount of light transmitted at that frequency [4]. Both of these responses can be determined using the Z-Scan experiment, which is the second of the two experiments used in this thesis. The Z-Scan experiment involves moving the sample with the propagation of the beam through the beam's focus and comparing the intensity of the transmitted beam with a reference intensity. This is explained in more detail in Chapter 2.2.2.

Both the Maker Fringe and the Z-Scan experiments will be performed on a set ternary compounds formed from GaAs and GaP, taking the form $GaAs_xP_{1-x}$ where $0 < x < 1$. GaAs has a larger $\chi^{(2)}$ nonlinear response than GaP; however, GaAs has a larger β than GaP for wavelengths between 1000 and 1800 nm (see Figure 2) [5, 6, 7, 8, 9]. The ternaries are examined for viability in the $1 - 1.8$ μm waveband that GaAs is not viable due to its nonlinear absorption. The x value in $GaAs_xP_{1-x}$ is also examined to determine the relationship between the ratio of arsenic to phosphorus and the nonlinear optics (NLO) properties of the ternary compounds. The additional material examined in this thesis for use in the MWIR and LWIR wavebands is tin thiohypodiphosphate ($Sn_2P_2S_6$, called SPS). Due to its crystal structure, characterizing the d-coefficients of SPS is more complicated than for GaAs and GaP. SPS has had its d-coefficients characterized via the Maker Fringe Rotation Method by Haertle *et al.* [11]. Being able to recreate Haertle's results with the Maker Fringe Intensity-scan Method would allow crystals of similar composition and structure to have their d-coefficients accurate characterized to determine their viability as MWIR or LWIR lasers.

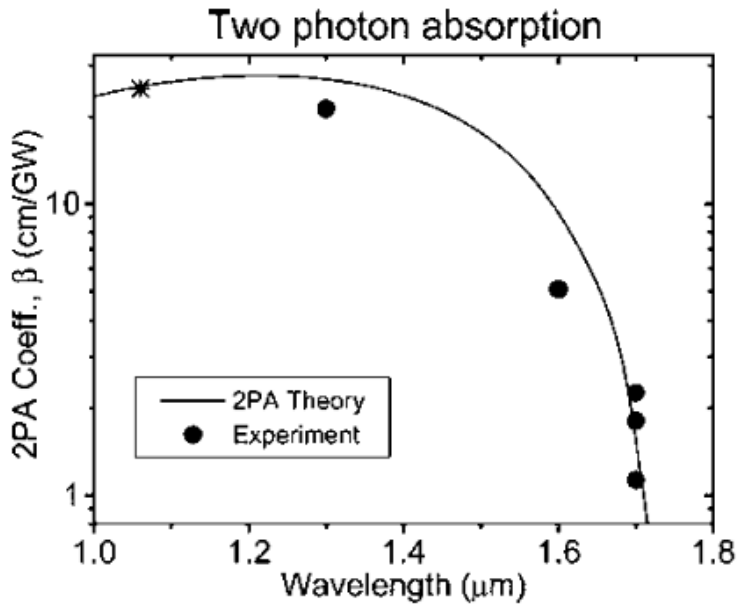

Figure 2: Nonlinear absorption in GaAs. A graph showing the theoretical (line) and experimental (dots) two photon absorption for GaAs from 1000 nm to 1800 nm, with polarization along the [1100] plane of GaAs. The $(*)$ is data from elsewhere in literature [10]. *This figure from [5].*

1.2 Problem Statement

Improving upon current long-range atmospheric sensors and communications requires finding additional coherent light sources in the IR wavebands of $1 - 1.8$ μm, $3 - 5$ μm, and $8 - 12$ μm.

1.3 Research Goal

Characterize the d-coefficients, nonlinear refractive index, and two photon absorption of the $GaAs_xP_{1-x}$ ternary compounds and $Sn_2P_2S_6$, with characterizations of ZnSe and GaAs as a verification step.

1.4 Research Questions

1. Does $GaAs_xP_{1-x}$ allow access to higher d-coefficients similar to GaAs while having a lower β like GaP? If so, what stoichiometry best accomplishes this?

2. Can an effective method for measuring the d-coefficients of $Sn_2P_2S_6$ be developed for the Instensity-scan Method of the Maker Fringe experiment?

1.5 Scope

This research is part of a larger joint effort between the Air Force Institute of Technology and multiple Air Force Research Laboratory (AFRL) directorates: the Materials and Manufacturing Directorate (AFRL/RX), the Sensors Directorate (AFRL/RY), and the Aerospace Systems Directorate (AFRL/RQ). The purpose of this collaboration is to discover new materials with useful NLO and electro-optical (EO) properties. This thesis is focused on the nonlinear characterization of new materials synthesized by AFRL/RX and AFRL/RY. Before characterization, AFRL/RX and AFRL/RY determined if any crystals grown have favorable unit cell structures and can be grown large enough for the characterization techniques. These materials are then characterized using the Maker Fringe and the Z-Scan experiments, and the data analyzed to determine their d-coefficients, nonlinear refractive index, and nonlinear absorption.

The objectives of this thesis are as follows:

1. Set up and calibrate a Maker Fringe experiment at AFRL/RY for this thesis and for future materials characterization under the continuation of this collaboration, with the ability to perform the Intensity-scan Method and the Rotation Method;

2. Characterize the $GaAs_xP_{1-x}$ ternary compounds and $Sn_2P_2S_6$ using the Maker Fringe and the Z-Scan experiments;

3. Document any trends between the stoichiometries of the $GaAs_xP_{1-x}$ ternary compounds and the properties characterized.

1.6 Assumptions

- The composition of each sample is congruent throughout, unless otherwise stated.

- Poynting vector walk-off within the sample between the pump and harmonic waves is not large enough to affect the data because of the small thicknesses of the samples.

1.7 Document Overview

This thesis will discuss the following within their own sections:

1. An overview of relevant topics in nonlinear optics (Section 2.1);

2. A background on how the experimental techniques characterize the nonlinear properties (Section 2.2);

3. Relevant known properties of the materials under study (Section 2.3);

4. The experimental setups (Sections 3.1 and 3.2);

5. The specific test samples used in the experiments (Section 3.3);

6. Experimental results and analysis of those results (Chapter 4); and

7. Conclusions and future work (Chapter 5).

II. Background and Literature Review

This chapter will highlight important material properties necessary for optical parametric generation, why these properties matter, and how these NLO properties are derived. Afterwards, the chapter will explain the theory behind the characterization techniques, explaining how nonlinear properties are measured and calculated. The chapter will end by discussing the known relevant properties of the crystals that were studied in this effort.

2.1 Theoretical Background

2.1.1 Properties of Light and Its Interactions with Materials

The refractive index (n) is the ratio of the speed of light in a vacuum to the speed of light in a given medium, or

$$n = \frac{c}{v}, \tag{1}$$

with c being the speed of light in a vacuum and v the speed of light in a medium [12]. The refractive index also varies based on wavelength, which is a property called dispersion [4]. In between absorption bands, n decreases monotonically for normal-dispersion materials, but near the absorption band edges n behaves differently, as seen in Figure 3 [4]. Dispersion becomes relevant in Section 2.1.2.1. The refractive index of a material, if known, is modelled or approximated by Sellmeier equations [4]. A material's Sellmeier equation(s) captures the change in n with respect to wavelength, temperature, and wave polarization.

The definition of n is given by

$$n = \sqrt{\epsilon_r \mu_r} = \sqrt{\left(\frac{\epsilon}{\epsilon_0}\right)\left(\frac{\mu}{\mu_0}\right)} \tag{2}$$

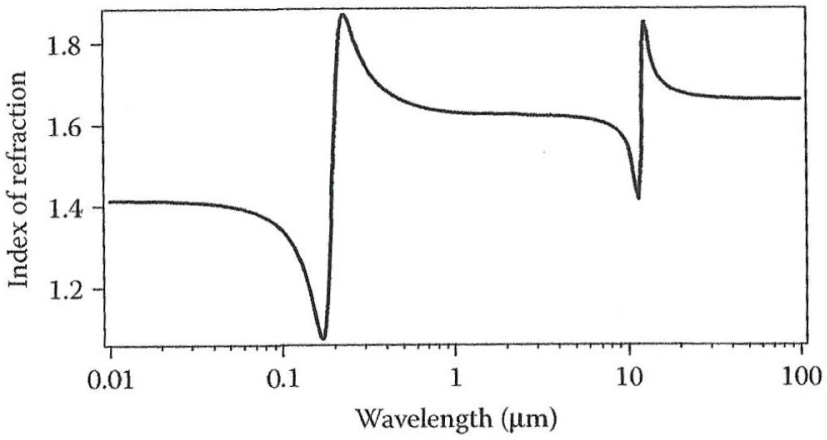

Figure 3: Example of dispersion in materials. The absorption bands of the material are where the index of refraction increases sharply. Away from the absorption bands near 0.2 μm and 10 μm, the refractive index is slightly decreasing with increasing wavelength. Around the absorption bands, n decreases more rapidly until at the absorption bands, where n suddenly increases by a large amount before decreasing again. *This figure is from [4].*

where ϵ_0 is the permittivity of free space, ϵ is the permittivity of the material, μ_0 is the magnetic permeability of free space, μ is the magnetic permeability of the material, and ϵ_r and μ_r are the relative permittivity and magnetic permeability, respectively [4]. For non-magnetic materials including the ones examined in this paper, $\mu = \mu_0$, so $n = \sqrt{\epsilon_r}$.

When a light wave is incident on a material, some of it will be reflected, some will be absorbed into the material, some will be scattered from the surface or within the material, and the rest will be transmitted [13]. The sum of the energies of the reflected, absorbed, scattered, and transmitted waves must equal that of the initial wave. For nonlinear materials, a fraction of what is transmitted can be converted to a different frequency, which can also be reflected, absorbed, or transmitted.

Reflection occurs when light travels from one medium to another with different indices of refraction, as when entering the material and exiting the material (see Figure 4) [12]. The quantity of wave reflection depends on the differences in n for the

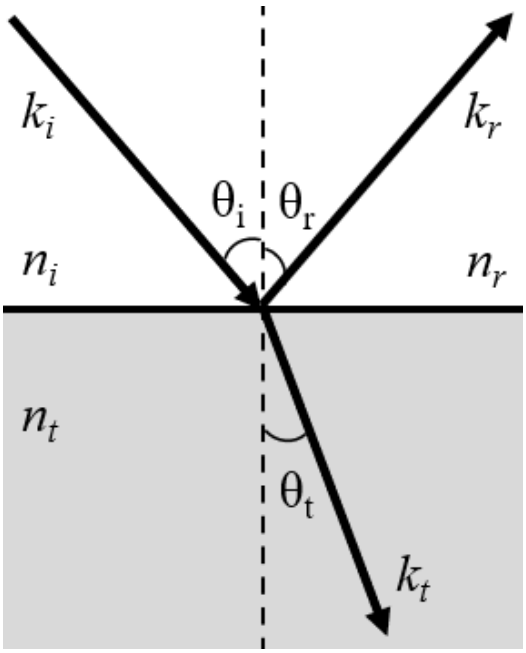

Figure 4: Diagram illustrating Snell's Law. Each k-vector represents the incident (k_i), reflected (k_r), and transmitted (k_t) waves.

incident material (n_i) and the transmitted material (n_t), the angle of incidence (θ_i), and the polarizations of the light [12]. Illustrated in Figure 4, Snell's Law is used to determine the angles of transmission (θ_t) and reflection (θ_r) based on the angle of incidence [12]:

$$n_i \sin\theta_i = n_t \sin\theta_t = n_r \sin\theta_r. \tag{3}$$

When the light is incident on an interface between two materials with different refractive indices, the interface's normal vector and the light wave's k-vector form a plane of incidence (see Figure 5) [12]. The polarization of the light can then be decomposed into perpendicular ($\perp$) and parallel ($||$) waves, where the perpendicular waves have their polarization perpendicular to the plane of incidence and the parallel waves have their polarization within the plane [12]. The $\perp$-waves and $||$-waves are commonly referred to as s-waves and p-waves, respectively, but this naming convention will not be used since s and p are used to represent other terms [14]. The amount of light that

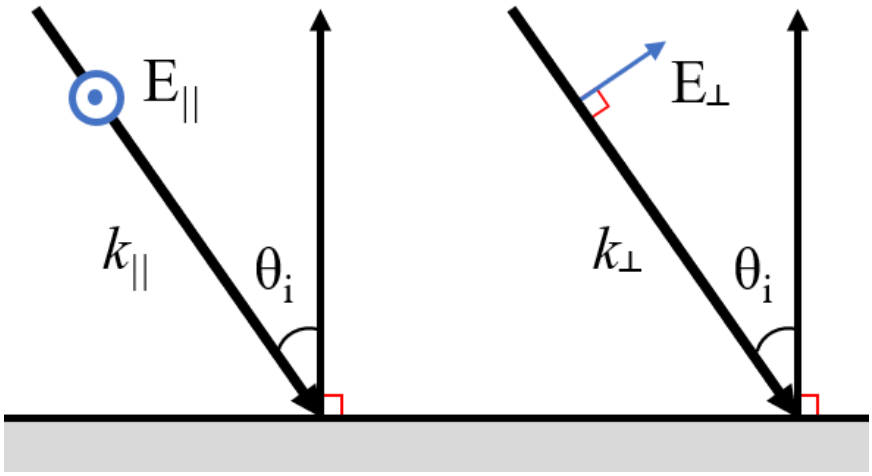

Figure 5: Parallel-polarized and perpendicular-polarized waves incident on a material. This figures illustrates the difference between a parallel-polarized wave (left) and a perpendicular-polarized wave (right), where the polarizations are parallel (left) or perpendicular (right) to the plane of incidence. The waves are represented by their k-vectors, and the surface normal is shown next to each k-vector.

is reflected and transmitted at a surface can be determined by the Fresnel equations:

$$r_\perp = \frac{n_i \cos\theta_i - n_t \cos\theta_t}{n_i \cos\theta_i + n_t \cos\theta_t} \tag{4}$$

$$r_{||} = \frac{n_t \cos\theta_i - n_i \cos\theta_t}{n_t \cos\theta_i + n_i \cos\theta_t} \tag{5}$$

$$t_\perp = \frac{2n_i \cos\theta_i}{n_i \cos\theta_i + n_t \cos\theta_t} \tag{6}$$

$$t_{||} = \frac{2n_i \cos\theta_i}{n_i \cos\theta_t + n_t \cos\theta_i}, \tag{7}$$

where r and t are the amplitude reflection coefficient and the amplitude transmission coefficient, respectively, for either the $\perp$-wave or the $||$-wave [12]. The next two equations are used to determine the amount of the wave reflected or transmitted when θ_i is not zero,

$$R_x = r_x^2 \tag{8}$$

$$T_x = \frac{n_t \cos\theta_t}{n_i \cos\theta_i} t_x^2, \tag{9}$$

where R and T are reflectance and transmittance, respectively, and x is either $\perp$ or $||$ for perpendicular waves or parallel waves, respectively [12]. R_x and T_x are the fractions of the wave reflected and transmitted at the surface, respectively. This means that by the conservation of energy, the intensities of the reflected wave and the transmitted wave together must equal that of the incident wave, assuming no scattering or absorption [12]. For $\theta_i = 0$, Equations 8 and 9 become [12]

$$R = R_\perp = R_{||} = \left(\frac{n_t - n_i}{n_t + n_i}\right)^2 \tag{10}$$

$$T = T_\perp = T_{||} = \frac{4n_t n_i}{(n_t + n_i)^2}. \tag{11}$$

It should be emphasized that this discussion relates only to scenarios involving a single surface.

Absorption occurs when a photon excites an electron to a higher energy state of an atom or a molecule [2, 12]. A photon's frequency is representative of how much energy it contains:

$$E = h\nu \tag{12}$$

where E is energy, h is Planck's constant (6.626×10^{-34} $\mathrm{m^2kg/s}$), and $\nu = 2\pi\omega$ is the frequency of the photon with ω being the angular frequency of the photon [12]. Thus, a higher frequency photon has a higher energy than a lower frequency photon [12]. Elements have different electron energy states from one another and molecules similarly have different vibrational-energy modes from one another. Thus, the photon frequency that an atom or molecule can absorb is dependent on the materials atomic and molecular structure. This is seen in Figure 1, where common molecules like O_2 absorb some frequencies partially or completely. If there is absorption in a material

for a given frequency, it can be determined by

$$I(z) = I_0 e^{-\alpha z}, \tag{13}$$

where α is the absorption coefficient (typically in cm^{-1}), I_0 is the initial intensity of the light wave transmitted into the material, and I is the intensity at z, the distance into the material [12, 13]. The transmittance through a parallel plate material at $\theta_i = 0$ can be determined by,

$$T = \frac{(1-R)^2 e^{-\alpha L}}{1 - R^2 e^{-2\alpha L}} \tag{14}$$

where L is the sample thickness, α is the absorption coefficient, and R is given by Equation 10 [15]. Equation 14 takes into account multiple internal reflections, allowing more light to transmit through than if surfaces were not parallel [15]. Equation 14 is also used when scattering of light is present [15]. The α term represents all losses present in the material, which includes absorption and scattering [15]. For an ideal sample (no absorption or scattering), $\alpha = 0$, and the Equation 14 reduces to [15]

$$T = \frac{1-R}{1+R}. \tag{15}$$

When it comes to the propagation of laser beams, the intensity of the beams should ideally be Gaussian (see Figure 6), where most of the energy is near the center of the beam [12]. These beams allow a high amount of energy over a small cross-sectional area (spot size $w(z)$) and can be designed to have minimal divergence. There are three methods commonly used to measure the spot size of a beam:

1. Full Width Half Max (FWHM), where $w(z)$ is the beam diameter measured at half the maximum intensity;

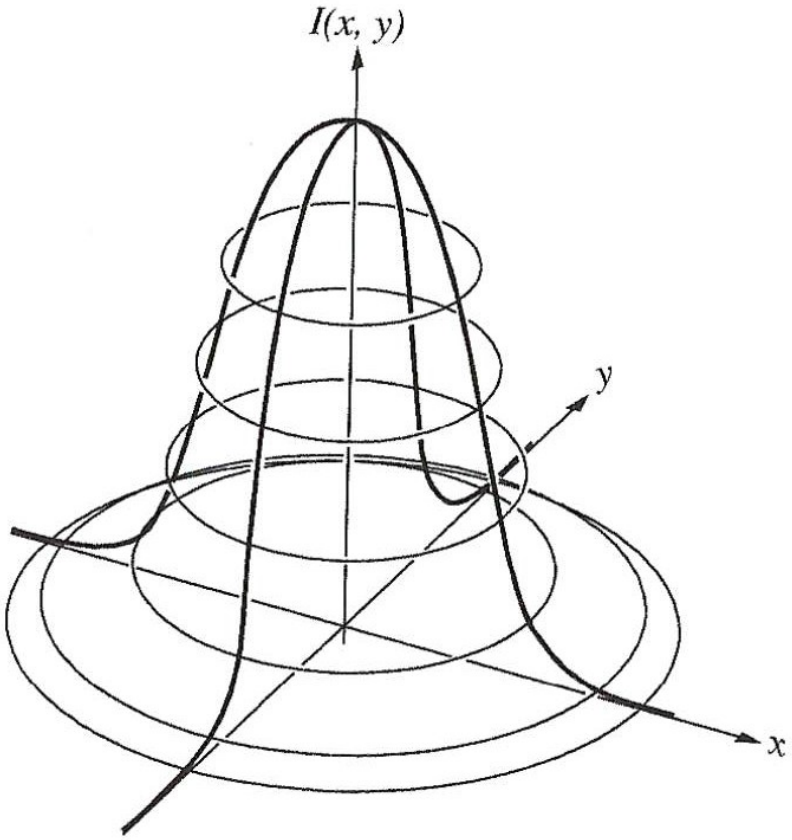

Figure 6: Intensity plot of a Gaussian beam. This figure illustrates the intensity of a Gaussian beam propagating down the z-axis. The three-dimensional Gaussian shape is made by rotating a two-dimensional Gaussian profile about the z-axis. *This figure is taken from [12].*

2. Half Width $1/e$ Max (or $1/e$), where $w(z)$ is the beam radius measured at $1/e$ times the maximum intensity; and

3. Half Width $1/e^2$ Max (or $1/e^2$), where $w(z)$ is the beam radius measured at $1/e^2$ times the maximum intensity;

where e is the Euler's number 2.71828 [4, 12]. It is important to keep track of which method of beam characterization was used, to ensure results can be compared accurately. The default used in this thesis for $w(z)$ is $1/e^2$; it will be noted when the default is not used. The beam can be focused to a minimal spot size with a radius

called the beam waist (w_0). On both sides of w_0 is a range called the Rayleigh Range (z_R) where the radius changes by no more than $\sqrt{2}$ (see Figure 7), where [4, 12]

$$z_R = \frac{\pi w_0^2}{\lambda}. \tag{16}$$

Within this $2z_R$ range, the intensity of the beam is often treated to be the same within the range.

To this point, the type of material has not been considered as the discussion applies to any material. Materials can be classified as birefringent or nonbirefringent. Nonbirefrigent (or isotropic) materials, like GaAs, are those that have the same refractive index regardless of the light's polarization. However, birefringent materials, like $Sn_2P_2S_6$, have different indices of refraction for each polarization [4]. A three-axis orthogonal coordinate system (xyz) is used to track the changes in n with respect to the polarization of the light traveling through the birefringent material. This xyz-coordinate system depends on whether the material is "biaxial" (where each axis has a different n) or "uniaxial" (where the z-axis has a different n than the x-y plane) [4]. Due to the complexity of biaxial crystals, this discussion will be limited to uniaxial

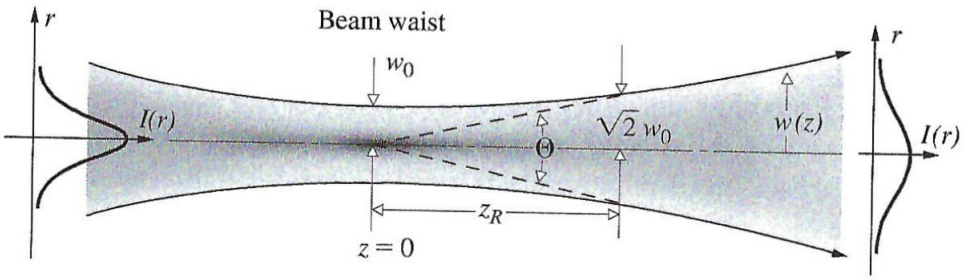

Figure 7: Rayleigh Range of a focused Gaussian beam. The Rayeigh Range z_R is the distance from the focus (z=0) to where the radius of the beam is $\sqrt{2}$ times the beam waist w_0. $w(z)$ is the radius of the beam at position z, and Θ is the divergence angle. The plots on either side show the cross-sectional intensity of the beam with respect to the radius. *This figure is from [12].*

materials; biaxial crystals can be analyzed as a uniaxial crystal when only taking into account two of the three axes [4]. For uniaxial materials, the z-axis is what is called the optic axis [4]. Relating this coordinate system to the light's polarization, any light wave can be broken into two waves with orthogonal polarizations: ordinary waves (o-waves) which have their polarization within the x-y plane, and extraordinary waves (e-waves) which have their polarizations orthogonal to the o-waves' polarization and their k-vectors [4]. Since the o-wave's polarization is always within the x-y plane, o-waves will always experience the same refractive index due to the x-y plane having the same refractive index n_o. As for e-waves, they will only have the same refractive as o-waves when propagating along the optic axis, since their polarization is within the x-y plane. When propagating within the x-y plane, the refractive index experienced by the e-waves is the refractive index for the optic axis n_z. When propagating elsewhere in the crystal, the e-waves' refractive index n_e will vary based on the angle θ between the optic axis and the k-vector [4]:

$$\frac{1}{n_e^2(\theta)} = \frac{\cos^2(\theta)}{n_o^2} + \frac{\sin^2(\theta)}{n_z^2}. \tag{17}$$

The differences in n for e-waves and o-waves is illustrated in Figure 8 for positive uniaxial crystals ($n_z > n_o$) and for negative uniaxial crystals ($n_z < n_o$) [4]. Due to the difference in n within the x-y plane and along the optic axis, there are at least two Sellmeier equations, one for the x-y plane (n_o) and one for the optic axis (n_z). O-waves will always use the equation for n_o, and e-waves will use both Sellmeier equations in Equation 17 to determine n_e [4].

A phenomenon occurs when both e- and o-waves are incident on a birefringent material propagating the same direction (excluding the optic axis): the e-wave will "walk-off" from the o-wave based on its Poynting vector, denoted $\overrightarrow{S}$ (see Figure 9) [4]. This means that while the e-wave's k-vector remains unchanged, the energy of

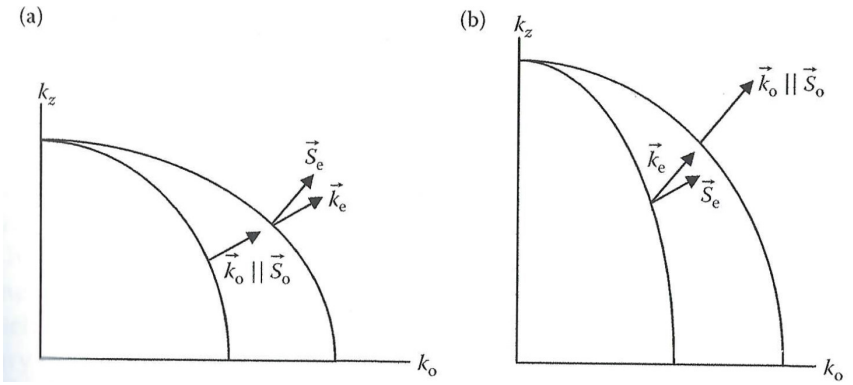

Figure 8: Refractive index differences based on polarization in uniaxial crystals. These figures show the refractive indices for positive uniaxial (a) and negative uniaxial (b) crystals. The axes shown are the ordinary axis (k_o) which is within the x-y plane and the optic axis (k_z). The vectors shown are the propagation vectors ($\overrightarrow{k}$) and the Poynting vectors ($\overrightarrow{S}$) for the ordinary waves (o-waves, subscript o) and the extraordinary waves (e-waves, subscript e). For the e-waves, n either increases (a) or decreases (b) as $\overrightarrow{k_e}$ points away from k_z towards k_o. *This figure is taken from [4].*

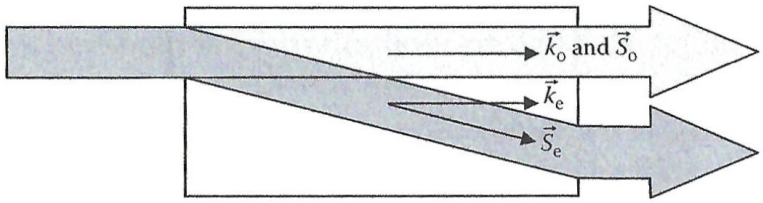

Figure 9: Poynting vector walkoff. A light wave composed of an e-wave and an o-wave travels through a birefringent material. *This figure is from [4].*

the e-wave travels in the direction of the S-vector [4]. The direction of the S-vector is always perpendicular to the refractive index experienced by either wave, as seen in Figure 8 [4]. Thus, for o-waves, $\overrightarrow{S_o}$ is always parallel to $\overrightarrow{k_o}$, but for e-waves, $\overrightarrow{S_e}$ is only parallel to $\overrightarrow{k_e}$ on the optic axis (see Figure 10) [4]. The angle between $\overrightarrow{S_e}$ and $\overrightarrow{k_e}$ is the Poynting vector walkoff angle ρ, which is the same angle between $\overrightarrow{E}$ (electric field) and $\overrightarrow{D}$ (electric displacement) [4]. As such, the electric field is always perpendicular to the Poynting vector, not the k-vector. This phenomenon only occurs inside the birefringent material; when the wave exits the material, the e-wave's energy once

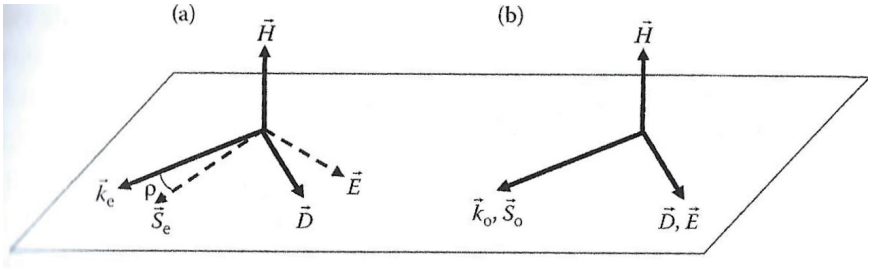

Figure 10: Directions of components of an electro-magnetic wave in a birefringent material. The differences in directions of the wave's components between e-waves (a) and o-waves (b) are illustrated. The direction of the magnetic field vector $\overrightarrow{H}$ remains unchanged and perpendicular to the other components. *This figure is from [4].*

again travels with its k-vector [4]. However, the birefringent materials examined in this paper are too thin for this Poynting vector walk-off to affect any results, so this will be ignored.

2.1.2 $\chi^{(2)}$ Nonlinearity

The polarization ($\overrightarrow{P}$) of a material by the electric field ($\overrightarrow{E}$) of an incident light wave is expressed as

$$\overrightarrow{P}(t) = \epsilon_0 \chi \overrightarrow{E}(t) \tag{18}$$

where $\overrightarrow{P}$ is the polarization at time t, ϵ_0 is the permittivity of free space, $\overrightarrow{E}$ is the complex amplitude of the electric field at time t, and χ is the susceptibility of the material [4]. χ is related to n by

$$n = \sqrt{(1+\chi)}, \tag{19}$$

thus from Equation (2), $\epsilon_r = 1 + \chi$ when $\mu_r = 1$ [4]. This relationship means that a change in refractive index results in a change in χ [4]. As such, a change in wavelength will result in a change in χ. This also means that there are multiple values for χ for birefringent materials due to the refractive index not being the same for all

polarizations.

A Taylor Series expansion can be performed on χ in Equation 18 to obtain

$$\overrightarrow{P}(t) = \epsilon_0 \left(\chi^{(1)} E(t) + \chi^{(2)} E^2(t) + \chi^{(3)} E^3(t) + ...\right) \tag{20}$$

where $\chi^{(1)}$ is the linear susceptibility, $\chi^{(2)}$ is the first order of nonlinear susceptibility, and so on [4]. Individual orders of polarizations can be examined separately from the other orders:

$$\overrightarrow{P}^{(1)}(t) = \epsilon_0 \chi^{(1)} \overrightarrow{E}(t); \tag{21}$$

$$\overrightarrow{P}^{(2)}(t) = \epsilon_0 \chi^{(2)} \overrightarrow{E}^2(t); \tag{22}$$

and so on [4]. The relative strengths of increasing orders of nonlinearity are shown below [4]:

$$|\chi^{(1)}| >> |\chi^{(2)} E(t)| >> |\chi^{(3)} E^2(t)| >> ... \tag{23}$$

In general, susceptibility is a tensor oroperty that increases in rank with the higher orders of nonlinearity. $\chi^{(2)}$ is a rank 3 tensor, so all $\chi^{(2)}$ nonlinear processes involve three light waves. Since these processes involve frequency conversion without the addition of outside energy, they must obey the law of conservation of energy, thus $\omega_1 = \omega_2 + \omega_3$, and by convention $\omega_1 > \omega_2 \geq \omega_3$. These three waves each have polarizations and propagate through a nonlinear material. The polarizations of the three waves can interact in one of 27 ways within the material. As such, each of these 27 susceptibilities are recorded as χ_{ijk}. The indices i, j, k each represent the polarization of each of the three waves, respectively: x-, y-, or z-axis polarization, written as x, y, z or as 1, 2, or 3 respectively. For these equations, i refers to the polarization of the wave of interest, while j and k refer to the other two waves'

polarizations in decreasing frequency. Thus, Equation 22 can be rewritten as

$$\overrightarrow{P}_i^{(2)}(t) = \epsilon_0 \chi_{ijk}^{(2)} \overrightarrow{E}_j(t) \overrightarrow{E}_k(t) \tag{24}$$

where $\chi_{ijk}^{(2)}$ is the $\chi^{(2)}$ response of the material to the specific polarizations of the three waves [4].

2.1.2.1 *d*-coefficients

A common way to encapsulate the material's nonlinear susceptibilities is with a matrix of d_{ijk} elements instead of χ_{ijk}, where $\chi_{ijk} = 2d_{ijk}$. The d-tensor originates from the early work in NLO and has remained the standard convention for describing $\chi^{(2)}$ nonlinearity [4]. This results in Equation 24 becoming

$$\overrightarrow{P}_i^{(2)}(t) = 2\epsilon_0 d_{ijk} \overrightarrow{E}_j(t) \overrightarrow{E}_k(t) \tag{25}$$

with $d_{ijk} = \frac{1}{2}\chi_{ijk}^{(2)}$ in units of pm/V [4]. This leads to a $3 \times 3 \times 3$ array containing the 27 different susceptibilities, or d-coefficients:

$$\begin{pmatrix} d_{111} & d_{112} & d_{113} \\ d_{121} & d_{122} & d_{123} \\ d_{131} & d_{132} & d_{133} \end{pmatrix}, \begin{pmatrix} d_{211} & d_{212} & d_{213} \\ d_{221} & d_{222} & d_{223} \\ d_{231} & d_{232} & d_{233} \end{pmatrix}, \begin{pmatrix} d_{311} & d_{312} & d_{313} \\ d_{321} & d_{322} & d_{323} \\ d_{331} & d_{332} & d_{333} \end{pmatrix}. \tag{26}$$

This is a cumbersome way to track all the susceptibilities. A simplification is frequently used to reduce the array to a 3×6 matrix. When determining the polarization of the wave of interest, it does not matter how the polarizations of the other two waves are oriented in relation to each other, only that they are either parallel or perpendicular to each other. This leads to a simplification of indices, as shown in Table 1 [4]. As an example, d_{xzy} is written as d_{132}, but can then be condensed to

Table 1: Contracted Index for d-coefficients

j,k	new index
xx	1
yy	2
zz	3
yz,zy	4
xz,zx	5
yx,xy	6

d_{14}. Additionally, d_{xyz} is d_{123}, but is also condensed to d_{14}. This simplification reduces the number of d-coefficients to 18. Applying this simplification to the d-tensor, Equation 26 becomes:

$$\overleftrightarrow{d} = \begin{pmatrix} d_{11} & d_{12} & d_{13} & d_{14} & d_{15} & d_{16} \\ d_{21} & d_{22} & d_{23} & d_{24} & d_{25} & d_{26} \\ d_{31} & d_{32} & d_{33} & d_{34} & d_{35} & d_{36} \end{pmatrix}. \tag{27}$$

At this point, the d-matrix can be simplified even more using Kleinman's symmetry [16]. Kleinman's symmetry is a permutation symmetry that allows the permutation of any of the three susceptibilities without permuting the frequencies; for example, d_{123} is the same as d_{312}, or $d_{14} = d_{36}$ [4, 16]. This applies when all three frequencies are outside the absorption bands of the material, resulting in the dispersion of $\chi^{(2)}$ being negligible [4, 16]. This simplifies the d-matrix to

$$\overleftrightarrow{d} = \begin{pmatrix} d_{11} & d_{12} & d_{13} & d_{14} & d_{15} & d_{16} \\ d_{16} & d_{22} & d_{23} & d_{24} & d_{14} & d_{12} \\ d_{15} & d_{24} & d_{33} & d_{23} & d_{13} & d_{14} \end{pmatrix}. \tag{28}$$

This matrix can be further simplified depending on the structure of the material's unit cell. The unit cell is the fundamental geometric arrangement of atoms in a crystal that, when repeated, forms the crystal (an example is shown in Figure 11) [13].

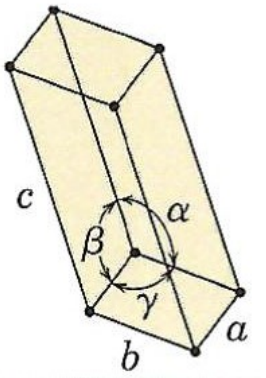

Figure 11: Unit cell structure of triclinic crystal. For triclinic crystals, the side lengths a, b, and c do not equal each other, while the internal angles α, β, and γ also do not equal each other. Other unit cells have some or all sides/angles being the same. *This figure is from [13].*

Unit cells with similar structures are grouped together in groups called point groups, or even smaller groups called space groups [17, 18]. As mentioned above, $\chi^{(2)}$ is a Rank 3 tensor, and as such, it is self-similar under some specific coordinate transformations of rotation, reflection, and inversion (coordinate transformations that do not stretch, skew, alter the coordinate axes) [4, 17, 19]. Unit cells within the same point group will have the same transformations, and thus will have the same simplified d-matrix [4, 17, 18]. These transformations are encapsulated in a 3×3 "R-matrix". For example, a rotation $+90°$ about the z-axis would have a corresponding R-matrix of

$$\begin{pmatrix} \cos\frac{\pi}{2} & \sin\frac{\pi}{2} & 0 \\ -\sin\frac{\pi}{2} & \cos\frac{\pi}{2} & 0 \\ 0 & 0 & -1 \end{pmatrix}. \tag{29}$$

To determine the new d-coefficient in a transformed coordinate system, the following equation is used

$$d'_{ijk} = \sum_{\alpha=1}^{3}\sum_{\beta=1}^{3}\sum_{\gamma=1}^{3} R_{i\alpha}R_{j\beta}R_{k\gamma}d_{\alpha\beta\gamma}, \tag{30}$$

where d'_{ijk} is the new d-coefficient and each R_{ab} is an entry in the corresponding

R-matrix [4, 19]. For an inversion transformation, the R-matrix is

$$\begin{pmatrix} -1 & 0 & 0 \\ 0 & -1 & 0 \\ 0 & 0 & -1 \end{pmatrix}. \tag{31}$$

If this inversion transformation applies to a specific d-coefficient, we have

$$\begin{aligned} d'_{ijk} &= \sum_{\alpha=1}^{3}\sum_{\beta=1}^{3}\sum_{\gamma=1}^{3} R_{i\alpha}R_{j\beta}R_{k\gamma}d_{\alpha\beta\gamma} \\ &= R_{11}R_{22}R_{33}d_{ijk}(-1)(-1)(-1)d_{ijk} = -d_{ijk}. \end{aligned} \tag{32}$$

Since $d'_{ijk} = -d_{ijk}$, d_{ijk} must equal 0 as a result of this transformation. Thus, any d-coefficient that has an inversion transformation will be reduced to 0. For centrosymmetric crystal structures, there is an inversion transformation that applies to every d-coefficient, thus reducing the d-matrix to a 3×6 matrix of zeros. Thus, centrosymmetric materials have no $\chi^{(2)}$ nonlinearity.

The d-coefficients for a particular crystal can be found using Equation 25 [4]. The polarization of the wave of interest is on the left side, and the right side is expanded to account for every possible d-coefficient and electric field combination of the other two waves. In this case, the polarization of ω_3 is being examined in relationship to

ω_1 and ω_2:

$$\overrightarrow{P}(\omega_3) = 2\epsilon_0 \begin{pmatrix} d_{11} & d_{12} & d_{13} & d_{14} & d_{15} & d_{16} \\ d_{16} & d_{22} & d_{23} & d_{24} & d_{14} & d_{12} \\ d_{15} & d_{24} & d_{33} & d_{23} & d_{13} & d_{14} \end{pmatrix} \begin{pmatrix} E_x(\omega_1)E_x^*(\omega_2) \\ E_y(\omega_1)E_y^*(\omega_2) \\ E_z(\omega_1)E_z^*(\omega_2) \\ E_z(\omega_1)E_y^*(\omega_2) + E_y(\omega_1)E_z^*(\omega_2) \\ E_z(\omega_1)E_x^*(\omega_2) + E_x(\omega_1)E_z^*(\omega_2) \\ E_y(\omega_1)E_x^*(\omega_2) + E_x(\omega_1)E_y^*(\omega_2) \end{pmatrix} \tag{33}$$

As mentioned before, coefficients in the d-matrix may equal zero due to crystal symmetries. Terms in the other matrix my be reduced to zero due to the propagation directions of the other two waves; for example, if ω_1 propagates only on the x-axis, then the $E_y(\omega_1)$ and $E_z(\omega_1)$ terms are zero. After multiplying the matrices, the equation will take the form similar to Equation 25:

$$\overrightarrow{P}(\omega_3) = 2\epsilon_0 d_{eff} E_1 E_2^*, \tag{34}$$

where d_{eff} is the effective d-coefficient based on the propagations and polarizations of waves 1 and 2 [4]. The matrix multiplication results in $d_{eff}E_1E_2^*$ being a 3×1 vector, where each row represents P_x, P_y, and P_z in order. As mentioned above, d_{eff} may contain multiple weighted d-coefficients, depending on crystal structure and propagations of the other two waves.

Since n and χ are related to each other (Equation 19), the d-coefficients are also affected by dispersion. This results in the same d-coefficient having different values at different wavelengths. To avoid measuring the coefficients at numerous different wavelengths, Miller's Rule can be used to approximate a d-coefficient at another set

of wavelengths [9, 20]. Miller's Rule involves calculating Miller's Δ at one set of wavelengths and using the calculated Δ for another set of wavelengths, both for the same d-coefficient [9, 20]. To calculate Miller's Δ, the following equation is used:

$$d_{ijk} = \chi_{ii}^{(2)}\chi_{jj}^{(2)}\chi_{kk}^{(2)}\Delta_{ijk} = (n_1^2 - 1)(n_2^2 - 1)(n_3^2 - 1)\Delta_{ijk}, \tag{35}$$

where $\chi = n^2 - 1$ [4, 20]. Equation 35 is first used with a known d_{ijk} and its corresponding χ or n values to calculate Δ_{ijk}. Using this calculated Δ_{ijk}, Equation 35 is then used to calculate the value for the same d-coefficient using the χ or n values corresponding to the new wavelengths:

$$d'_{ijk} = (n_4^2 - 1)(n_5^2 - 1)(n_6^2 - 1)\Delta_{ijk}, \tag{36}$$

where waves 4, 5, and 6 have the same polarizations as 1, 2, and 3 such that d_{ijk} and d'_{ijk} have the same subscripts. d-coefficients are commonly presented in literature as being calculated via second harmonic generation, with the pump wavelength being the wavelength associated with the d-coefficient. This convention will be used when using Miller's Rule in this thesis.

A limitation with Miller's rule is the accuracy the calculated d_{ijk} value is to the actual d value. This accuracy varies with samples and with wavelengths, which can produce errors upwards of 35% in certain scenarios [8]. However, using Miller's Rule may be the only option to estimate d at a given wavelength if unable to directly calculate the d-coefficient.

2.1.2.2 Phase Matching and Quasi-Phase Matching

To achieve the most efficient frequency conversion for $\chi^{(2)}$ materials, the three interacting waves need to be phase matched. The three waves are considered phase

matched when the propagation vectors, or k-vectors, of waves 2 and 3 add up to that of wave 1 (see Figure 12) [4]. Figure 12 shows both noncollinear (k-vectors are not propagating in the same direction) and collinear (all propagate in the same direction) phase matching. This discussion will focus only on collinear phase matching, as this will be the method used in the Maker Fringe experiment.

For the collinear case, the vector notation will be dropped since all three waves travel the same direction. The k-vector can be written in terms of frequency and refractive index: $k = n\omega/c$ [4]. Thus, the phase matching equation is

$$0 = k_1 - k_2 - k_3 = \frac{n_1\omega_1}{c} - \frac{n_2\omega_2}{c} - \frac{n_3\omega_3}{c} \tag{37}$$

or

$$\Delta k = n_1\omega_1 - n_2\omega_2 - n_3\omega_3 \tag{38}$$

where $\Delta k = k_1 - k_2 - k_3$ and $\Delta k = 0$ is phase matched [4]. Recall the convention $\omega_1 > \omega_2 \geq \omega_3$, and recall from Section 2.1.1 that dispersion dictates that $n_1 > n_2 \geq n_3$ if all three waves are not separated by absorption bands. Because of dispersion, phase matching cannot occur under this scenario if all three waves have the same polarization since Δk will never equal zero. Thus, those corresponding d-coefficients are unobtainable with this method of phase matching. For example, congruent lithium niobate ($LiNbO_3$) has a d_{33} of -27.2 pm/V, but since accessing this component re-

Figure 12: Phase matched k-Vectors. The left figure is an example of noncollinear phase matching. The right figure is an example of collinear phase matching. Each vector k_a corresponds to the ath wave.

quires all three waves to be z-polarized, the largest accessible d-coefficient in terms of magnitude is d_{31} at -4.35 pm/V [21].

When phase matching does not occur ($\Delta k \neq 0$), frequency conversion can still happen but only for a specific distance within the material, called the coherence length (L_c) [4]. This limitation arises from a phase mismatch between the pump and the converted waves ($\Delta\phi = \Delta k L$, where $\phi = 2\pi n/\lambda$), as seen in Figure 13 [4]. Energy transfers from the pump wave to the converted waves until the the phase mismatch reaches π radians, after which the converted waves "back-convert" to the pump wave until the phase mismatch reaches 2π, or zero [4]. This forward and back conversion follows a sinusoidal pattern, where the peaks happen at every odd integer multiple of L_c, and the valleys at every even integer multiple (see Figure 14) [4]. This non-phase matched frequency conversion can happen regardless of wave polarization. For SHG processes where all three k-vectors propagate in the same direction, L_c can be

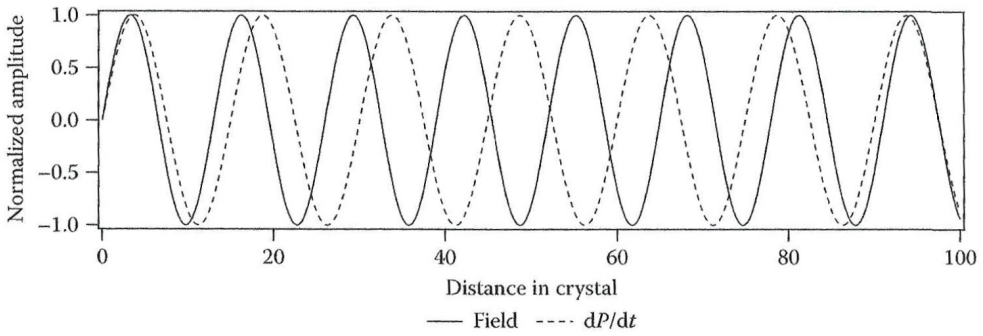

Figure 13: Phase misalignment between fundamental and generated waves when not phasematched. The solid line shows the phase of the fundamental wave, and the dotted line shows the phase of the generated wave. The distance in the crystal is in arbitrary units (a.u.), with 50 a.u. being one L_c. *This figure is from [4].*

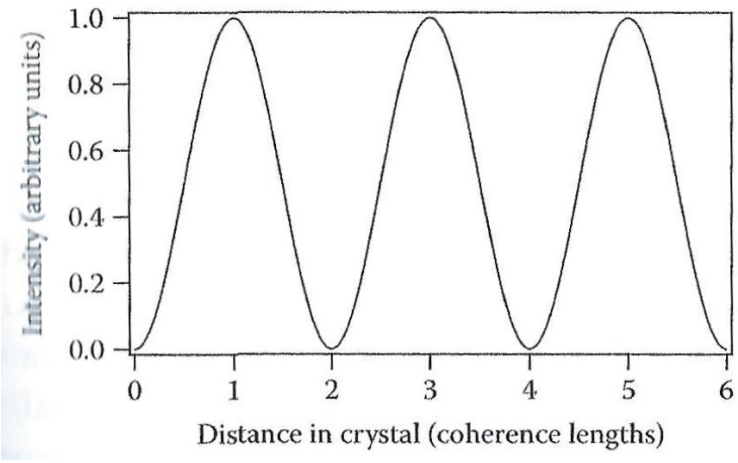

Figure 14: Intensity of a frequency converted wave when not phase matched. *This figure is from [4].*

determined:

$$\pi = (k_s - k_p - k_p)\, L_c = (k_s - 2k_p)\, L_c \tag{39}$$

$$\pi = L_c\, (n_s\omega_s - 2n_p\omega_p) \tag{40}$$

$$\pi = L_c \left(\frac{2\pi n_s}{\lambda_s} - \frac{4\pi n_p}{\lambda_p} \right) \tag{41}$$

$$\pi = 2\pi L_c \left(\frac{n_s}{\lambda_p/2} - \frac{2n_p}{\lambda_p} \right) \tag{42}$$

$$\pi = \frac{4\pi L_c}{\lambda_p}(n_s - n_p) \tag{43}$$

$$\therefore L_c = \frac{\lambda_p}{4\,(n_s - n_p)}, \tag{44}$$

where $k = n\omega$, $\omega = 2\pi/\lambda$, and the subscripts s and p refer to the SHG wave and the pump wave, respectively [4, 22]. When the k-vectors are not all propagating in the same direction, the angle between the pump and harmonic k-vectors should be accounted for as that will affect L_c. However, this effect will be ignored since the birefringent samples examined in this thesis are considered too thin for this to become an issue.

Back conversion is resolved by inverting the crystal structure every coherence length. Doing so allows the forward frequency conversion process to happen when it would otherwise back convert, leading to the scenario in Figure 15. This method is called quasi-phase matching (QPM), which allows access to the "unobtainable" birefringent d-coefficients mentioned above and allows non-birefringent materials to effectively frequency convert over lengths much longer than L_c [12]. QPM alters the phase matching equation (Equation 38) to

$$\begin{aligned} \Delta k'_m &= \Delta k - k_m = \Delta k - \frac{2\pi}{\Lambda} m \\ &= n_1\omega_1 - n_2\omega_2 - n_3\omega_3 - \frac{2\pi}{\Lambda} m \end{aligned} \tag{45}$$

where Λ is typically two coherence lengths and m is the mth-order of QPM (usually $m = 1$, as that is the most efficient for frequency conversion) [4]. Even though the first-order QPM has a $2/\pi$ scaling factor on the d_{eff} when compared to the

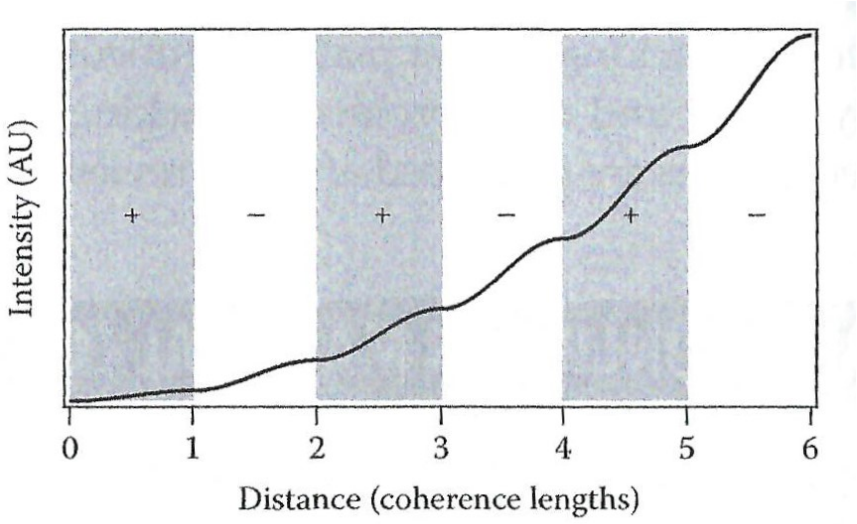

Figure 15: Frequency conversion in a quasi-phasematched material. Light is frequency converted during the first coherence length (L_c). At one L_c through the crystal, the crystal orientation is inverted, causing the light to continue to frequency convert instead of back converting. This process is repeated every L_c for more frequency conversion. Note that the intensity is in arbitrary units (AU). *This image is from [4].*

birefringent phase matching, sometimes QPM is preferred as it can access much higher d-coefficients as is the case with $LiNbO_3$'s d_{33}, mentioned earlier [4].

2.1.3 $\chi^{(3)}$ Nonlinearity

$\chi^{(3)}$ is a Rank 4 tensor, meaning that it involves the interactions between four waves instead of three, with its susceptibility coefficients taking the form $\chi^{(3)}_{ijkl}$ [4]. Due to $\chi^{(3)}$ being a Rank 4 tensor, its R-matrix will be 4×4, meaning that any inversion symmetries within a material will not result in its coefficients being equal to zero, there being four R coefficients instead of three as shown in Equation 32 [4]. As such, all materials (including centrosymmetric ones) can exhibit $\chi^{(3)}$ nonlinearity. As the order of nonlinearities increases, so does the number of possible interactions between the material and the waves. The interaction of interest in this thesis involve all four waves with the same frequency (or the same wave acting as both inputs and both outputs). The material's properties that are affected in this interaction are nonlinear refractive index (n_2) and nonlinear absorption (β) [4]. These properties should be well understood to avoid deleterious effects.

2.1.3.1 Nonlinear Refractive Index

In terms of $\chi^{(3)}$, the nonlinear refractive index n_2 is

$$n_2 = \frac{3}{4\epsilon_0 n_0^2 c}\chi^{(3)}_{iiii} \tag{46}$$

where $\chi^{(3)}_{iiii}$ is real, and the subscript $iiii$ means that all four waves have the same polarization [4]. Relating n_2 to the refractive index n,

$$n = n_0 + n_2 I, \tag{47}$$

where n is the material's total refractive index, n_0 is the linear refractive index as discussed in Section 2.1.2, and n_2 is in units of m^2/W (or cm^2/GW) [4]. Another common way of relating n_2 to n is

$$n = n_0 + \frac{n_2}{2} |E|^2 , \tag{48}$$

where n_2 is in units of esu, with the conversion between esu and m^2/W being [esu]= $cn_0/40\pi[m^2/W]$ [23]. The convention used in this thesis is Equation 47 with n_2 in units of cm^2/GW. So, a change in n_2 will change the material's overall refractive index, thus altering the phase matching conditions which can decrease or change the output of the frequency conversion process. When irradiated by a Gaussian beam, n_2 causes the material to act as a lens, focusing for positive n_2 and defocusing for negative n_2, a feature utilized in the Z-Scan experiment [4, 24].

2.1.3.2 Nonlinear Absorption

The nonlinear absorption (β) corresponding to $\chi^{(3)}$ nonlinearity is two photon absorption (2PA), where as the name suggests, two photons are absorbed simultaneously instead of one. If β is large enough for a set of wavelengths, the material can become unusable for NLO devices due to the losses to 2PA. Therefore, materials with low values of β are desired as frequency converting materials. In terms of the $\chi^{(3)}$ coefficient, β is

$$\beta = \frac{3\omega}{2\epsilon_0 n^2 c^2} \chi^{(3)}_{Im} \tag{49}$$

where n is the total refractive index (Equation 47), ω is the frequency of the wave, and $\chi^{(3)}_{Im}$ is the imaginary part of $\chi^{(3)}_{iiii}$ [4]. When both linear absorption α and β are present, the total absorption caused α and β is related to intensity I by the following

equation [4]:

$$\frac{dI}{dz} = -\alpha I - \beta I^2. \tag{50}$$

2.2 Nonlinear Optical Characterization Techniques

There are two characterization techniques used to determine the three nonlinear properties used in this research. The first is the Maker Fringe technique, which is used to determine the d-coefficients. The second is the Z-Scan technique, which is used to calculate both the nonlinear absorption β and the nonlinear refractive index n_2.

2.2.1 Maker Fringe

In 1962, Maker *et al.* documented an interesting phenomenon involving a piece of quartz [25]. With the pump laser propagation normal to the front and back faces, the quartz was rotated about the propagation direction, and varying amounts of second harmonic light was gathered (see Figure 16) [25]. The initial theory behind this was described by Bloembergen and Pershan in 1962; however, it would not be until 1970 that this interference pattern, or fringes, would be called "Maker Fringes" [26, 27]. Later in 1970, the initial theory behind the phenomenon was developed, which provided the origin of these fringes: bound harmonic waves and free harmonic waves (see Figure 17) [26]. The bound harmonic waves are generated from the standard $\chi^{(2)}$ SHG process, meaning that the bound waves travel with the fundamental waves [26]. The free waves are generated at the input surface from the inter-atomic and dipole forces, and they travel through the material seeing the harmonic refractive index instead of the fundamental's refractive index [26, 27]. Since the bound and the free waves experience different refractive indices, the two sets of waves travel at different speeds and are thus periodically in-phase and out-of-phase with each other. When they exit

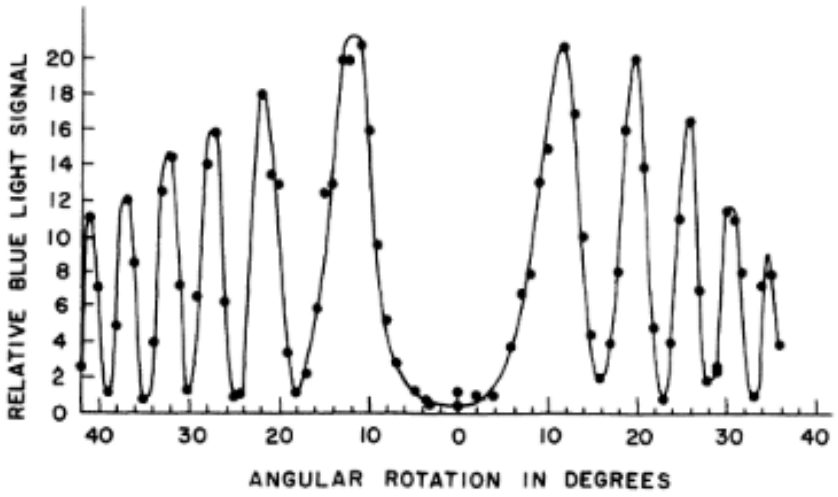

Figure 16: Second harmonic signal from rotating quartz. Relative second harmonic signal is plotted against angular rotation for a slab of quartz, with the line being a fit to the data. The incident wave was normal to the input surface and parallel to the optic axis [25]. Note the rapid change between peaks and valleys; this pattern would later be called "Maker Fringes" [27]. *This figure is modified from [25].*

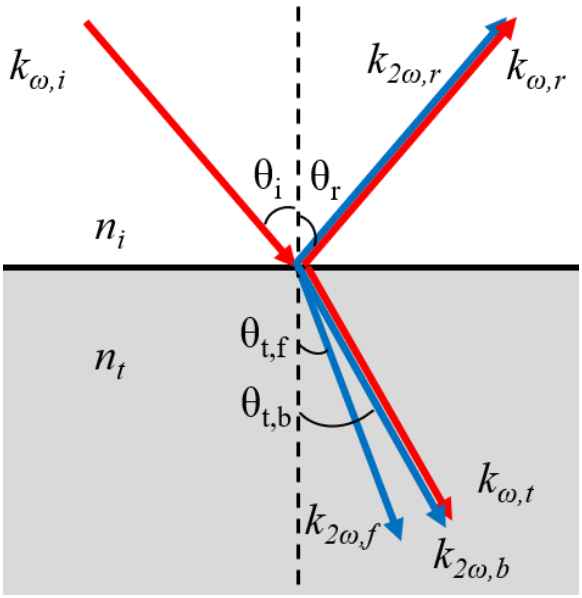

Figure 17: Propagation of harmonic waves at the input surface. The pump wave obeys Snell's law, represented by the incident ($k_{\omega,i}$), reflected ($k_{\omega,r}$), and transmitted ($k_{\omega,t}$) waves. The bound harmonic wave ($k_{2\omega,b}$) travels with $k_{\omega,t}$ according to the transmitted angle from Snell's Law ($\theta_{t,b}$), but the free harmonic wave ($k_{2\omega,f}$) travels separately according to its own internal angle ($\theta_{t,f}$). A harmonic wave ($k_{2\omega,r}$) is generated at the surface and travels with $k_{\omega,r}$.

the material, they travel at the same speed again, so whatever phase offset they have as they exit will be their offset as they propagate outwards. Looking at Figure 16, the peaks and valleys of the "blue light" signal correspond to the bound and free waves being in-phase and out-of-phase, respectively [26, 27]. Since the article by Jerphagnon *et al.* in 1970, improvements were made to the theory to account for different classes of crystals, birefringence, more reflections within the crystal, and absorption at one or both wavelengths [27, 28, 29, 30]. The relevant improvement for this thesis is the "19-Beam Theory" by Murray *et al.*, which is an extension of the "13-Beam Theory" by Pavlides and Pugh [28, 30].

One of the improvements Pavlides and Pugh made was an expansion into crystals with any symmetry, as opposed to the simple symmetries that arise from unit cells like simple cubic that the earlier theories are restricted to [27, 28]. Another improvement they made is the tracking of thirteen different beams from both sides of the irradiated material, as shown in Figure 18 [28]. By tracking both the ordinary and extraordinary components of the incident wave inside the crystal, the bound and free

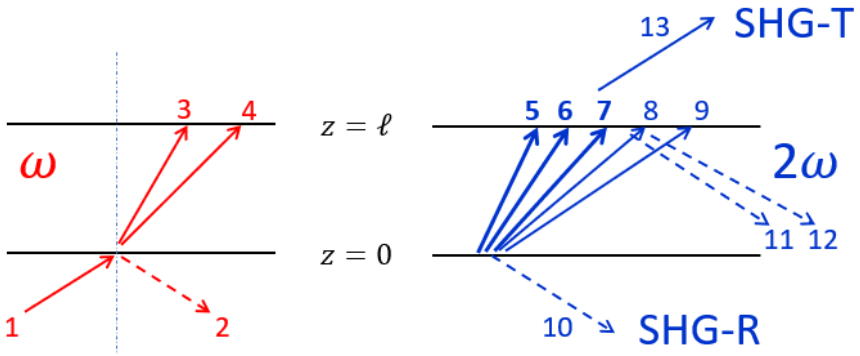

Figure 18: Maker Fringe 13-Beam Theory. The red beams on the left have frequency of ω, while the blue beams on the right have frequency of 2ω. Waves 3 and 4 are the transmitted fundamental waves with one being an o-wave and the other an e-wave. Waves 5 through 7 are bound waves travelling with waves 3 and 4. Waves 8 and 9 are free waves generated at the $z = 0$ surface, as is the reflected wave 10. Waves 11 and 12 are the reflected free waves at $z = l$. Wave 13 is the total harmonic wave transmitted. *This figure is modified from [30].*

waves generated by each component can be better tracked. Additionally, by tracking the reflected waves at each surface, there is a more comprehensive understanding of how much energy entered the crystal and how much of the incident wave was frequency converted (compared to what exited the material) [28]. Another improvement originating from Pavlides and Pugh's work is the ability to track the energy at each crystalline surface, since the energy on both sides of each surface has to be the same. The end result of the 13-Beam Theory is a more accurate account of how much SHG was produced compared to what is transmitted for any unit cell structure. This accurate calculation of the SHG waves allows for more precision when calculating a d_{eff} from the SHG output.

One issue not completely addressed in 13-Beam Theory is the internal beam reflections due to the material having a high n. Since most of the time the material is surrounded by air which has a refractive index of about 1, a material with a high refractive index (for example, GaAs has a refractive index 3.48 at 1045 nm) will cause more light to be reflected on each surface than a material with a lower n due to Fresnel reflection [12, 31]. To address this issue with high refractive index materials, Murray *et al.* added six more beams to 13-Beam Theory to create 19-Beam Theory (see Figure 19) [30]. One of these new beams is the fully transmitted fundamental wave, while the other five are the internally reflected waves: two fundamental waves and three bound waves [30]. A higher n material would cause more of the harmonic waves to be reflected backwards (compared to a lower n material), which is not accounted for in the 13-Beam Theory. Thus, the 13-Beam Theory determines that less of the fundamental wave is converted to the SHG wave than the 19-Beam Theory, which in turn leads to undervalued calculations of the d-coefficients. The discrepancies between the two theories increase as n is increased.

Figure 20 shows a block diagram for the Maker Fringe experiment. The pump

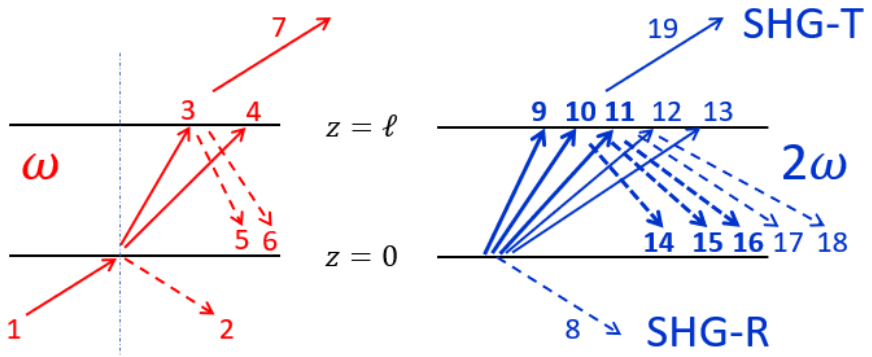

Figure 19: Maker Fringe 19-Beam Theory. The 19-Beam Theory adds five more internally reflected beams for both frequencies along with the transmitted fundamental beam. *This figure is modified from [30].*

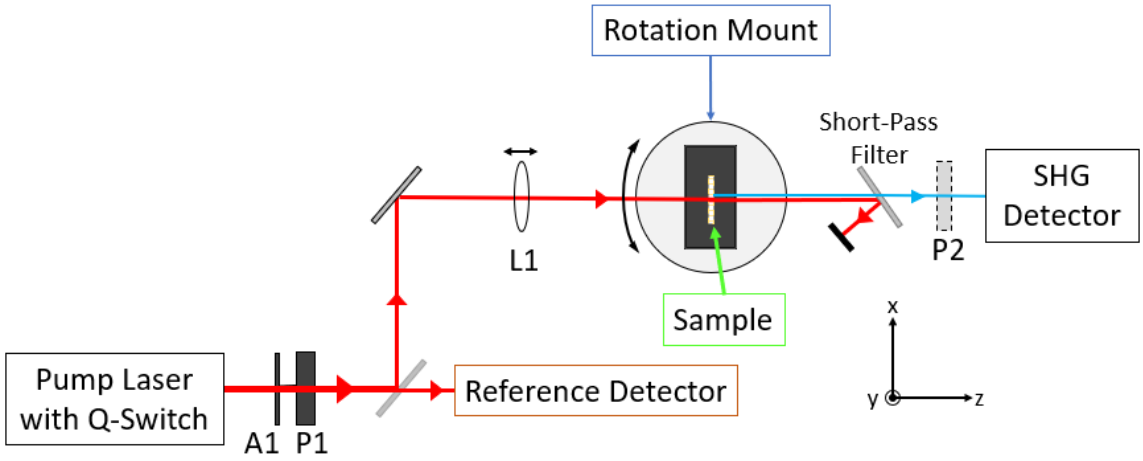

Figure 20: Block diagram of Maker Fringe experiment.

laser is Q-switched, which produces a train of short pulses. Attenuator A1 is used for power control, and the polarizer P1 polarizes the beam. The beam is focused at the sample by lens L1, which may be on a z-translation stage for minor adjustments. The pump is filtered out of the output, and the SHG detector collects the generated SHG waves produced by the sample. Polarizer P2 can be used to collect the different polarizations of the harmonic output.

The 13-Beam Theory and the 19-Beam Theory focus on the propagations and generations of waves, trying to provide the most accurate account for how much SHG light was generated, transmitted, and reflected [28, 30]. The complete derivations

of 13-Beam and 19-Beam Theories are located in [28] and [30]. Presented below are two of the methods for analyzing the transmitted SHG wave which allows one to determine d_{eff}.

Two common methods for conducting Maker Fringe experiment are the Rotation Method and the Intensity-scan (I-scan) Method. In the Rotation Method, the sample is rotated about the y-axis to a desired angle where it is fixed during data collection and then rotated about the sample surface normal 360° while the output is collected at set intervals [30]. Note that this rotation is only about the z-axis when the pump's angle of incidence is 0°. Each polarization of the SHG wave can be recorded separately, and these outputs resemble the Maker Fringes shown in Figure 16, though the number of fringes will vary depending on the sample. At different angles, d_{eff} is comprised of different d-coefficients with varying weights attached to them [30]. As such, this method allows multiple d-coefficients to be individually determined with just one scan of each polarization. Additionally, ratios of d-coefficients can be plotted, showing the relative strengths of the two coefficients for a given sample [30]. The Rotation Method is not used in this thesis due to time constraints, so further information will not be provided here.

The second method to measure d_{eff} is I-scan, whose name comes from varying the pump intensity at set intervals while leaving the sample in the same position. The sample is aligned about the vertical and sample surface normal either for maximum frequency conversion from the pump wavelength to the SHG wavelength or for measurement of specific d-coefficients. The pump intensity is varied, and the harmonic output is recorded at each pump intensity. To calculate d_{eff} and the d-coefficients, the following method is used.

The following equation is the general equation used to calculate d_{eff} for both the

Rotation Method and the I-scan Method:

$$I_{SHG} = \frac{2\mu_0\omega_p^2 L^2}{n_{SHG}n_p^2 c} d_{eff}^2 I_p^2 sinc^2\left(\frac{\Delta kL}{2}\right), \tag{51}$$

where μ_0 is the magnetic permeability of free space, the subscript p refers to the pump wave, the subscript SHG refers to the harmonic wave, and Δk is defined in Equation 38 [4]. Equation 51 originates from the solution to the coupled amplitude equations for all three waves (two pump, one SHG), derived in detail in [4]. Solving for d_{eff}, Equation 51 becomes

$$d_{eff} = \sqrt{\frac{cn_{SHG}n_p^2 I_{SHG}}{2\mu_0\omega_p^2 L^2 I_p^2 sinc^2\left(\frac{\Delta kL}{2}\right)}}. \tag{52}$$

To use Equation 52 with the I-scan data, a fitting parameter b_{fit} is used to relate the SHG output energy and the input intensity. As the pump intensity (I_{in}, in GW/cm^2) is increased linearly, the energy of the SHG signal (E_{SHG}, in nJ) increases in a quadratic fashion, where a fitting function can be plotted:

$$E_{SHG} = b_{fit} I_{in}^2, \tag{53}$$

where b_{fit} is the fitting parameter with units nJ/(GW/cm^2)^2 [22]. This b_{fit} parameter does not account for how much of the pump is reflected at the front surface and how much of the SHG wave is reflected at the back surface. These Fresnel losses are accounted for with a similar equation to Equation 53:

$$\frac{E_{SHG}}{T_s} = b_{true}\left(I_{in}T_p\right)^2, \tag{54}$$

where T_p is the single surface sample transmittance at the pump wavelength, T_s is the single surface sample transmittance at the SHG wavelength, and b_{true} has the

same units as b_{fit} [4, 22]. Multiplying both sides of Equation 54 by T_s, Equations 53 and 54 can be equated to obtain the value for b_{true} [22]:

$$b_{true} \left(I_{in} T_p\right)^2 T_s = b_{fit} I_{in}^2 \tag{55}$$

$$b_{true} = \frac{b_{fit}}{T_p^2 T_s}, \tag{56}$$

Equation 52 can then be rewritten to include this b_{true} parameter:

$$d_{eff} = \sqrt{\frac{b_{true} \lambda_p^2 n_p^2 n_s c \epsilon_0}{(2\sqrt{2}\pi^{7/2}) L^2 w_0^2 t_0 sinc^2(\frac{\sigma}{2})}}, \tag{57}$$

where λ_p is the pump wavelength, n_p and n_s are the refractive indices at the pump and SHG wavelengths, c is the speed of light, ϵ_0 is the permittivity of free space, L is the length of the sample, w_0 is the beam waist, t_0 is the temporal pulse width (FWHM), $\sigma = \pi L / L_c$, and L_c is calculated via Equation 44 [22]. Once d_{eff} is obtained, then individual d-coefficients are calculated based on crystal structure and orientation, using the method described in Section 2.1.2.1.

Equating Equations 52 and 57 shows what b_{true} represents:

$$b_{true} = \frac{\pi^{3/2} w_0^2 t_0 I_{SHG}}{2\sqrt{2} I_{in}^2}. \tag{58}$$

I_{SHG} is the on-axis intensity for the SHG wave. To convert from intensity to energy E_{SHG}, I_{SHG} is divided by the area of the beam waist πw_0^2 and the temporal pulse width t_0. Equation 58 then becomes

$$b_{true} = \frac{E_{SHG}}{I_{in}^2} \left(\frac{\sqrt{\pi}}{2\sqrt{2}}\right), \tag{59}$$

where the $\sqrt{\pi}/2\sqrt{2}$ is the conversion factor from a plane wave to a Gaussian wave [22]. The equations presented in this section provide a basis for the analysis method

used in this thesis for the Maker Fringe data.

2.2.2 Z-Scan

2.2.2.1 Z-Scan Overview

The Z-Scan experiment was introduced in 1989 as a simple yet accurate method of determining the nonlinear refractive index (n_2) of a material [24]. This determination is done using a setup similar to the one shown in Figure 21. In the Z-Scan method, a pulsed pump beam passes through a beam splitter (BS), where the reflected light waves are immediately collected by a detector (D1). The transmitted light waves are focused at a point, z_0, and then defocused before being collected by another detector (D2). The sample is placed on a translation stage with its center at z_0. The sample is then moved along the direction of propagation from $-z$ to z, hence the name Z-Scan. The position z is chosen such that the intensity at $\pm z$ is too low to induce a substantial effect from n_2 or β. The aperture in front of the second detector allows this setup to determine two different properties of the sample: closed aperture (CA) for n_2 and open aperture (OA) for β. Both methods use the normalized transmittance (D2/D1) plotted against sample position to determine the properties.

For the CA setup, the aperture allows a limited amount of the unobstructed beam

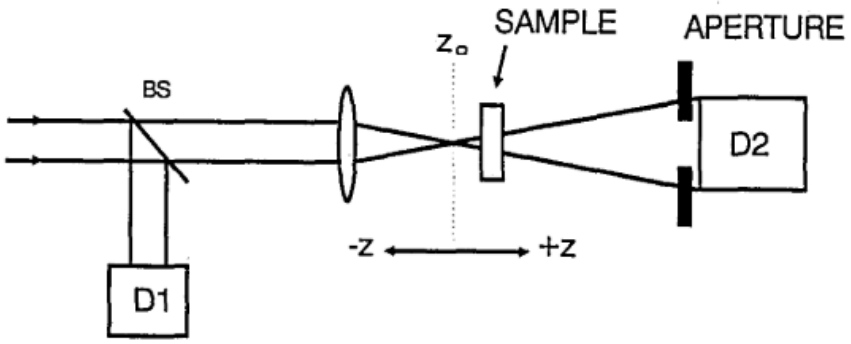

Figure 21: Block diagram of Z-Scan experiment. *This figure is modified from [24].*

to be collected by the detector. Since n_2 relies on high intensity, a Gaussian pump beam will induce a different n_2 in the center of the sample than on the edges since most of the energy is in the center. As the beam is focused, the intensity of the beam increases. As the sample is moved through z_0, it will act like a lens, with the center of the beam encountering a different refractive index due to the effects of nonlinear refraction (see Figure 22) [4]. For a positive n_2 material, the center of the beam travels slower through the material than the edges, causing the beam to be focused [4, 24]. On the $-z$ side of the experiment, the sample causes the beam to focus before z_0, which means it defocuses further from the aperture, leading to less of the beam passing through the aperture and being collected. On the $+z$ side of the experiment, the sample refocuses the beam after the beam starts diverging, allowing more of the beam to pass through the aperture. For a material with a negative n_2, the center experiences a lower refractive index than the edges, causing the beam to defocus as it exits, resulting in the opposite effects of positive n_2 [4, 24]. An example of the normalized transmittance for both positive and negative n_2 materials is shown in Figure 23 [24].

With this CA setup, it is possible to calculate β [32]. However, a simpler and more effective way to calculate β would be to completely open or to remove the aperture

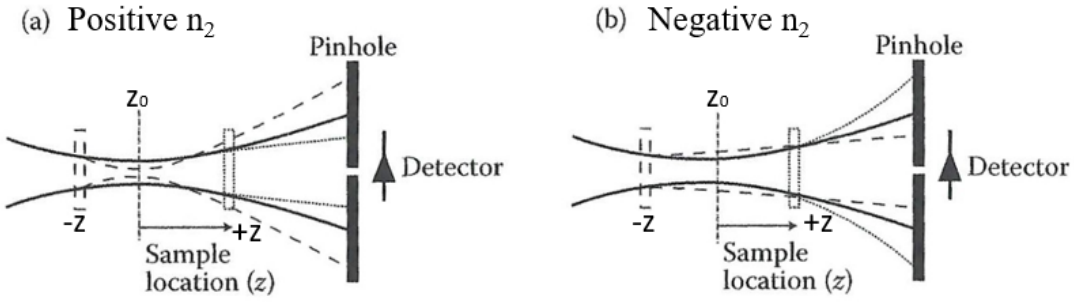

Figure 22: Material lensing due to nonlinear refractive index. This figure illustrates the material lensing caused by positive n_2 (a) and by negative n_2 (b) in the closed aperture Z-Scan experiment. Beam divergence is exaggerated for illustration purposes. *This figure is modified from [4].*

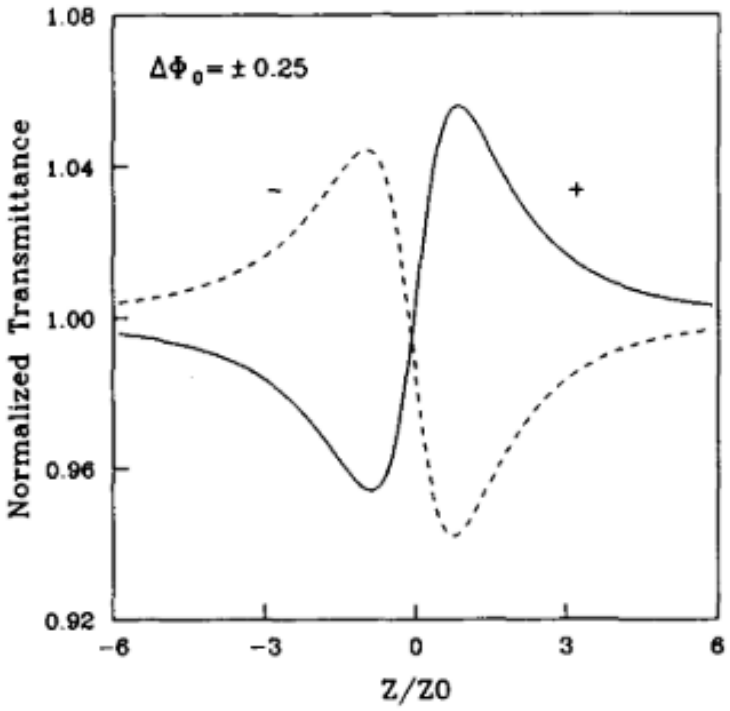

Figure 23: Example of normalized transmittance for closed aperture Z-Scan. This figure shows the general shape of the closed aperture Z-Scan normalized transmittance for positive n_2 (solid line) and negative n_2 (dashed line) materials. The location of highest intensity z_0 is located at $z/z_R = 0$. "z_0" in the figure is the Rayleigh range z_R. *This figure is taken from [24].*

entirely (the OA setup) [32]. Doing so allows the whole beam to be collected by the detector regardless of crystal position, removing the effect of n_2 and reducing the number of unknowns. The normalized transmittance is still plotted against sample position, but the plot takes on a different shape as seen in Figure 24. As the crystal approaches z_0, the intensity of the beam increases due to the decreased spot size. This increases the probability of multi-photon absorption and thereby decreases the number of photons that are transferred through the sample [4, 32]. As expected when the intensity decreases, the nonlinear absorption also decreases, leading to the symmetric nature of the graph about z_0.

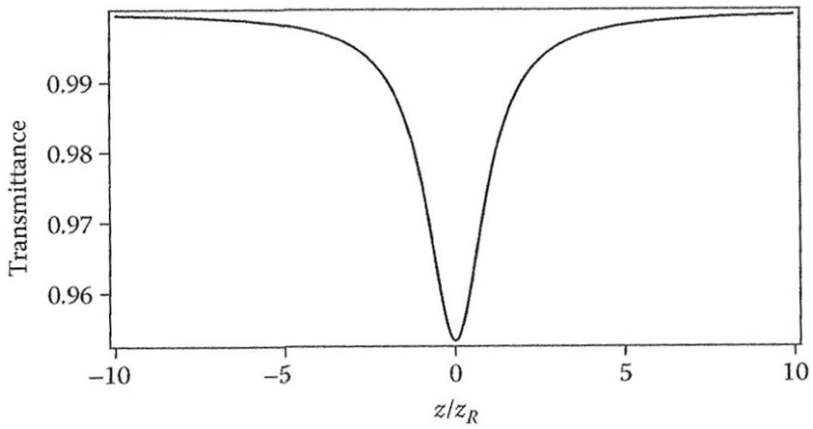

Figure 24: Example of normalized transmittance for open aperture Z-Scan. This figure shows the general shape of the normalized transmittance for an open aperture Z-Scan run. The location of highest intensity z_0 is located at $z/z_R = 0$. *This figure is taken from [4].*

2.2.2.2 Z-Scan Theory

The full derivation of the theory behind the Z-Scan technique has been done by Sheik-Bahae *et al.*, so only portions will be repeated here [23].

Nonlinear refractive index will be presented first, and the calculations for n_2 assume there is negligible nonlinear absorption. The electric field of a Gaussian beam propagating through the air is dependent on position in space z, radial distance from the center of the beam r, and time t, denoted $E(z, r, t)$. As the beam propagates through the sample, there will be a nonlinear phase shift:

$$\Delta\phi^{NL}(z, r, t) = \frac{\Delta\Phi_0}{1 + (z/z_R)^2} \exp\left(-\frac{2r^2}{w^2(z)}\right) \tag{60}$$

where $\Delta\Phi_0$ is the on-axis phase shift at the focus and is

$$\Delta\Phi_0 = k n_2 I_0 L_{eff}, \tag{61}$$

L_{eff} is the effective interaction length given by $L_{eff} = (1 - e^{-\alpha L})/(\alpha)$, α is the

absorption coefficient given by Equation 14, L is the length of the sample, I_0 is the on-axis peak intensity at z_0, z_R is the Rayleigh range, r is the radial distance from the center of the beam, and $w(z)$ is the radius of the beam at z with z_0 at w_0 [4, 23]. Additionally, the sample may linearly absorb part of the beam. Thus, the electric field exiting the sample E_e can be written as

$$E_e(z, r, t) = E(z, r, t)e^{-\alpha L}e^{i\Delta\phi^{NL}}, \tag{62}$$

where $e^{-\alpha L}$ is the effect of linear absorption, α is the linear absorption coefficient, and $e^{i\Delta\phi^{NL}}$ is the nonlinear phase shift [4, 23]. The electric field at the aperture E_a is

$$E_a(r, t) = E(z, r = 0, t)e^{-\alpha L/2}\Psi(z, r, \Delta\phi) \tag{63}$$

where $\Psi(z, r, \Delta\phi)$ is a function of beam radius, distance from sample to aperture, and phase, provided in detail in [23]. By spatially integrating $E_a(r)$ to the aperture radius r_a, the power transmitted through the aperture is [23]

$$P_T(\Delta\Phi_0(t)) = c\epsilon_0 n_0 \pi \int_0^{r_a} |E_a(r, t)|^2 \, r dr. \tag{64}$$

With $P_i(t)$ as the instantaneous input power within the sample and S as the aperture linear transmittance, the normalized transmittance can then be calculated:

$$T(z) = \frac{\int_{-\infty}^{\infty} P_T(\Delta\Phi_0(t))dt}{S\int_{-\infty}^{\infty} P_i(t)dt} \tag{65}$$

where $P_i(t) = \pi w_0^2 I_0(t)/2$ and $S = 1 - \exp(-2r_a^2/w_a^2)$, with w_a as the beam radius at the aperture [23]. When $T(z)$ has the shape shown in Figure 23, a simplification can be made which relates $|\Delta\Phi_0|$ to the difference between the peak and valley of T_N

(ΔT_{p-v}) [23]. If $|\Delta\Phi_0| \leq \pi$ [23],

$$\Delta T_{p-v} \approx 0.406(1-S)^{0.25}\,|\Delta\Phi_0|\,. \tag{66}$$

To measure β, the aperture in front of the detector is completely opened or removed, allowing the beam to be completely collected by the detector. For a sample that has both linear and nonlinear absorption, the intensity and phase shift exiting the sample are

$$I_e(z,r,t) = \frac{I(z,r,t)e^{-\alpha L}}{1+q(z,r,t)} \tag{67}$$

and

$$\Delta\phi = \frac{kn_2}{\beta}\ln\left[1+q(z,r,t)\right] \tag{68}$$

where α is the linear absorption, $q(z,r,t) = \beta I(z,r,t)L_{eff}$, and $L_{eff} = (1-e^{-\alpha L})/(\alpha)$ [23]. For $|q| < 1$, Equations 67 and 68 can be combined to write the electric field exiting the sample as an infinite sum of Gaussian beams [23]:

$$E_e = E(z,r,t)e^{\alpha L/2}\sum_{m=0}^{\infty}\frac{q(z,r,t)^m}{m!}\left[\prod_{n=0}(\frac{ik\gamma}{\beta}-1/2-n+1)\right]. \tag{69}$$

Integrating Equation 69 over r gives the transmitted power

$$P_T(z,t) = P_i(t)e^{-\alpha L}\frac{\ln\left[1+q_0(z,t)\right]}{q_0(z,t)} \tag{70}$$

where $q_0(z,t) = \beta I_0(t)L_{eff}/(1+z^2/z_R^2)$ and $P_i(t)$ is the same from the closed aperture calculations [23]. Time integrating Equation 70 and expressing it as an infinite sum, the transmittance equation used to determine β is [23, 33]

$$T_N(z) = \sum_{m=0}^{\infty}\frac{[-q_0(z,0)]^m}{(m+1)^{3/2}} = \sum_{m=0}^{\infty}\frac{[-\beta I_0(t)L_{eff}/(1+z^2/z_R^2)]^m}{(m+1)^{3/2}}. \tag{71}$$

2.3 Properties of the Examined Materials

This section will cover the relevant properties of the materials characterized as part of this thesis. Relevant wavelengths are 2090 nm and 1045 nm for the Maker Fringe experiment, and 1550 nm for the Z-Scan experiment. The order of the materials is as follows:

1. GaAs;
2. GaP;
3. The $GaAs_xP_{1-x}$ ternary compounds;
4. $Sn_2P_2S_6$; and
5. Zinc Selenide (ZnSe).

2.3.1 Gallium Arsenide (GaAs) and Gallium Phosphide (GaP)

Both GaAs and GaP are non-birefringent materials in the $\overline{4}$3m crystal class, which has a cubic unit cell structure (see Figure 25) [34]. As a result, their d-matrix is [4, 34]

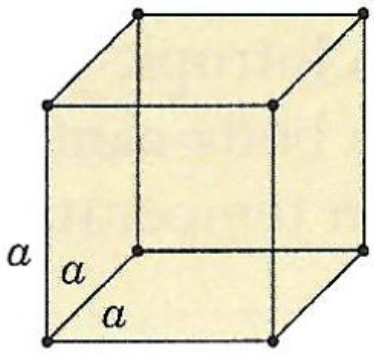

Figure 25: Unit cell structure of cubic crystal. The side lengths a, b, and c all equal each other. All three internal angles α, β, and γ equal 90°. *This figure is from [13].*

$$\overleftrightarrow{d} = \begin{pmatrix} 0 & 0 & 0 & d_{14} & 0 & 0 \\ 0 & 0 & 0 & 0 & d_{14} & 0 \\ 0 & 0 & 0 & 0 & 0 & d_{14} \end{pmatrix}. \tag{72}$$

Being non-birefringent, both of these are generally engineered to be QPM materials, having their orientation flipped every coherence length. However, the samples examined in this thesis are single crystal.

2.3.1.1 GaAs

The transmittance of GaAs as manufactured by a vendor is shown in Figure 26 [35]. From Figure 26, the differences between the thinner and thicker samples between the wavelengths 900 nm and 1200 nm indicates that there is appreciable linear absorption in that waveband. The Sellmeier equation for GaAs was formulated by Skauli *et al.*

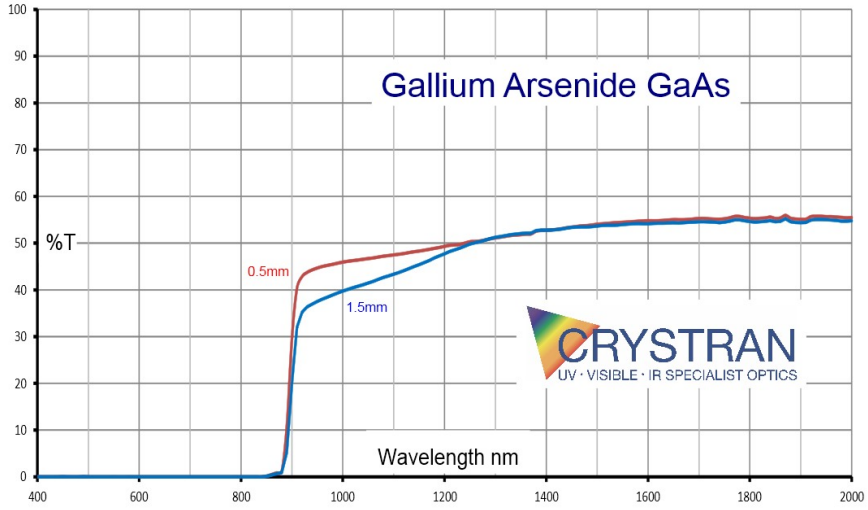

Figure 26: Transmission spectrum of GaAs. The red and blue lines show the difference in transmission between a 0.5 mm and a 1.5 mm sample. *This figure is from [35].*

in 2003:

$$\begin{aligned} n(\lambda)^2 &= 5.372514 + \frac{27.83972}{1/\lambda_1^2 - 1/\lambda} \\ &+ \frac{0.031764 + 4.350 \times 10^{-5}\Delta T + 4.664 \times 10^{-7}\Delta T^2}{1/\lambda_2^2 - 1/\lambda} \\ &+ \frac{.00143636}{1/\lambda_3^2 - 1/\lambda} \end{aligned} \tag{73}$$

where $\lambda_1 = 0.11313071 + 5.0564 \times 10^{-5}\Delta T$, $\lambda_2 = 0.08746453 + 1.913 \times 10^{-4}\Delta T - 4.882 \times 10^{-7}\Delta T^2$, $\lambda_3 = 36.9166 - 0.011622\Delta T$, $\Delta T = T - 22$ with T in degrees Celsius, and λ in μm [31]. Using this equation, the refractive indices for the wavelengths used in both experiments at room temperature are listed in Table 2 [31].

Table 2: Refractive Indices for GaAs used in this Thesis

1045 nm	1550 nm	2090 nm
3.480402	3.369709	3.334201

The d_{14} coefficient of GaAs used in this thesis was calculated by Skauli *et al.* in 2002 to be 94 pm/V at 4.1 μm [9]. Using Miller's Rule (Equation 35) results in a d_{14} of 107.7 pm/V at 2.09 μm [9, 20, 31]. Figure 27 shows n_2 for GaAs over a wide range of wavelengths, with n_2 at 1550 nm being approximately 3×10^{-4} cm^2/GW [5]. At shorter wavelengths GaAs has considerable nonlinear absorption, as seen in Figure 2 [5]. At 1550 nm, β is approximately 13 cm/GW [5]. With such a high β for these shorter wavelengths, GaAs is not desirable for use in optical devices below 1.7 μm.

2.3.1.2 GaP

The transmission spectra for GaP is shown in Figure 28 [36]. From Figure 28, GaP transmits about $58 - 59\%$ for the wavelengths of interest [36]. The Sellmeier

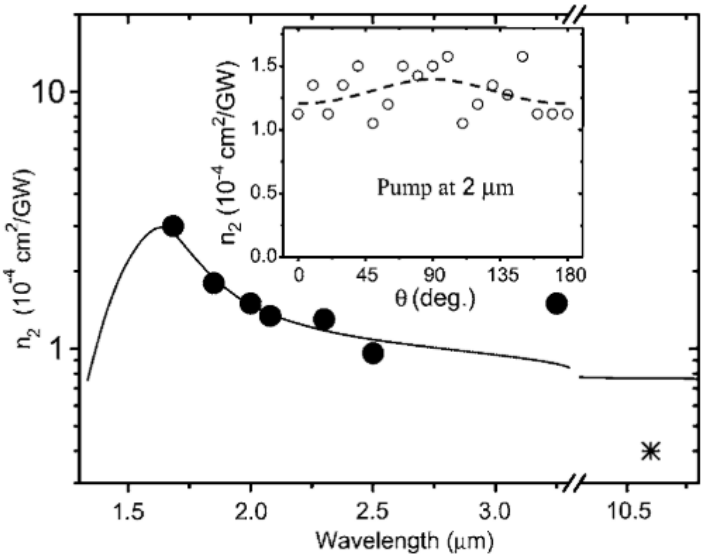

Figure 27: Nonlinear refractive index of GaAs. The theoretical (line) and experimental (dots) nonlinear refractive index n_2 for GaAs is shown from 1000 nm to $11,000$ nm, with polarization along the [1 1 0] plane of GaAs. The inset shows the variation of n_2 as the material is rotated at 2000 nm, with the circles being experimental and the dashed lines being the best fit of the experimental. *This figure is from [5].*

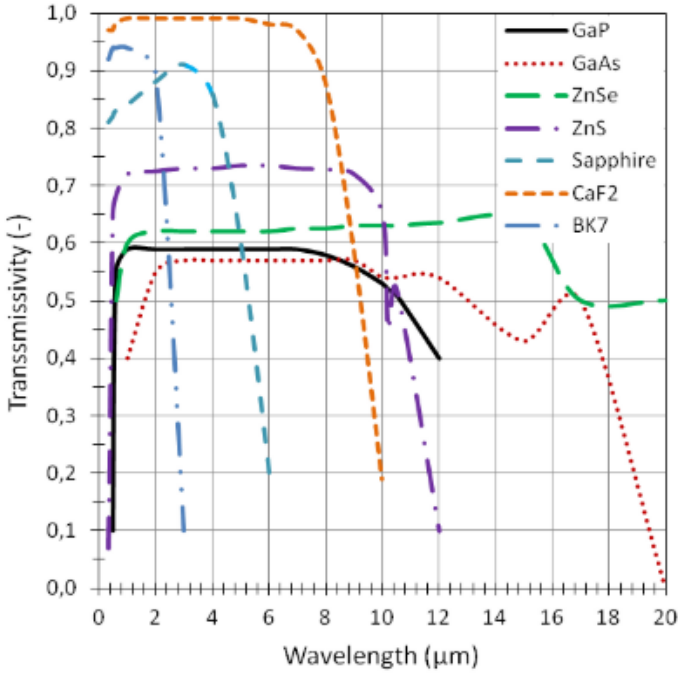

Figure 28: Transmission spectra for selected crystals. The transmission for GaP for $0.5 - 12$ μm is the black line. *This figure is from [36].*

equation for GaP is as follows:

$$n^2(\lambda) = A + \frac{B}{1-(0.0911014/\lambda^2)} + \frac{D}{1-(758.048/\lambda^2)}, \tag{74}$$

where $A = 10.926 + 7.0787 \times 10^{-4}T + 1.8594 \times 10^{-7}T^2$, $B = 0.53718 + 5.8035 \times 10^{-5}T + 1.9819 \times 10^{-7}T^2$, $D = 1504 + 0.25935T - 0.00023326T^2$, T is in Kelvin, and λ is in μm [37]. Thus, the refractive indices at room temperature for GaP used are listed in Table 3 [37].

Table 3: Refractive Indices for GaP used in this Thesis

1045 nm	1550 nm	2090 nm
3.107926	3.054845	3.035313

The d_{14}-coefficient used in this thesis is 70.6 pm/V at 1064 nm [8]. Scaling this using Equation 35, the d_{14} coefficient at 2090 nm is 53.1 pm/V [8, 20]. A couple values for β measured near 1 μm are 1.02 cm/GW around 780 nm and 0.2 cm/GW at 1064 nm [6, 7]. Note that these β values are at least one order of magnitude lower than GaAs's. As such, the value of β used in the Z-Scan experiment will be 0 cm/GW [38]. Also around 1550 nm, GaP's n_2 value has been calculated to be 1.2×10^{-17} m^2/W [39].

2.3.2 $\mathbf{GaAs_xP_{1-x}}$ Ternaries

The two $GaAs_xP_{1-x}$ ternary compounds examined in this thesis are $GaAs_{0.602}P_{0.398}$ and $GaAs_{0.74}P_{0.26}$, with the stoichiometries determined by the grower of the samples prior to being lent for this thesis. $GaAs_xP_{1-x}$ ternary compounds are commonly used as semiconductors or in solar cells, which do not rely on the same properties required for coherent light generation does. There does not appear to be any published NLO-properties of $GaAs_xP_{1-x}$ available in literature. Since their NLO properties have not been well characterized in literature, Vegard's Law is used to approximate the

relevant properties required to analyze the experimental data. Vegard's Law is an approximation theory for ternary compounds if the ternaries and the respective binary compounds have the same crystal structure [40]. Vegard's Law says that there is a linear relationship between the properties of the binaries and those of the ternaries (primarily applies to the dimensions of the unit cell structure) [40]. For example, if compound AB has side a at 1 arbitrary unit (a.u.) and compound AC has side a at 2 a.u., then the ternary $AB_{0.4}C_{0.6}$ will have side a be $1(0.4) + 2(0.6) = 1.6$ a.u. [40].

Vegard's Law will be extended to the refractive index and the "ideal" transmittance of the ternaries. Using the refractive indices from the previous section, the values for n for $GaAs_{0.602}P_{0.398}$ that will be used are listed in Table 4 [31, 37, 40].

Table 4: Refractive Indices for $GaAs_{0.602}P_{0.398}$ and $GaAs_{0.74}P_{0.26}$ used in this Thesis

	1045 nm	1550 nm	2090 nm
$GaAs_{0.602}P_{0.398}$	3.332168	3.244393	3.215243
$GaAs_{0.74}P_{0.26}$	3.383558	3.287844	3.256490

2.3.3 $Sn_2P_2S_6$

In literature, it is noted that SPS has a high transparency range between 0.53 μm and 8 μm, though no graph is provided [41, 42, 43]. SPS is a monoclinic crystal (see Figure 29) in the Pc space group (m point group) [13, 18, 44]. The d-matrix for point group m crystal is

$$\overleftrightarrow{d} = \begin{pmatrix} d_{11} & d_{12} & d_{13} & 0 & d_{15} & 0 \\ 0 & 0 & 0 & d_{24} & 0 & d_{12} \\ d_{15} & d_{24} & d_{33} & 0 & d_{13} & 0 \end{pmatrix}. \tag{75}$$

Anema *et al.* measured the d_{21} coefficient for SPS, which implies that SPS is a point group 2 [18, 41]. This is in contradiction to many other papers that state or imply that SPS is in the m point group, so Anema's d-coefficient findings will be ignored [11, 44, 42, 45]. Haertle *et al.* used the Rotation Method of the Maker Fringe

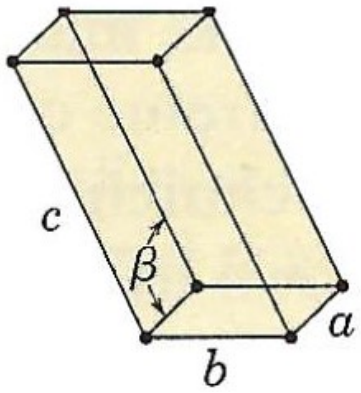

Figure 29: Unit cell structure of a monoclinic crystal. The side lengths a, b, and c do not equal each other. Internal angles α and γ both equal 90°, while β does not equal 90°. *This figure is from [13].*

experiment and calculated SPS's d-matrix at 1907 nm to be (in pm/V) [11]

$$\overleftrightarrow{d} = \begin{pmatrix} 12 \pm 1.5 & 2.0 \pm 0.3 & 6 \pm 5 & 0 & -1 \pm 4 & 0 \\ 0 & 0 & 0 & 1.8 \pm 0.5 & 0 & 1.7 \pm 0.2 \\ -1 \pm 4 & 3 \pm 2 & 4 \pm 3 & 0 & 6 \pm 5 & 0 \end{pmatrix}. \tag{76}$$

Note that Kleinman's symmetry is not always applied here (compare Equations 75 and 76), only when they were unable to separate the coefficients [45].

Since the monoclinic crystal structure does not have three orthogonal axes, Figure 30 is used to relate the crystal axes (a, b, and c) to a Cartesian coordinate system (x, y, and z), where the y- and b-axes are both perpendicular to the x-z plane shown [45]. Since SPS is a biaxial crystal, the axes x_1, x_2 (perpendicular to the x-z plane), and x_3 form another coordinate system for the refractive indices of SPS, with n_1 along the x_1-axis, n_2 along x_2, and n_3 along x_3 [45]. The angle α (indicatrix) is wavelength dependent, which means that the pump and the harmonic waves will have slightly different coordinate systems [45]. With the coordinate system presented in Figure 30, the relationship between the three axes' indices is $n_3 > n_1 > n_2$, which is

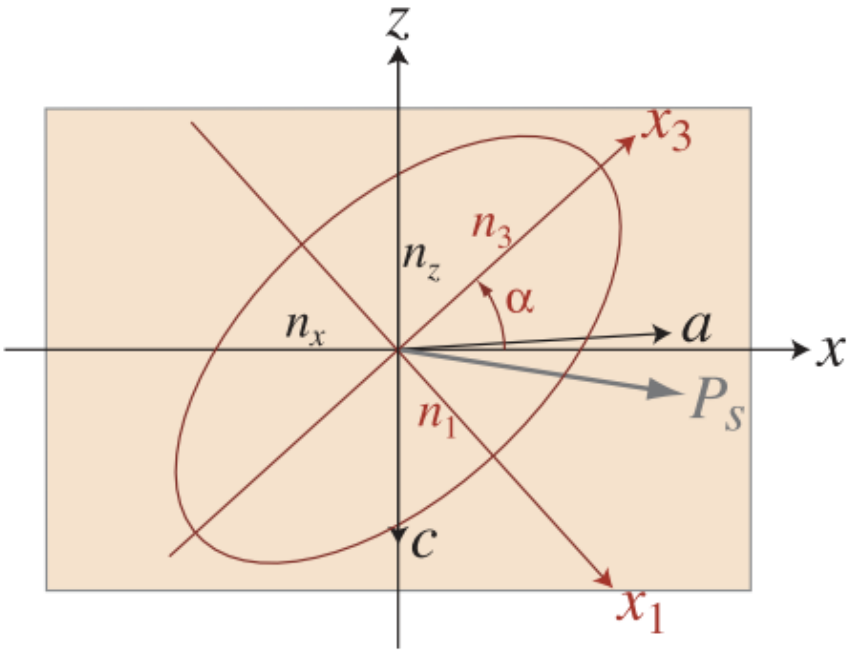

Figure 30: Coordinate systems of $Sn_2P_2S_6$. The graph shows the x-z plane, while the y-axis is perpendicular to the x-z plane. The crystal axes a and c are shown in the x-z plane, while the b-axis is perpendicular to the x-z plane and parallel to the y-axis. The refractive index axes x_1 and x_3 are shown, while x_2 is perpendicular to the x-z plane and parallel to the y- and b-axes. P_S is unimportant to this discussion. *This figure is from [45].*

not the standard where $n_3 > n_2 > n_1$ [45]. The Sellmeier equation for SPS is

$$n^2(\lambda) - 1 = \frac{S_1\lambda_1^2}{1-(\lambda_1/\lambda)^2} + \frac{S_2\lambda_2^2}{1-(\lambda_2/\lambda)^2}, \tag{77}$$

where the parameters S_i and λ_i for each n are listed in [45]. Thus, the refractive indices used in this thesis are listed in Table 5.

Table 5: Refractive Indices for $Sn_2P_2S_6$ used in this Thesis

	1045 nm	1550 nm	2090 nm
n_1	2.8317	2.7808	2.7636
n_2	2.7554	2.7085	2.6925
n_3	2.8677	2.8107	2.7916

Haertle *et al.* also measured two $\chi^{(3)}$ susceptibility coefficients at 1907 nm:

$\chi^{(3)}_{1111}$=17 ± 6 × 10^{-20} m^2/V^2 and $\chi^{(3)}_{2222}$=9 ± 3 × 10^{-20} m^2/V^2 [11]. Since both of these are for four waves with the same polarization, n_2 can be calculated using Equation 46, but β cannot since there is no imaginary part to these susceptibilities [4]. Using Equation 46, the nonlinear refractive indices for the x_1- and x_2-axes at 1907 nm are 6.266±2.211×10^{-5} cm^2/GW and 3.495±1.165×10^{-5} cm^2/GW, respectively [11, 45].

2.3.4 Zinc Selenide (ZnSe)

ZnSe is another NLO material examined in this research, though it is well established and is not related to the other groups. ZnSe was used to verify the setup of the Maker Fringe experiment and was subsequently put in the Z-Scan experiment. As such, its relevant properties will be listed below.

The transmission of ZnSe is shown in Figure 31, where the transmission for wavelengths between $1 - 2$ μm is about 70% [46]. Linear absorption is seen in the left-half of Figure 31, and has been measured (near the regions of interest) to be

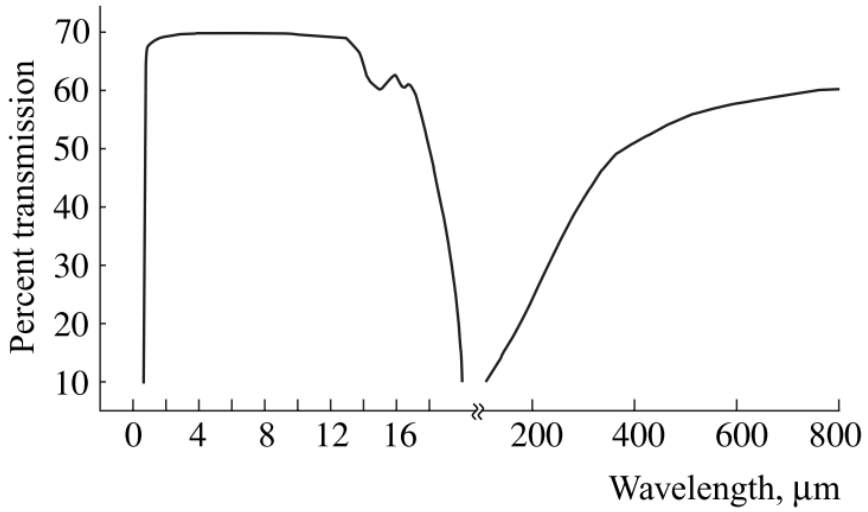

Figure 31: Transmission spectra of ZnSe. A graph showing the transmission spectra for ZnSe, for wavebands $0.5 - 22$ μm and about $100 - 800$ μm. *This figure is modified from [46].*

2×10^{-4} cm^{-1} at 1.3 μm and 7×10^{-4} cm^{-1} at 2.7 μm [46]. The Sellmeier equation for ZnSe was developed by Tropf in 1995 and will not be repeated here due to its complexity [47]. Using Tropf's Sellmeier equation, the relevant refractive indices at room temperature are listed in Table 6 [47].

Table 6: Refractive Indices for ZnSe used in this Thesis

1045 nm	1550 nm	2090 nm
2.484092	2.455559	2.444954

Since ZnSe is in the same crystal class as GaAs, it too only has d_{14} [8, 48]. The value for the d_{14} coefficient used in this thesis is 53.8 pm/V for the SHG process converting 852 nm to 426 nm [8]. Using the Miller's Δ_{14} value found in [8], d_{14} at 2090 nm is 35 pm/V [8, 20]. Figure 32 shows the n_2 values for wavelengths 0.8 μm to 2.5 μm [49]. From the figure, n_2 is approximately 1.00×10^{-5} cm^2/GW.

Li *et al.* compiled published data on different β values for ZnSe in 2022 [50]. The closest usable β value for this thesis is < 0.005 cm/GW at 1270 nm, calculated using a poly-crystalline ZnSe sample [50]. Li *et al.* showed a single ZnSe sample would

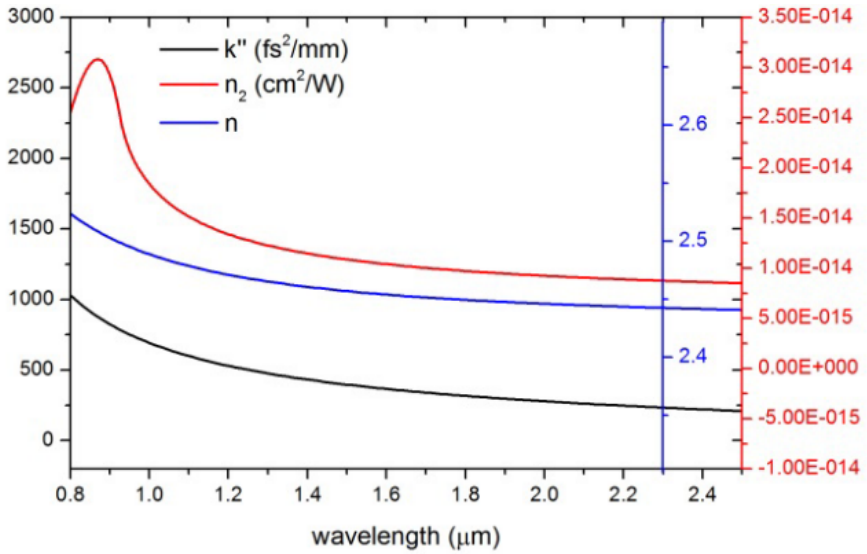

Figure 32: Dispersion, refractive index, and nonlinear refractive index of ZnSe. The black line is the dispersion (k'') of ZnSe, the blue line is the refractive index n, and the red line is the nonlinear refractive index n_2. *This figure is from [49].*

be about 1.7 times a poly-crystalline sample, so the β value at 1270 nm would then be < 0.085 cm/GW [50]. The other β values presented are for shorter wavelengths, decreasing in value as the wavelengths increase [50]. Using this downwards trend, β is negligible at 1550 nm for ZnSe.

III. Methodology

This chapter will describe the methods and procedures used to characterize the nonlinear properties using the two experimental methods: Maker Fringe and Z-Scan. Afterwards, it will cover the specifics of the samples used during each experiment.

3.1 Maker Fringe Experiment

A diagram of the Maker Fringe experiment is shown in Figure 33 and a photograph of the setup is in Figure 34. A Holmium:Yttrium-Aluminum-Garnet (Ho:YAG) crystal creates the 2.09 μm laser, which is Q-switched to generate pulses of 26.3 ns (measured FWHM) at a rate of 1000 Hz. A beam stability test was conducted over the course of an hour, and based on the maximum and minimum during that hour the power fluctuates by at most 3%. An M^2 measurement (how Gaussian the beam is) was also performed on this laser. The x-axis has an M^2 of 1.06, and the y-axis has an M^2 of 1.02, with a perfectly Gaussian beam having an M^2 of 1.

The pump passes through an attenuator (A1) and waveplate (P1) for power control and for horizontal polarization. Afterwards, the beam is split in two directions by a

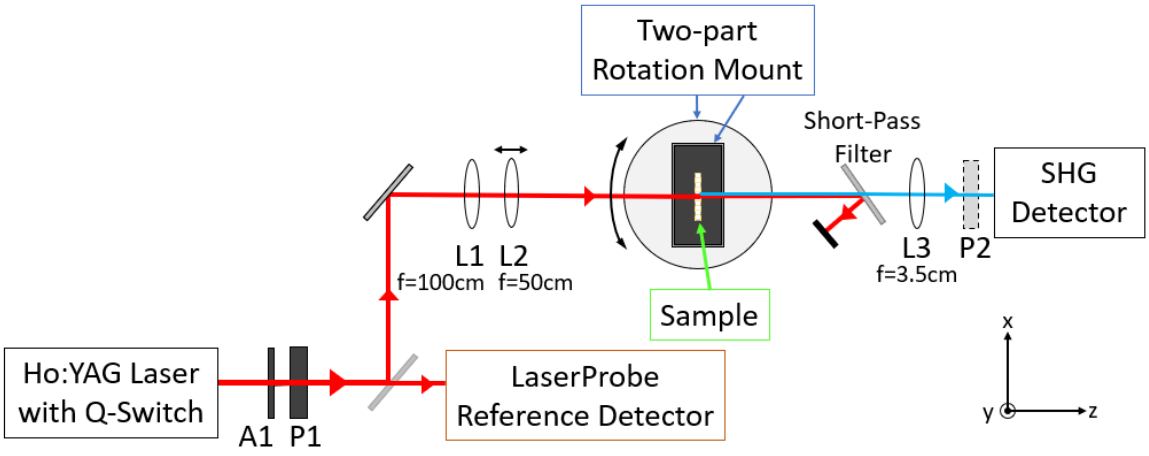

Figure 33: Block diagram of Maker Fringe experimental setup.

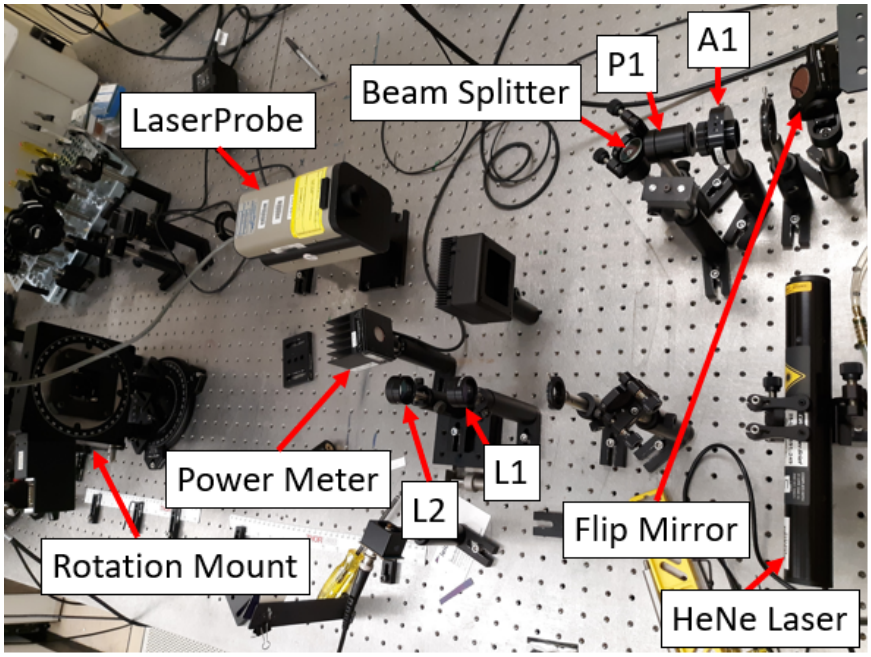

Figure 34: Picture of Maker Fringe experimental setup. The HeNe laser was used for alignment, and was directed down the path using the flip mirror. Not seen behind the rotation mount is the short-pass filter, L3, P2, and the SHG detector. The pump laser is to the right of A1 and the flip mirror.

beam splitter. The straight path lets 58.9% of the beam be collected by the *LaserProbe* Rm-6600 Universal Radiometer to monitor the power going into the sample. The other path directs the other 41.1% of the beam towards the sample, where 35.5% of the initial beam intensity is incident on the sample after the turning mirrors and lenses L1 and L2. L1 is the collimating lens with a focus of 100 cm, and L2 is the focusing lens with a focus of 50 cm. Together, these lenses produce an elliptical beam waist of 145 $\times$ 131 μm (measured $1/e^2$). L2 is on a z-translation stage to move z_0 if needed without changing the size of the beam waist. The beam passes through the sample mount, with the sample located at the beam waist. After transmitting through the sample, the pump is deflected by a short-pass filter and dumped while the SHG output is focused with a 3.5 cm ZnSe lens L3 (behind the rotation mount in Figure 34) onto the DET36A Si-based Detector by *ThorLabs*, transmitting 66.9%

of the harmonic wave [12, 47]. This detector is connected to the *LeCroy* LC584AL oscilloscope, where it collects the peak-to-peak voltage of the SHG signal. When separating the output by polarization, a polarizer (P2) is placed between L3 and the detector, and data for each polarization is then recorded separately.

The samples are housed in easily removable housing units made with a 3D printer, as seen in Figure 35. The samples are held in with clay, which does require the samples to be cleaned when irradiating the part of the sample held with clay earlier. A 5.5 mm diameter opening in the center allows the sample to be irradiated by the pump. These housing units are placed within a tip-tilt stage in the center of the sample mount (see Figure 36). The tip-tilt stage accounts for small discrepancies among the removable housing units, so that the front face of every sample is in the same plane. The sample mount holding the tip-tilt stage is a full 360° rotation

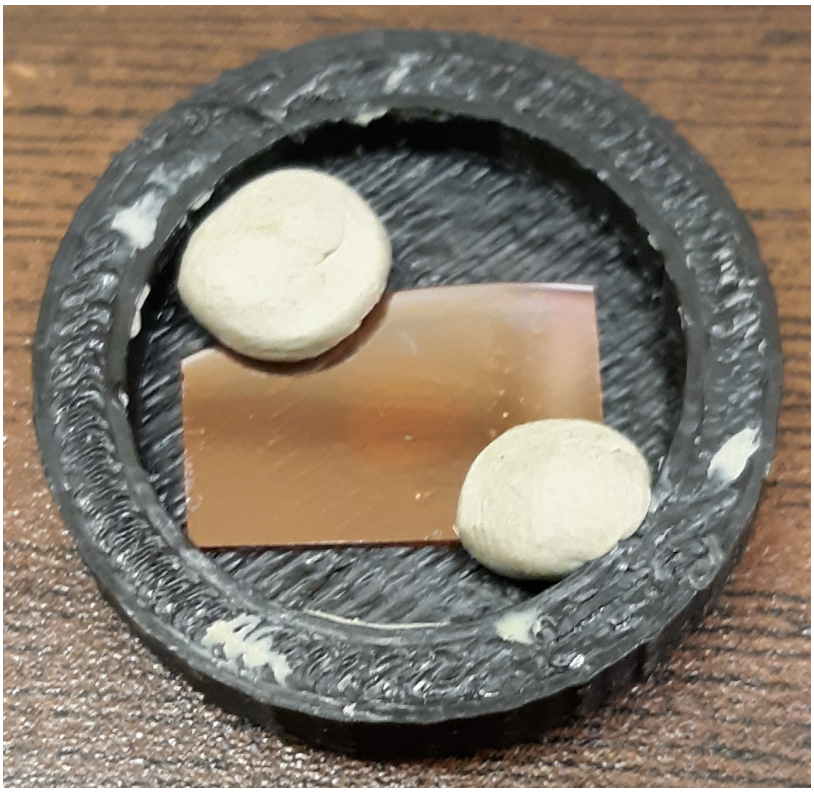

Figure 35: Maker Fringe sample housing unit. The GaP sample is housed within this unit.

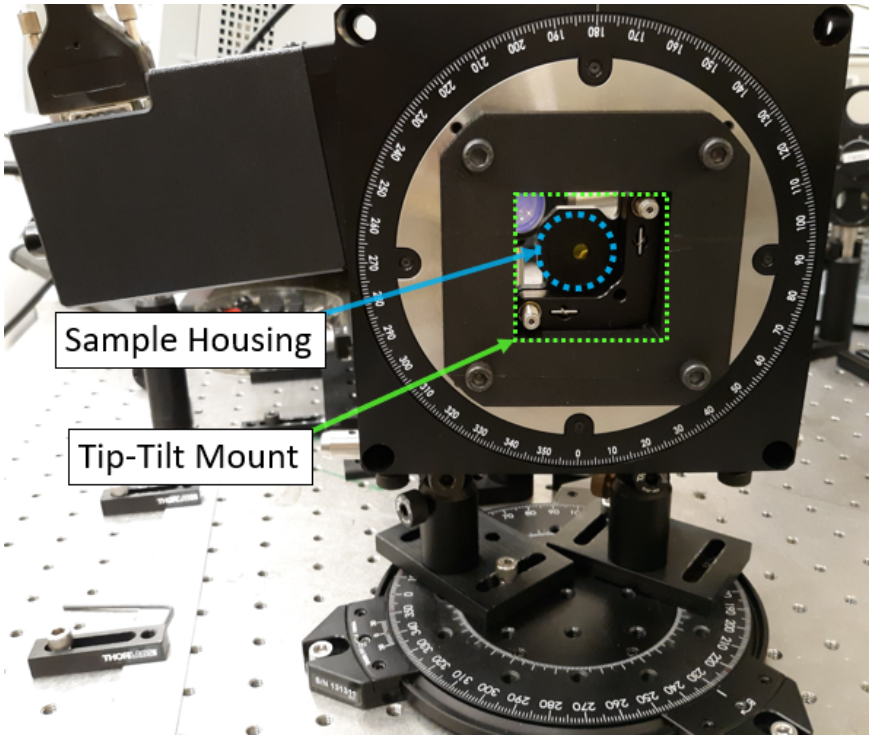

Figure 36: Rotation mount for the Maker Fringe experiment. The sample housing and tip-tilt mount are highlighted for clarity.

mount, allowing for full rotations about the sample surface normal. The 360° rotation mount allows the rotation method to be accomplished, and is convenient for the I-scan method. This 360° mount is connected to a *Newport* Motion Controller/Driver SMC-100 series to allow for computer control. Additionally, this mount is placed on another rotation mount, allowing the sample to be rotated about the y-axis. Together, these mounts allow the sample to be rotated without changing the location the beam enters the sample to allow for accurate data collection amongst the samples.

A ZnSe sample was used to calibrate the SHG detector to the reference detector, since the SHG detector signal is recorded as a peak-to-peak voltage. At varying pump powers, the SHG detector recorded a peak-to-peak voltage and then was swapped with the reference detector which recorded the average SHG power. The data for this calibration is shown in Figure 37. Thus, 1 V peak-to-peak corresponds to 19.14 μW

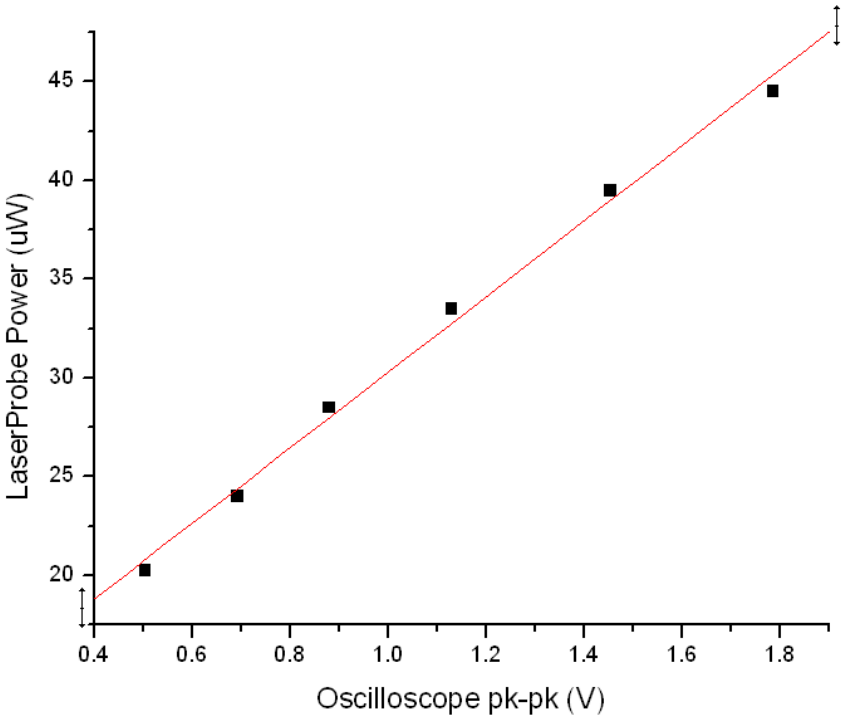

Figure 37: Calibration data for the output detector. The data points (squares) and the fit (line) of the output detector are plotted, with the output detector's signal on the x-axis and reference detector's signal on the y-axis.

of average power.

L3 had its transmittance calculated instead of measured, which could be done since it was uncoated and a single material. A power meter was placed at different points along the beam path to measure the pump losses from the other lenses, mirrors, and filters. The pump, however, is at 2090 nm, whereas the wavelength L3 experiences is half that at 1045 nm. Unfortunately, a 1045 nm laser was unavailable, and the spectrophotometer could not measure the transmittance due to the short focal length of L3 interfering with the device. As a result, the transmittance of L3 for the SHG signal had to be calculated. Using Equations 10 and 11 and calculating the refractive index of the lens to be 2.485 at 1045 nm, the transmittance of the SHG signal through L3 is 66.9% [12, 47]. Since the surfaces are not parallel or planar, multiple internal reflections can be ignored. Since this lens was professionally made and polished and

was stored properly, it is assumed that any losses due to scattering or absorption are negligible. Additionally, any pump light that passes through the short-pass filter in front on L3 is not intense enough to produce SHG within L3 for any pump intensity used during testing.

The I-scan Method is used to determine the d-coefficients. To maximize the SHG output, the sample is rotated about its normal and about the vertical, and if needed the L2 is shifted forwards or backwards. Once the SHG is maximized, the sample's final position is recorded so that it can be related to its unit cell orientation and its refractive index coordinate system during analysis. The input power is varied at set intervals, and data points are taken at each interval. One data point consists of the average peak-to-peak voltage of 5000 samples from the oscilloscope and the corresponding power from the reference leg during the sample collection.

Once sufficient data points for a crystal are collected, the units of the data points need to be converted before being fit to a parabolic function. The ZnSe calibration mentioned earlier resulted in a peak-to-peak of 1 V on the oscilloscope corresponding to 19.14 μW of average power. This power is divided by 1000 pulses per second to obtain the output energy per pulse E_{SHG}.

To get the pump intensity into the sample (I_{in}) from the average power off the reference detector, the average power is first multiplied by 380/630 to obtain the average power going into the sample, where 630 mW on the reference detector corresponds to 380 mW of average power irradiating the sample. Then it is divided by 1000 pulses/s to obtain the energy per pulse. The energy per pulse is then divided by the temporal pulse width t_0 to get the peak pulse energy. Finally the peak pulse energy is divided by the area of the beam waist πw_0^2 to obtain I_{in}. The following equation summarizes

the process from average reference power P_{ref} to I_{in}:

$$P_{ref}\left(\frac{38}{63}\right)\left(\frac{1}{1000}\right)\left(\frac{1}{t_0}\right)\left(\frac{1}{\pi w_0^2}\right) = I_{in}. \tag{78}$$

The t_0 value used is the measured pulse width of 26.3 ns (FWHM) multiplied by $\sqrt{\pi}$ to account for a Gaussian pulse instead of a square pulse and by (1/1.66511) to convert from FWHM to $1/e$ radius [22]. Since the beam waist was measured as $1/e^2$ radius instead of $1/e$, the value for w_0 used is $\sqrt{145 \times 131}/\sqrt{2}$ μm, where $1/\sqrt{2}$ is the conversion factor from $1/e^2$ radius to $1/e$ radius, and 145 and 131 are the radii along the long- and short-axes in μm, respectively [22].

Now, the converted data points are plotted to find b_{fit} in Equation 53, which is done using Matlab. After adjusting b_{fit} to b_{true} with Equation 56, d_{eff} is calculated using Equation 57, via Microsoft Excel code detailed in Appendix B.2.1. The non-birefringent materials all only have one d-coefficient (d_{14}), so the same method of extracting d_{14} from d_{eff} is used for all of them. The full method of calculating the d-coefficients is explained in Appendix A.

For the monoclinic crystals, the method is altered slightly. Since they are biaxial crystals, the orientation of the sample matters since the refractive index changes on orientation. Since they are birefringent, the SHG wave will propagate in a different direction than the pump wave, though this effect is ignored in this thesis. The differences in analysis up through calculating d_{eff} are detailed in Appendix B.2.2. Since d_{eff} is likely dependent on multiple d-coefficients, individual d-coefficients may be determined if enough runs at different orientations are collected. Extracting individual coefficients requires using Equation 34.

3.2 Z-Scan Experiment

A diagram of the Z-Scan experiment is shown in Figure 38, and a picture of the setup is Figure 39. A *Light Conversion* Pharos PH1-10-1000-10-10-SP generates the 1064 nm beam, which enters the OPA device, a *Light Conversion* Orpheus-HP. This OPA is pumped with the *Pharos* beam and outputs a varying range of wavelengths and pulse widths, controlled via a computer. With the desired wavelength and a pulse width of 120 fs (FWHM), the beam exits the OPA and encounters a beam splitter. This splitter sends part of the beam to the reference detector and the rest towards the sample. The attenuator (A1) before the reference detector is to prevent the detector from being saturated. Both the reference detector and the sample detector are *ThorLabs* PDA50B2 amplified detectors, rated for $800-1800$ nm. The A2 variable attenuator controls the power incident on the sample. The beam passes through the sample, the aperture, and the A3 attenuator before being collected by the sample detector. The samples are placed in a housing unit shown in Figure 40. The housing is placed on a three-axis translation stage, allowing the sample to travel along the

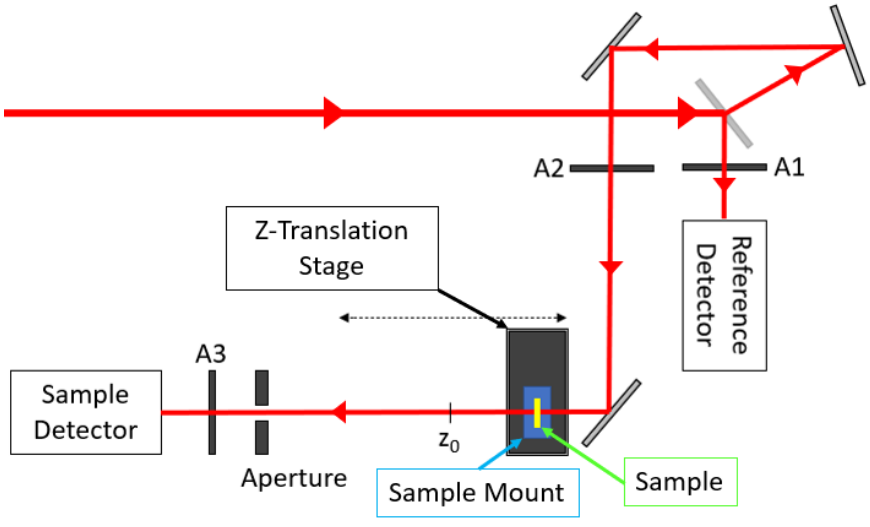

Figure 38: Block diagram of Z-Scan experimental setup.

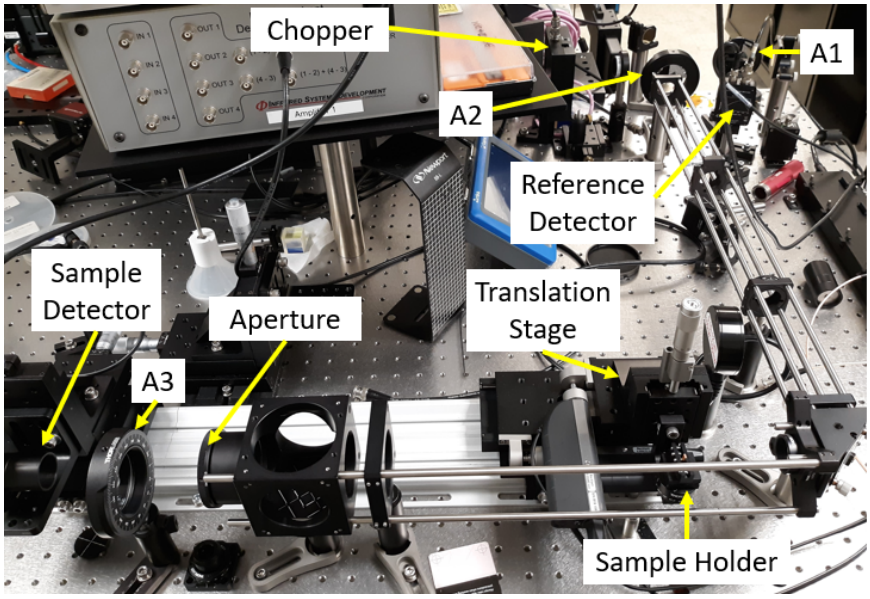

Figure 39: Picture of Z-Scan experimental setup. The pump passes through the chopper before reaching the beam splitter, which is obscured by Attenuator 1 (A1). Part of the pump is directed into the Reference Detector, and the other part is directed by two mirrors to A2. The chopper is off and open while running the experiment, but is turned on only when measuring the power going into the sample.

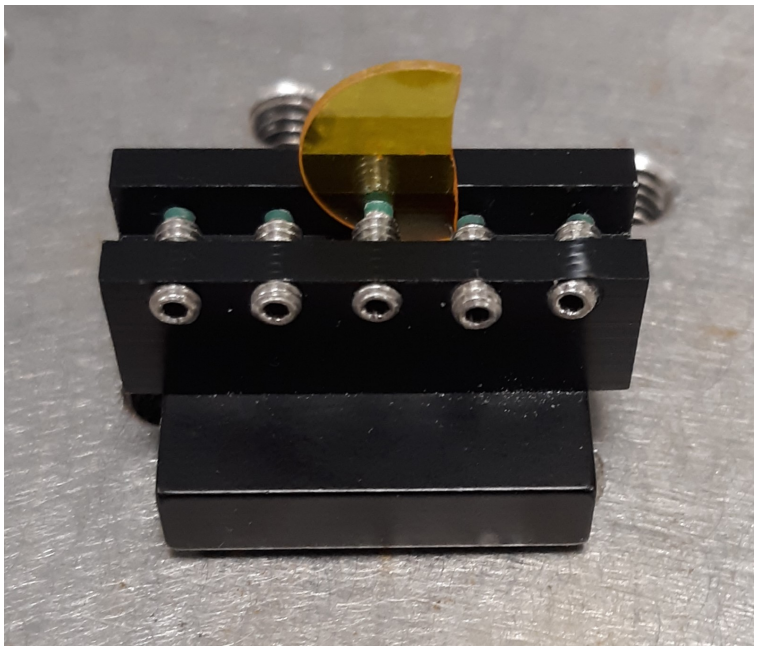

Figure 40: Picture of Z-Scan sample housing unit. The sample being house is the ZnSe sample.

beam through z_0 while starting and ending far enough away from z_0 that the effects of n_2 and β are negligible. The translation stage is controlled by a *Newport* Motion Controller Model XPS-D. The translation stage moves along the z-axis from 0 to 40 mm, where 0 mm is not the location of the focus z_0; z_0 was not directly measured at any point during testing but can be inferred from the data plots. The aperture is either set to open or closed for β or n_2, respectively. A3 is utilized to match the intensity of the signal from the sample detector to that of the reference detector. The two detectors are connected to an HF2LI Lock-in Amplifier by *Zurich Instruments AG*, which is used to receive and average the signals before further analysis and to isolate the desired frequency for collection. Via LabView, the sample signal is then divided by the reference signal to produce the normalized transmittance plots. These plots are then taken elsewhere for fitting using Matlab and the fitting functions below.

The wavelength 1550 nm was chosen to compare the 2PA between GaAs and the ternaries. This was the only wavelength examined due to the limited access to the Z-Scan experiment. Before each run, the sample was placed at either end of the translation stage. If needed, the power going into the sample was changed using A2, but the power going into the reference detector was never changed. Then, A3 was used to match the live signal from the sample detector to that of the reference detector, as best as possible.

One of the factors to consider when analyzing the data is the pump/OPA stability. Two GaAs runs were completed while the pump was stable; however, in the week prior to performing the rest of the Z-Scan experiments, the room in which the experiment was located heated above 90°F. The excessive heat affected the OPA system, altering the alignment of some component within the Orpheus-HP container. This misalignment within the OPA system led to the pump intensity fluctuating for the remainder of the Z-Scan runs. When starting to test with the unstable pump, it

would frequently drop in average power by 20% from the maximum level which lasted at most one second. By the end of testing, the pump instability increased to the point where it would drop by at most 60% of maximum average power. The frequent power drops are an issue since the reference detector does not have the sample in front of it like the other detector. Since both $\chi^{(3)}$ properties are intensity dependent, these fluctuations in intensity result in the sample detector fluctuating more than the reference detector, leading to more noise in the data. The purpose of the reference detector is to compensate for changes in intensity from the pump. However, when the pump is frequently fluctuating in intensity, the noise created by the frequent dips and spikes in T_N can negatively impact the analysis, leading to incorrect results. Due to time constraints, the OPA could not be realigned before running the experiment, since the day after the last runs were completed the setup was moved to another location and was not set up in time for follow-up runs.

Before determining n_2 with the CA setup, β was first determined with the OA setup, in case the sample has nonlinear absorption at 1550 nm. To calculate β, the normalized transmittance plots should have the shape shown in Figure 24 and should be symmetric about z_0. The recommended values for the minimum of T_N are between 0.95 and 0.77. The minimum being higher than 0.95 T_N might be indistinguishable from the noise. The minimum being lower than 0.77 T_N leads to scenarios similar to Figure 41. The fit curve starts increasing around z_0, and the lower the T_N value is at z_0, the higher the fit curve will spike. As such, any fits that result in the center spiking upwards will not used. For the runs that resulted in T_N dropping too low for Equation 71, additional runs were performed at a lower power. As mentioned earlier in this section, the position of z_0 was not measured. While this does make z_0 a fit parameter, runs conducted on the same day need to have the same location since the location was not altered between runs, with one exception explained in Section 4.2.

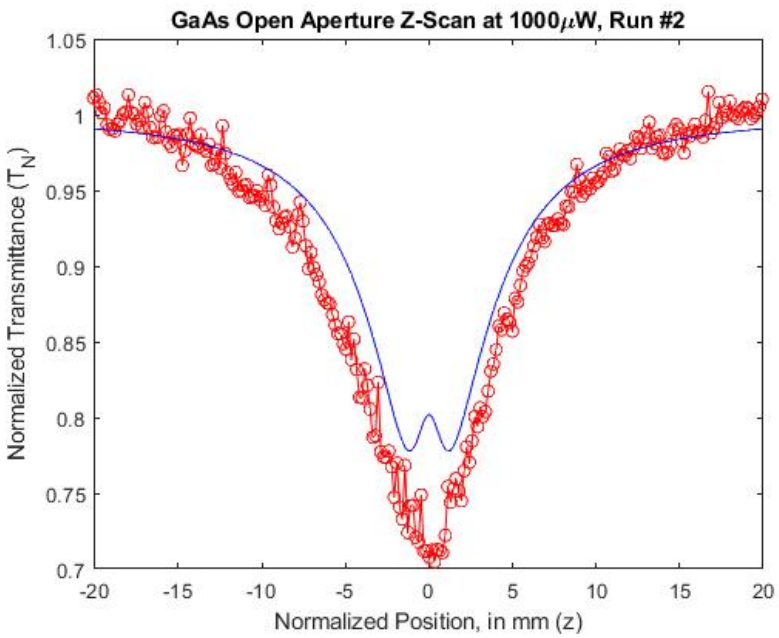

Figure 41: Example of incorrect open aperture fit due to the normalized transmittance being too low. Note how the fit function (blue line) increases near z=0 instead of following the data to 0.71 T_N.

Equation 71 is used to fit the normalized transmittance plots and find β, repeated here:

$$T_N(z) = \sum_{m=0}^{\infty} \frac{[\beta I_0(t) L_{eff}/(1+z^2/z_R^2)]^m}{(m+1)^{3/2}},$$

where $L_{eff} = (1-e^{-\alpha L})/(\alpha)$ and $z_R = \pi\omega_0/\lambda$. While the sum goes to $m = \infty$, it was deemed sufficient (and efficient) to have the sum go to $m = 10$. I_0 is calculated by

$$P_{avg}\left(\frac{1}{\#pulses/s}\right)\left(\frac{1}{t_0}\right)\left(\frac{1}{\pi w_0^2}\right) = I_0, \tag{79}$$

where P_{avg} is the average power per second incident on the sample and t_0 is the temporal pulse width ($1/e^2$). Since w_0 was not measured, it too is a fit parameter. However, like with the z_0, w_0 should not change in between runs when the pump is stable.

Matlab was used to fit Equation 71 to determine β, w_0, and z_0. The specific

function in Matlab used is the *lsqcurvefit* function, where β and w_0 are the parameters the function fits. This function uses the least squares method to determine the best fit for the specified variables, in this case β and w_0. Since z_0 is tied to the data which had to be read into Matlab, a *for* loop is used to shift the position of z_0 by set amounts while the *lsqcurvefit* function fits the data at each step. One of the outputs of the *lsqcurvefit* function is a parameter called "resnorm", which outputs the squared norm of the error between the fit and the data. The lowest resnorm was used to determine the best fit for the parameters. Since the pump configuration was not altered in between runs, w_0 and z_0 should be consistent in between runs, though the pump instability may slightly alter them. The w_0 and z_0 parameters are then used for all runs for that day, and the *lsqcurvefit* function is then used to find β.

With β calculated, now n_2 can be determined. Should the sample have negligible β and a $T(z)$ with a similar shape as either curve in Figure 23, Equation 66 will be used to find $|\Delta\Phi_0|$ before using Equation 61 to find n_2. To use these equations, the z_0 location should be where $T_N(z)$ is the same as the $T_N(z)$ value at z_0 in the OA plot, since the sample cannot focus or defocus the beam when the beam is already at its focus.

For the samples that have an appreciable β, this method will not work as the $T_N(z)$ plots will resemble more the OA plots. However, instead of using Equation 64, the following equation will be used:

$$T_N(z) = 1 + \frac{8\pi}{\lambda}\frac{n_2 I_0 L_{eff}(z/z_R)}{[(z/z_R)^2+9][(z/z_R)^2+1]} - \frac{\beta I_0 L_{eff}[(z/z_R)^2+3]}{[(z/z_R)^2+9][(z/z_R)^2+1]}, \qquad (80)$$

where λ is the wavelength of the pump and L_{eff}, z_R, and I_0 are the same as in the OA experiment [33]. The derivation behind Equation 80 from Equation 64 is done using articles by Rhee *et al.* and by Yin *et al.* and will not be repeated here [51, 52].

Again, Matlab is used to fit the data to Equation 80, using the same *lsqcurvefit*

function. Inputting the β, w_0, and z_0 values from the OA runs, the *lsqcurvefit* function only needs to fit n_2. However, when discrepancies arise from the OA fits of w_0 and z_0, Equation 80 is used to help determine w_0 and z_0.

3.3 Specifics of the Materials Examined

This section will cover the specifics of the samples used in both experiments, starting with the common materials (ZnSe, GaAs, and GaP). Two different stoichiometric $GaAs_xP_{1-x}$ ternary sets were obtained for this thesis. There was only one SPS sample was obtained for this thesis. All samples were measured with a *Starrett* F2730IQ profilometer, which measures the thickness to within one micrometer. The transmittance of all the samples was measured using the *Varian* Cary 5000 Spectrophotometer. Equation 14 was used to determine the absorption coefficients at 1550 nm for use in the Z-Scan experiment (Equations 71 and 80). However, if the transmittance measured is larger than the Fresnel-limited transmittance calculated via Equation 15, an α of 0.01 cm^{-1} will be used instead since α should not be negative for these materials.

3.3.1 Common Materials: GaAs, GaP, ZnSe

The first of the common samples is GaAs, with a picture of the two GaAs samples used in Figure 42. The 12.5 × 10 mm piece (left) was from a polished GaAs wafer left over from other experiments, and looks as though it was not damaged if used (except possibly around the edges). The 10.5 × 5.5 mm sample (right) was also a left-over piece of GaAs from a different wafer but has some surface damage in the middle, though none is visible on the reverse side. Both samples came from vendors and are z-cut, meaning that the z-axis is the same as the normal vector for the flat surface. The larger sample is 347 ± 1 μm thick, while the smaller sample is 377 ± 1

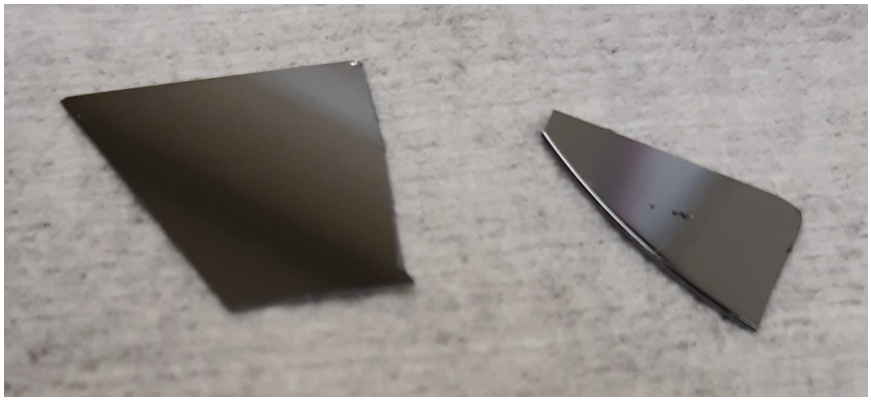

Figure 42: Picture of the GaAs samples. The left sample was used for the Maker Fringe experiment, and the right sample for the Z-Scan experiment. Note the surface damage on the right sample. Also note that both samples are reflecting the wall and ceiling.

μm. The transmittances measured for the larger and the smaller samples are 54.6% and 55.63%, respectively (see Figures 43 and 44). Since these are higher than the Fresnel-limited transmittance of 54.55% for GaAs at 1550 nm, both samples will use $\alpha = 0.01$ cm^{-1} for Z-Scan. By accident, the larger piece was used in the Maker Fringe experiment and in the first day of Z-Scan, while the smaller piece was used in the other two days of Z-Scan; the same sample was intended to be used for both. The smaller piece used to be 60% larger, but the rest of it broke off and shattered on

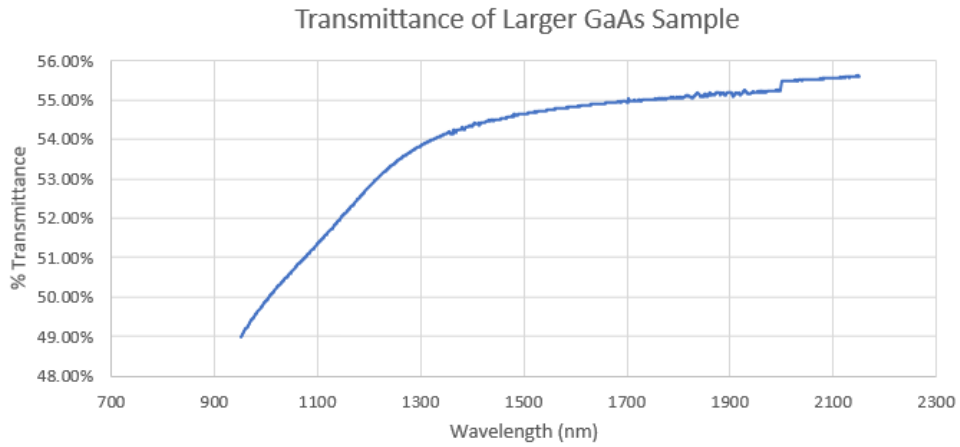

Figure 43: Measured transmittance of larger GaAs sample. The jump at 2000 nm was caused by the spectrophotometer.

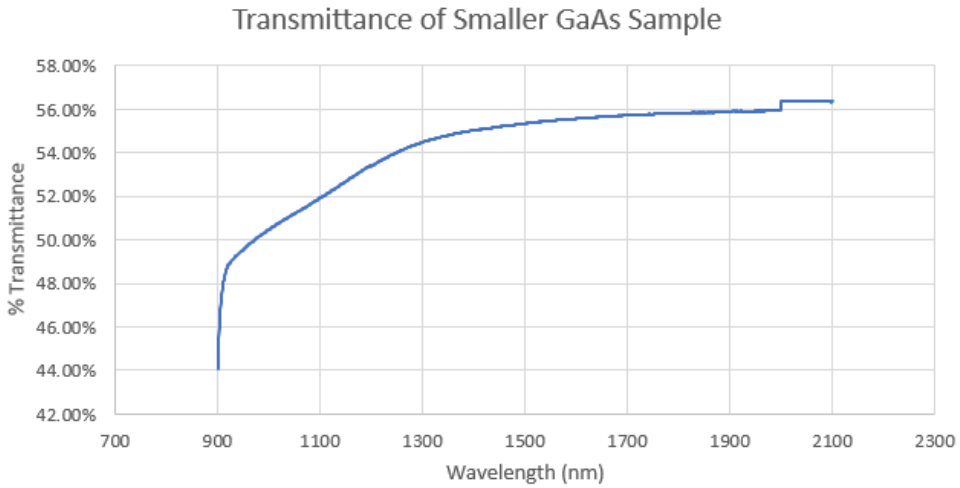

Figure 44: Measured transmittance of smaller GaAs sample. The jump at 2000 nm was caused by the spectrophotometer.

the ground when placing it on the translation stage for the Z-Scan experiment. This occurred before any Z-Scan data, but after taking the Maker Fringe data.

A picture of the second common sample, GaP, is shown in Figure 35 in Section 3.1, and by itself in Figure 45. This piece came from a vendor z-cut GaP wafer left over from prior experiments and appeared to have not been significantly damaged before this research. The 15×10 mm piece was measured to be 499 ± 1 μm

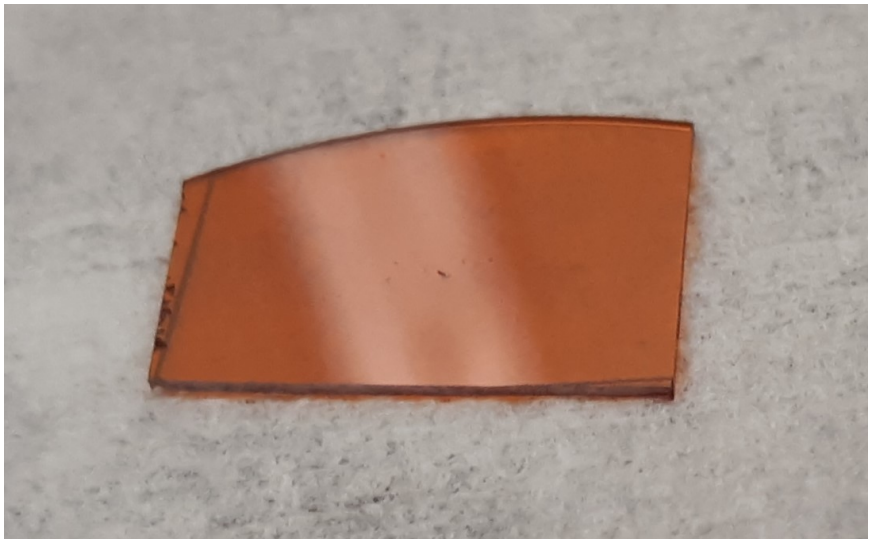

Figure 45: Picture of GaP sample. Note the white streak in the middle is a reflection.

thick. The small damage spots seen on the surface came from the Maker Fringe experiment. The Fresnel-limited transmittance for GaP at 1550 nm is 59.13%, and this sample has a measured transmittance of 57.56% (see Figure 46). Thus, $\alpha = 0.4750$ cm^{-1} for the Z-Scan data analysis.

As the last common sample, ZnSe was used primarily to verify the setup of the Maker Fringe experiment due to its high $\chi^{(2)}$ nonlinearity, and was subsequently put in the Z-Scan experiment. A picture of the ZnSe piece used is shown in Figure 47. This sample is an extra ZnSe piece found in the lab and has been used in experiments prior to this, where many of the damage spots came from, though not all. This piece is likely part of a 6.5 mm radius z-cut wafer based on the SHG output seen from the Maker Fringe experiment, whether vendor-grown or locally-grown is unknown at this point. This piece was measured to be 712 ± 1 μm around the center, where most of the experiments occurred. With the measured transmittance of 68.98% being lower than the Fresnel-limitted transmittance of 69.86% (see Figure 48), the α value used in the Z-Scan experiments is 0.1676 cm^{-1}.

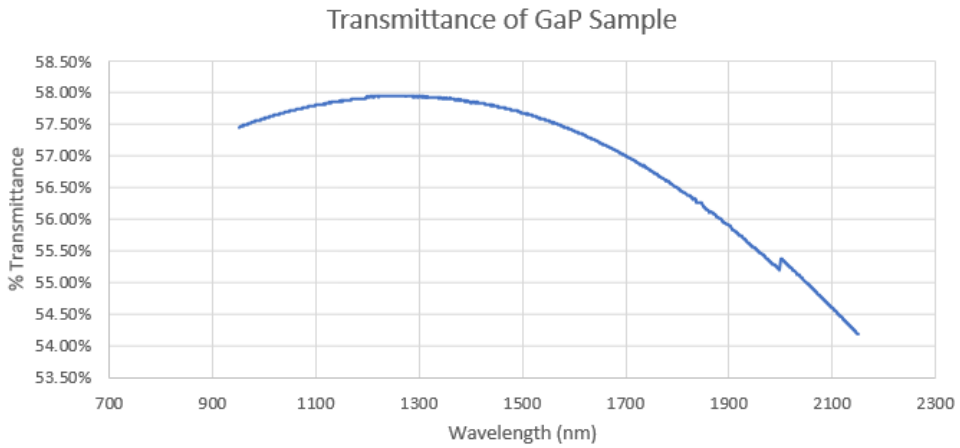

Figure 46: Measured transmittance of GaP sample. The jump at 2000 nm was caused by the spectrophotometer.

Figure 47: Picture of ZnSe sample.

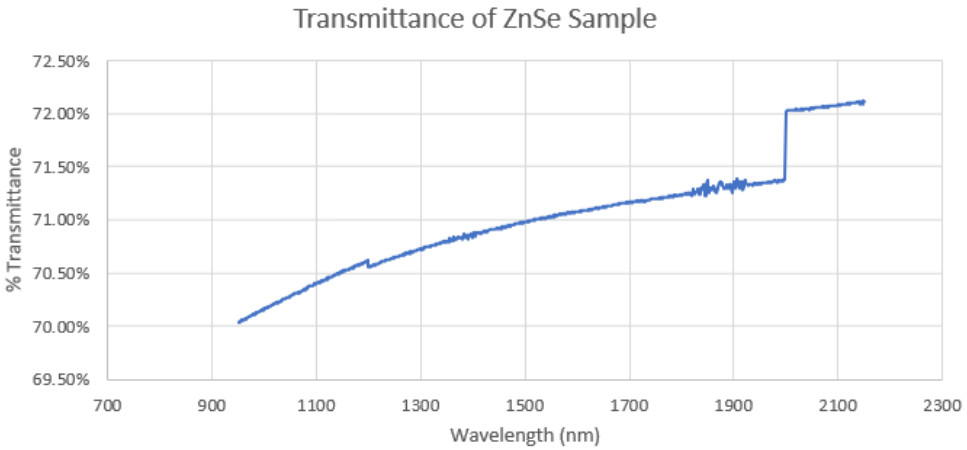

Figure 48: Measured transmittance of ZnSe sample. The jumps at 1200 nm and 2000 nm were caused by the spectrophotometer.

3.3.2 $\mathbf{GaAs_{0.602}P_{0.398}}$

One of the two ternary samples examined in this research is $GaAs_{0.602}P_{0.398}$, shown in Figure 49. The sample's composition is assumed to be uniform with 39.8% phosphorus, and like GaAs and GaP, is a $\bar{4}3m$ crystal [53]. Thus, it has d_{14} as its only d-coefficient. This particular sample was grown at AFRL/RY and polished down to 269 ± 1 μm. The measured transmittance of the sample is shown in Figure 50. At

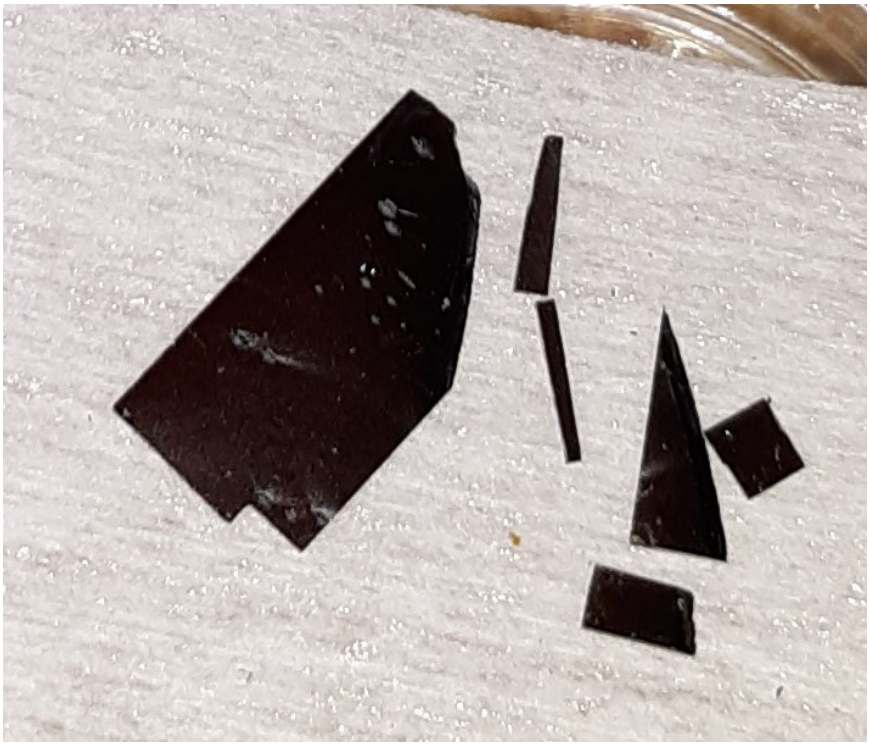

Figure 49: Picture of $GaAs_{0.602}P_{0.398}$ sample. Note the surface defects. This sample was broken when put in the Z-Scan housing unit. The sample appears more black due to lighting; the sample is similar in color to GaAs.

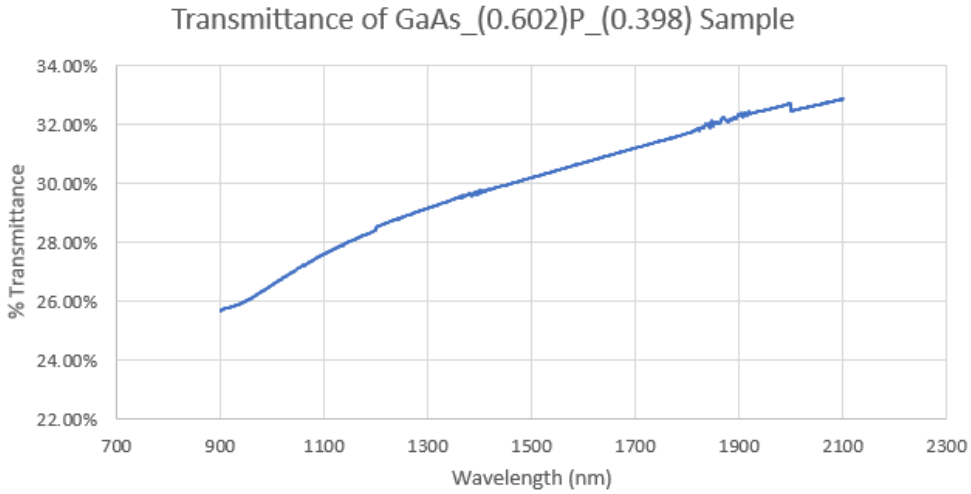

Figure 50: Measured transmittance of $GaAs_{0.602}P_{0.398}$ sample. The jumps at 1200 nm and 2000 nm were caused by the spectrophotometer.

1550 nm, the Fresnel-limited transmittance is 56.30%, and the measured transmittance is 30.45%, which corresponds to an α coefficient of 20.78 cm^{-1}. By looking

at the surface of the sample Figure 49, it is clear that the α coefficient is primarily comprised of loss due to scattering scattering, not linear absorption [15]. This sample does not look polished with all the surface defects, but this was as thin as the polisher could make it without it crumbling [53]. Unfortunately, this means that these defects impacted the data collected from both experiments (see Chapter 4). It used to be 16×6 mm, but is currently 10.5×6 mm after partially breaking while securing it in the Z-Scan sample housing unit. This occurred before any experiments were ran on it, but ultimately did not affect the outcomes of either since the broken pieces also contained a high amount of surface defects.

3.3.3 $\mathbf{GaAs_{0.74}P_{0.26}}$

The other ternary sample examined in this research is $GaAs_{0.74}P_{0.26}$, with both $GaAs_{0.74}P_{0.26}$ samples shown in Figure 51. The samples' composition is assumed to be uniform with 26% phosphorus, and like the other ternary, is a $\overline{4}$3m crystal [53].

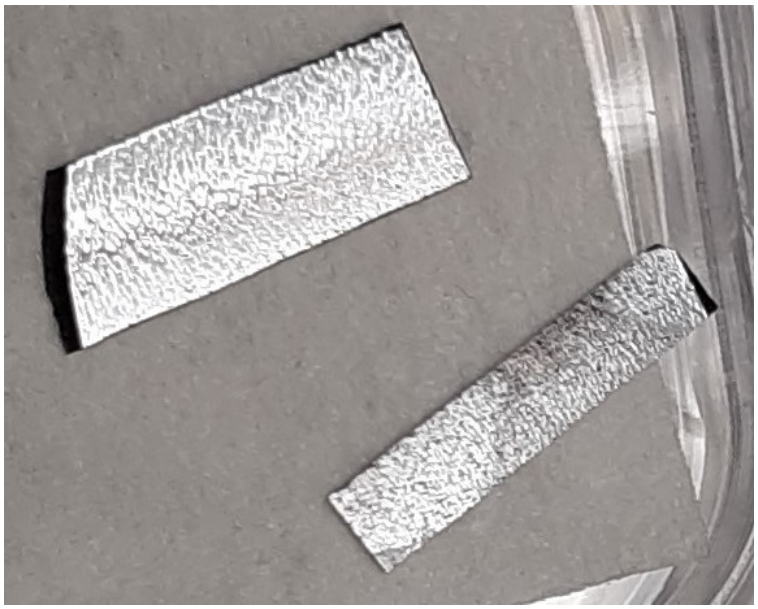

Figure 51: Picture of $GaAs_{0.74}P_{0.26}$ samples. Note the ridges on the surfaces, which do not appear on the other side. The black spots only appear black in this picture due to lighting; they are actually similar in color to GaAs.

Thus, it also only has d_{14} as its only d-coefficient. These particular samples were also grown in AFRL/RY and polished down to 462 ± 1 μm for the 16×6 mm sample and to 391 ± 1 μm for the 16×3 mm sample. Both samples were cleaved from the same wafer, even though their thicknesses are not similar [53]. The measured transmittances of these samples are shown in Figures 52 and 53 . The Fresnel-limited transmittance for these samples at 1550 nm is 55.68%. With the measured transmittances of 41.03%

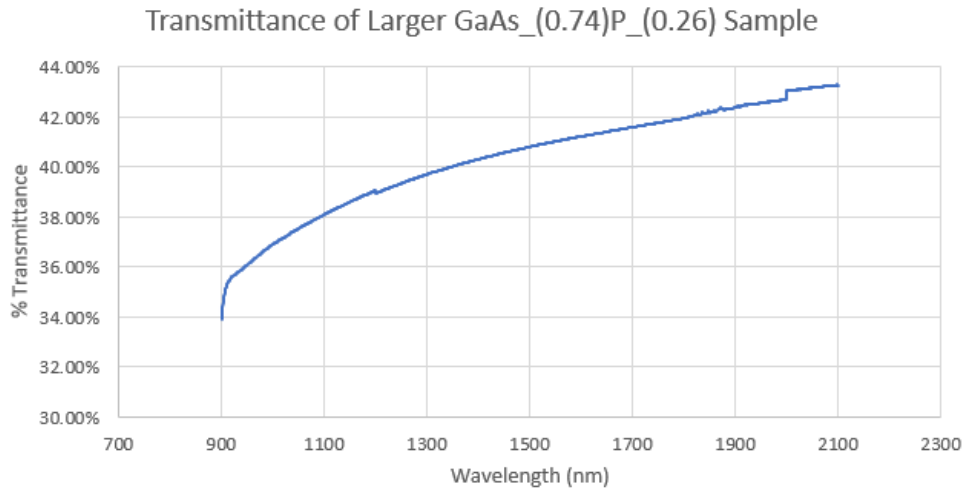

Figure 52: Measured transmittance of larger $GaAs_{0.74}P_{0.26}$ sample. The jumps at 1200 nm and 2000 nm were caused by the spectrophotometer.

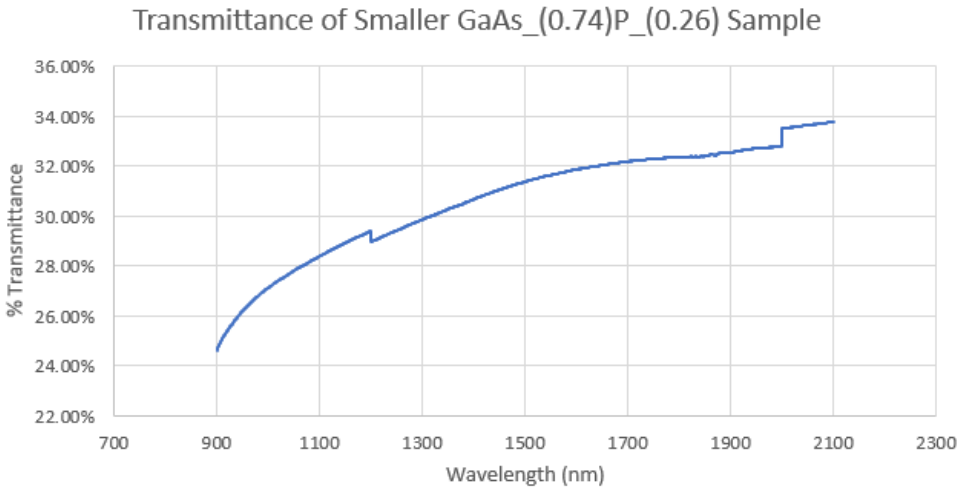

Figure 53: Measured transmittance of smaller $GaAs_{0.74}P_{0.26}$ sample. The jumps at 1200 nm and 2000 nm were caused by the spectrophotometer.

and 31.64% for the larger and the smaller samples respectively, the α coefficients are 5.828 cm^{-1} and 13.05 cm^{-1} respectively. As with the other ternary, these α values are primarily losses due to scattering. The transmittances presented here show how much T can vary with a surface similar to these samples. Looking at Figure 51, the top surface resembles the peel of an orange, but the bottom surfaces are much smoother. Unfortunately, this means that these surfaces impacted the data collected from both experiments (see Chapter 4).

3.3.4 $Sn_2P_2S_6$

The SPS crystal used in this thesis is shown in Figure 54. It was measured to be 1593 ± 1 μm thick, while its other dimensions were 6×3 mm before being damaged. The large flat surface is the (202) plane. The lattice parameters are $a = 0.652$ nm, $b = 0.748$ nm, $c = 1.13$ nm, and the angle $\beta = 124.08°$ [3]. The transmission spectra for this sample is shown in Figures 55 and 56, where the differences in where they overlap come from the differences in the measurement devices. These two figures show the transmittance of SPS to be in agreement with literature [41, 42, 43].

Figure 54: Pictures of $Sn_2P_2S_6$ sample. The left picture is the sample before experimentation, and the right picture was taken after it was damaged while securing it in the Z-Scan housing unit.

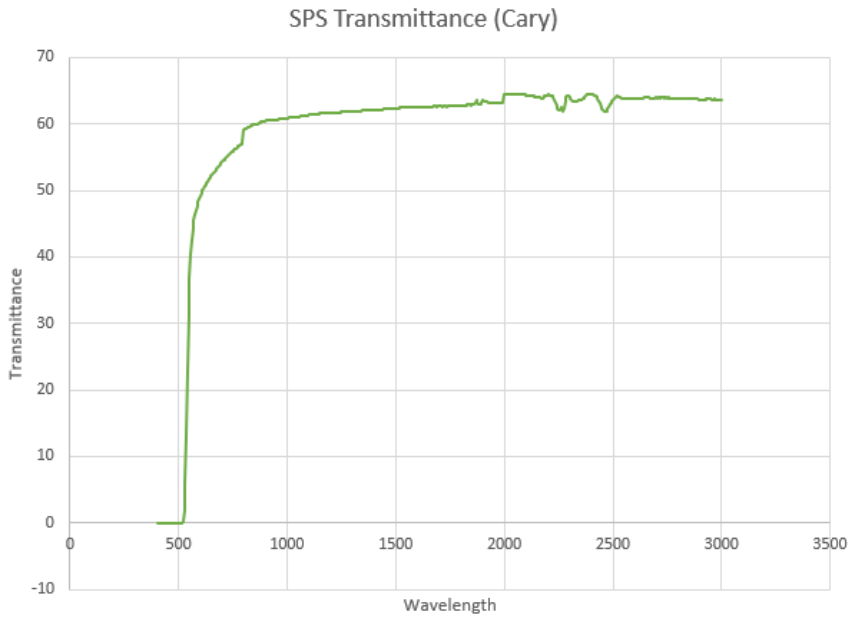

Figure 55: Measured transmittance of $Sn_2P_2S_6$ between 450 nm and 3000 nm. This measurement was taken with a *Varian* Cary 5000 Spectrophotometer. The wavelength is in nm, and the transmittance is in percentage.

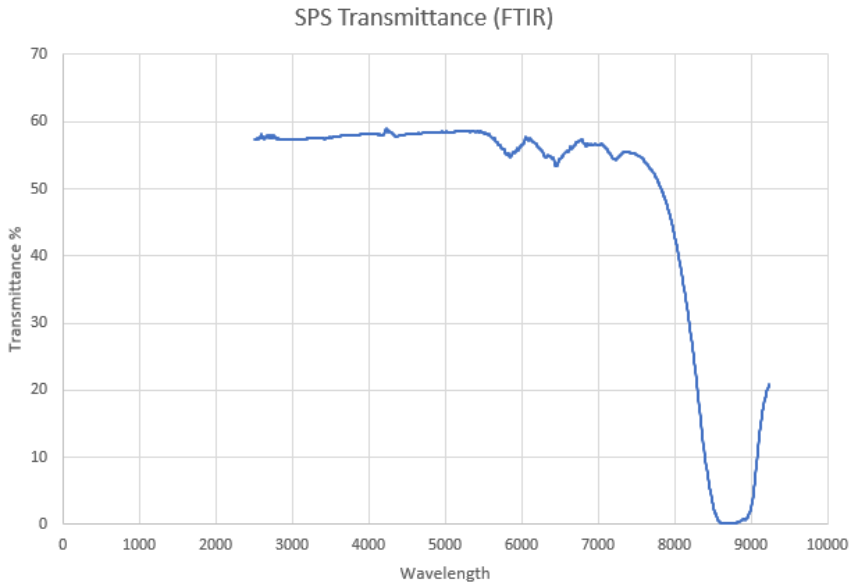

Figure 56: Measured transmittance of $Sn_2P_2S_6$ between 2500 nm and 9250 nm. This measurement was taken with a Fourier Transform infrared (FTIR) spectrophotometer. The wavelength is in nm, and the transmittance is in percentage.

This sample was grown a few years ago at AFRL/RX, and since then has accumulated surface damage to one of is surfaces, possibly affecting any data obtained (see Figure 57). This SPS is also likely not the same crystal orientation throughout, as suggested by the discoloration spot on the one side [3]. Prior to running any experiments on the sample, pieces of it broke off when securing it to the Z-Scan housing unit, happening on the same side as the discoloration spot. As such, no runs were performed near this discoloration spot.

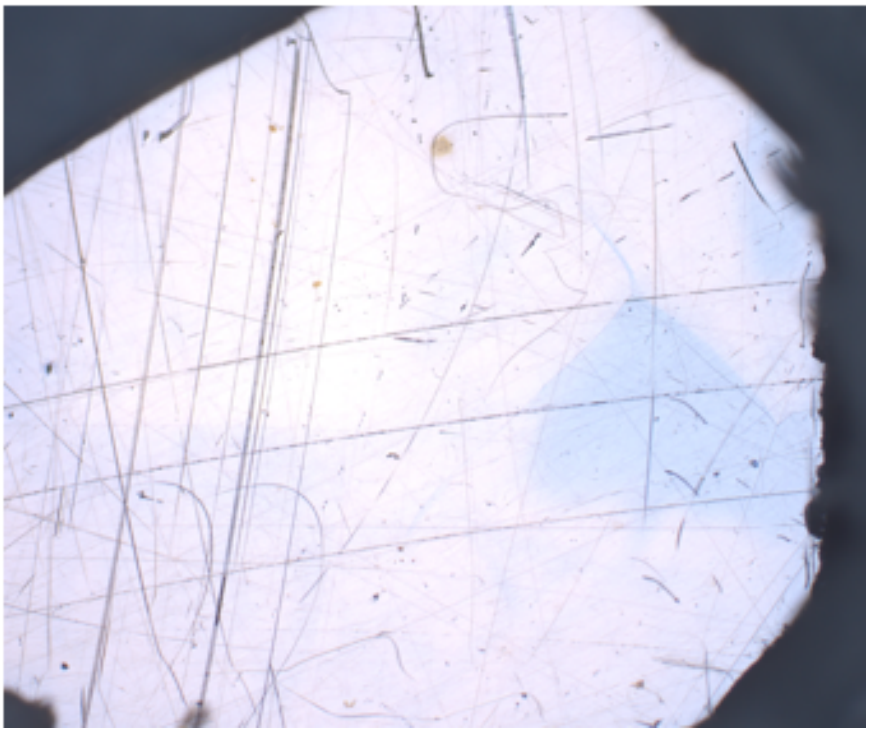

Figure 57: $Sn_2P_2S_6$ sample surface damage and interior defects. Using an optical microscope, many surface defects are seen, some more prominent than others. The blue region on the right is an interior defect and the discoloration spot seen in the left picture in Figure 54.

IV. Results and Analysis

This chapter will cover the data and analysis of the different materials for each experiment.

4.1 Maker Fringe Results

As mentioned in Section 3.1, each sample was placed at the beam waist and was oriented for maximum SHG output, based visually on the peak-to-peak signal on the oscilloscope. Data points were recorded as the average power increased, stopping when either sufficient data points were collected or when the sample was damaged. The data points for the cubic materials were then used to calculate a b_{fit} to be used in the Excel code, presented in detail in Appendix B.2.1. SPS required the Excel code to be modified, elaborated in Appendix B.2.2.

Three sources of uncertainty for these experiments are the sample thickness, the angle of incidence, and the pump power fluctuation. As mentioned in Section 3.3, the profilometer used could accurately measure the thickness to ± 1 μm. Due to the housing units not being identical to each other, an error of $\pm 1^{\circ}$ is used to account for any slight deviations or particles being stuck between the housing unit and the sample. Mentioned in 3.1, the pump power fluctuated during the experiments, with minimum being 3% lower than the maximum. Thus, the pump power can be assumed to fluctuate $\pm 1.5\%$ from its mean output. However, with the output data being averaged over 5000 samples, the overall effect of the pump power fluctuation is assumed to be negligible. Thus, the results and discussion will only address the thickness and the angle of incidence uncertainties.

The rest of this section covers the results obtained for the Maker Fringe experiment, starting with ZnSe as that was used to verify the setup. The ternaries and

SPS are presented next. GaAs presented last, to help highlight a shortcoming with this method of analysis. The GaP Maker Fringe run is presented in Appendix D.4.1.

4.1.1 ZnSe – Experimental Setup Verification

Figure 58 shows the fitting curve for determining b_{fit}, which produces a b_{fit} of 6956.1 nJ/(GW/cm^2)^2. With a thickness of 712 μm and an L_c of 13.35 μm, this sample is 53.45 coherence lengths thick, meaning that the thickness should not interfere with d_{eff} calculations, which will be verified below. Entering this b_{fit} value and an incident angle of 9.25° into the code detailed in Appendix B.2.1, the resulting d_{eff} value is 148.06 pm/V. Since the sample was rotated about its surface normal, the SHG output was maximized at this given incident angle. From the method provided in Appendix A, d_{14} is calculated by dividing d_{eff} by $\sqrt{3}$, which results in $d_{14} = 85.48$ pm/V. This is approximately 2.44 times as high as the expected d_{14} value of 35 pm/V based on using Miller's Rule, mentioned in Section 2.3.4.

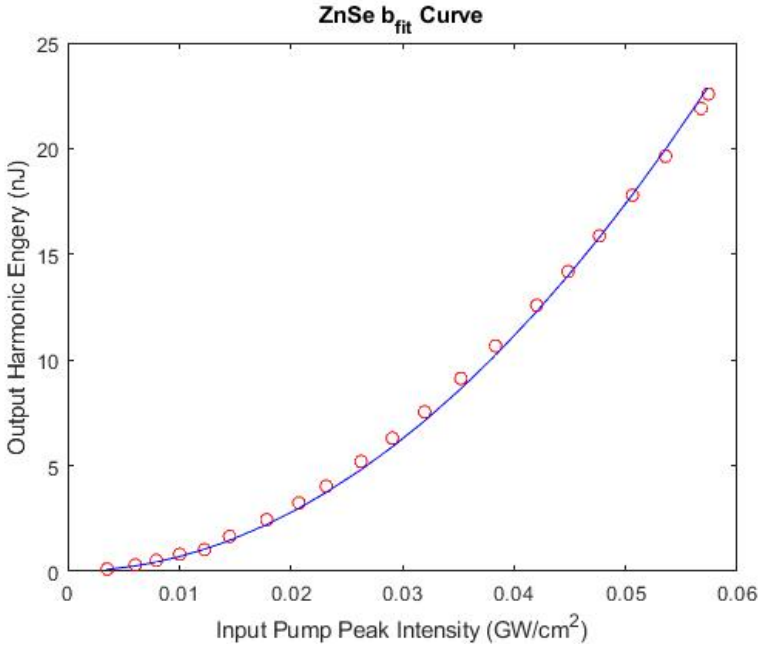

Figure 58: Plot of b_{fit} curve for ZnSe. The red circles are the data points collected, and the blue line is the fitting curve from Equation 53.

Not knowing where a factor of 2.44 could have originated, the d_{eff} calculation code was reexamined. The lab setup was reexamined for potential information missed. Last to be examined was the conversion equations used to obtain E_{SHG} and I_{in}. After checking all of these areas, the factor of 2.44 is still present, which is puzzling since the code produces more accurate results when used by the ones who wrote it. This is an unusual scaling factor to be off by, considering the values used in all the equations. Since the Miller's Rule was used to calculate the expected d_{14} value of 35 pm/V, it is possible that the expected value of d_{14} is incorrect due to the approximation involved when using Miller's Rule [8]. If the expected d_{14} was 15% larger (40 pm/V), then d_{eff} would be larger by a factor of 2.14; if 15% smaller (30 pm/V), d_{eff} would be larger by a factor of $2\sqrt{2}$. Since different powers of 2 are used in many equations, the latter scenario is more likely. As such, the calculated d_{eff} values obtained will be divided by $2\sqrt{2}$ for all the samples before calculating the individual d-coefficients.

Dividing ZnSe's previously calculated d_{14} by $2\sqrt{2}$ results in a d_{14} of 30.22 pm/V, about 15% lower than the 35 pm/V from Miller's Rule. Now to examine the uncertainty values, starting with thickness. With an uncertainty of ± 1 μm, Figure 59 shows the d_{14} values for thicknesses of 711 μm to 713 μm. This plot was made by plotting the output of Equation 57 divided by $\sqrt{3} \times 2\sqrt{2}$ while the thickness was varied at set intervals between 711 μm to 713 μm. The minimum value is 27.65 pm/V while the maximum value is 33.84 pm/V, corresponding to errors of 8.5% and 12%, respectively. Figure 60 plots the d_{14} values obtained by changing the angle of incidence by $\pm 1^{\circ}$. The minimum value is 29.33 pm/V while the maximum is 31.33 pm/V, corresponding to errors of 3% and 3.8%, respectively.

Applying the maximum errors from the thickness and the angle of incidence to the calculated d_{14} of 30.38 pm/V, the maximum and minimum values for d_{14} would be 34.99 pm/V and 26.74 pm/V, being errors of 16.2% and 11.3%, respectively. The

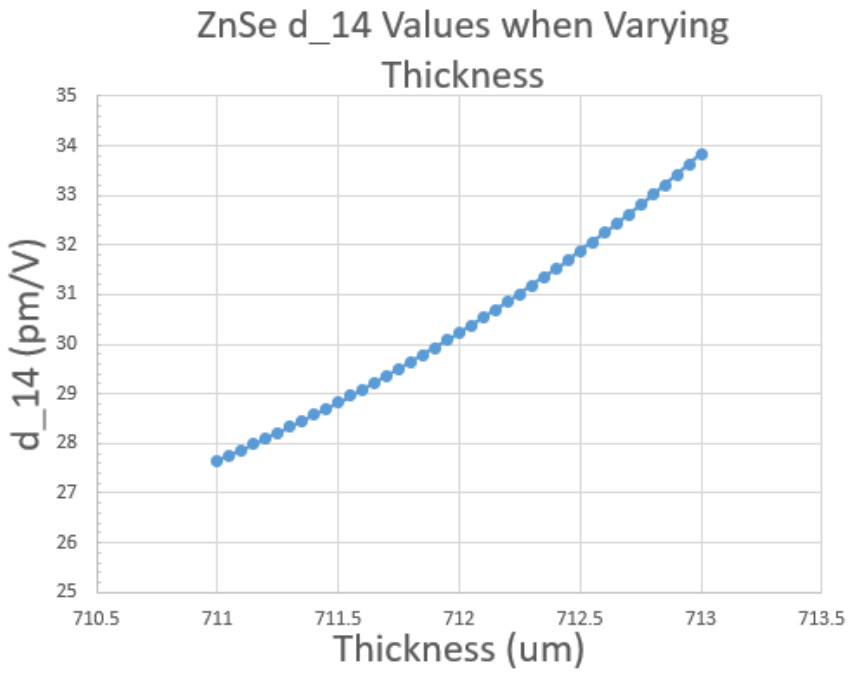

Figure 59: Plot of d_{14} values for ZnSe based on thickness. The thickness is varied between ± 1 μm, substituted into Equation 57, divided by $\sqrt{3} \times 2\sqrt{2}$, and plotted.

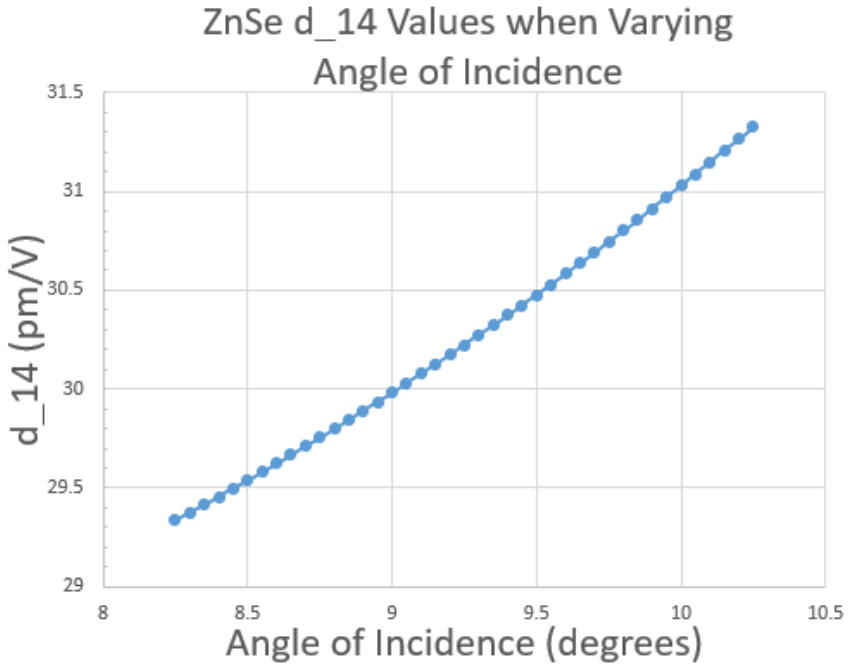

Figure 60: Plot of d_{14} values for ZnSe based on the angle of incidence uncertainty. The angle of incidence is varied between $\pm 1^{\circ}$, substituted into Equation 57, divided by $\sqrt{3} \times 2\sqrt{2}$, and plotted.

original expected d_{14} value of 35 pm/V is at the edge of this error for new d_{14} value of 30.22 pm/V. Therefore, when accounting for the $2\sqrt{2}$ scaling factor, the Maker Fringe setup is verified to provide accurate values.

4.1.2 $\mathbf{GaAs_{0.602}P_{0.398}}$

Unfortunately, there are no Maker Fringe data for $GaAs_{0.602}P_{0.398}$. The sample was placed in the housing unit in multiple different orientations, but every orientation attempted resulted in the sample being damaged by the pump before any data points were able to be taken. While the SPS crystal and the other ternary damaged with a fluence of about 5000 J/m^2 per pulse, $GaAs_{0.602}P_{0.398}$ damaged with as little as 2500 J/m^2 of fluence per pulse. This was evident by the SHG signal appearing upon a new orientation then decreasing to zero while nothing changed, and by the rings seen in Figure 61. The damage likely occurred due to the poor surface quality on

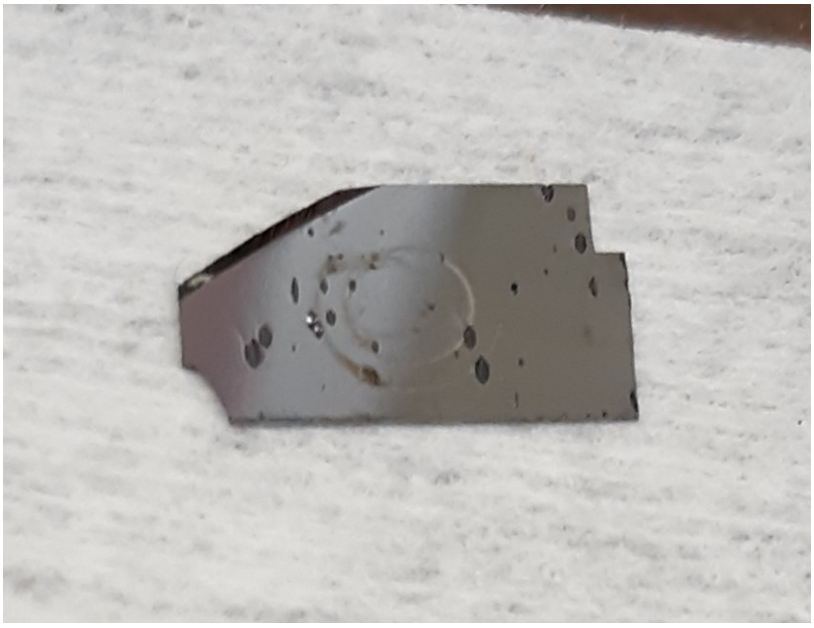

Figure 61: Picture of damaged $GaAs_{0.602}P_{0.398}$ sample. Note the two circular damage patterns, which occurred while irradiated with 300 mW (outer) and 150 mW (inner) of average power. These rings appear on both sides of the sample, even though the pump was only incident on one side of the sample.

both sides of the sample. With no data points recorded, no conclusions can be made about its d_{14} coefficient, other than it is not zero.

4.1.3 $GaAs_{0.74}P_{0.26}$

Two data sets were obtained for the larger sample. The data were collected on separate days. The same setup was used for both data collections, but the beam was incident either on a more sensitive location for the second day or on the damage spot caused by the first day, which ended in the surface being damaged at a lower average power. As a result, the b_{fit} value for the second day is 16% smaller than from the first day.

Figure 62 shows the plot of the b_{fit} fitting function. Only six data points were obtained before the sample was damaged, but since the other data set produced a lower b_{fit}, the fit calculated here will be used. The b_{fit} value obtained from the first data set is 23.0867 nJ/(GW/cm^2)^2. Using Vegard's Law for the refractive indices and

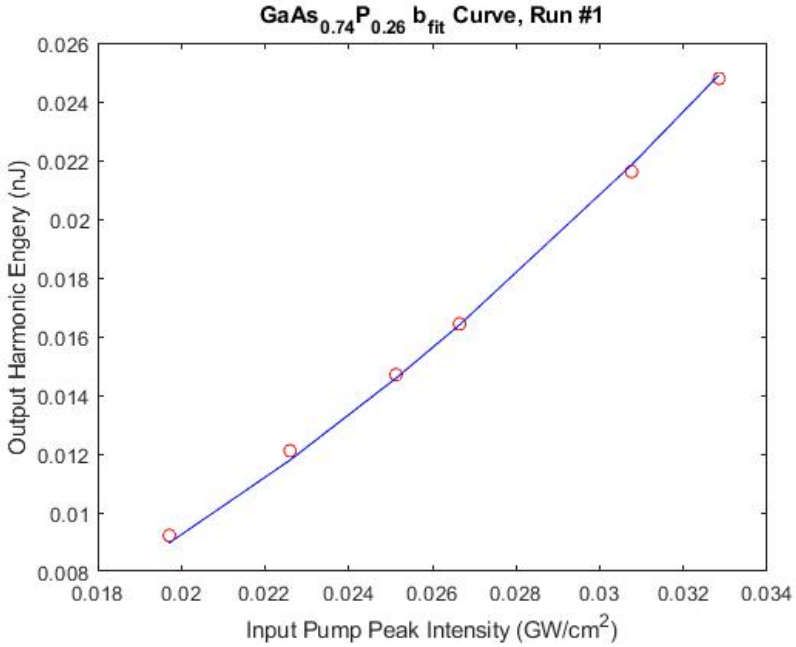

Figure 62: Plot of b_{fit} curve for the first data set for $GaAs_{0.74}P_{0.26}$. The red circles are the data points collected, and the blue line is the fitting curve from Equation 53.

the incident angle of 14°, dividing d_{eff} by $\sqrt{3} \times 2\sqrt{2}$ results in a d_{14} of 8.371 pm/V, which is 15.8% of GaP's expected d_{14}. With a thickness of 462 μm and an estimated L_c of 4.1 μm, this sample is 113.1 coherence lengths thick, so changing its thickness by ± 1 μm will not significantly affect d_{14}. This extremely low d_{14} value is likely caused by the rough surface scattering much of the pump, allowing only a small fraction to transmit without changing propagation direction. Another possibility would be that its refractive indices are different than calculated with Vegard's Law, changing L_c such that the thickness would be closer to an even number of L_c's thick. Therefore, a d_{14} value cannot be obtained for this ternary sample.

4.1.4 $Sn_2P_2S_6$

Figure 63 shows the b_{fit} curve, calculating b_{fit} to be 49.2399 nJ/(GW/cm^2)^2. A second run was accomplished with the same orientation as the first, resulting in a b_{fit} of 49.3914 nJ/(GW/cm^2)^2. For the following calculations, the average of the two

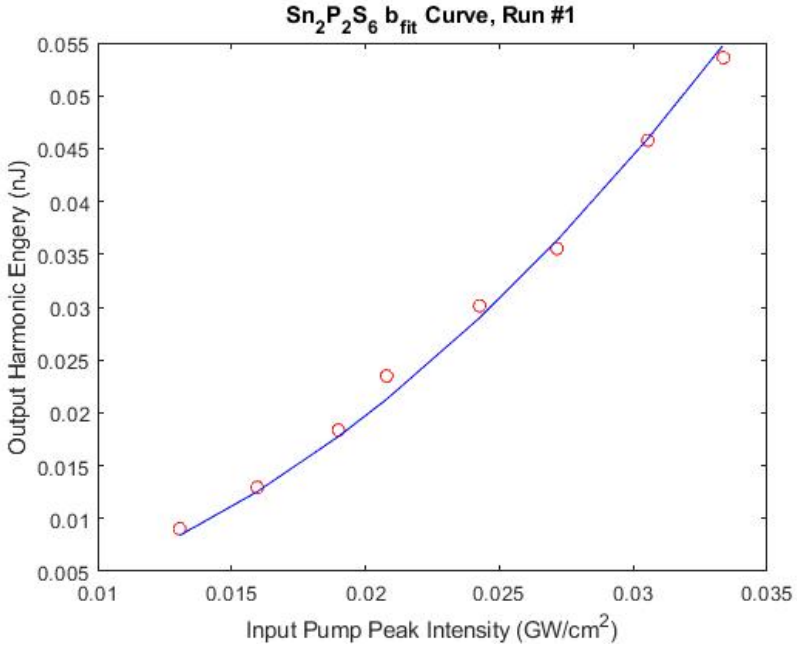

Figure 63: Plot of b_{fit} curve for SPS. The red circles are the data points collected, and the blue line is the fitting curve from Equation 53.

b_{fit} values will be used. Since SPS is birefringent and can phasematch, modifications to the code are made and documented in Appendix B.2.2. With these modifications, d_{eff} is calculated to be 0.06488 pm/V, which is then scaled by $2\sqrt{2}$ to be 0.02294 pm/V. When using in the predetermined d-coefficients from Equation 76 to determine d_{eff} from Equation 34, this d_{eff} is about two orders of magnitude higher than what was obtained, even when using the smallest possible values for the d-coefficients. Two factors are likely the cause of the discrepancy between the lab results and theoretical calculations. The SPS sample has been damaged over the years since its fabrication (see Figure 57) and has not been polished before testing, causing the pump to be scattered by the damaged area. The sample also may not have been aligned properly for phasematching, meaning $\Delta k \neq 0$ which in turn leads to less frequency conversion. Without a realistic d_{eff}, the individual d-coefficients for SPS were not calculated.

4.1.5 GaAs

Figure 64 shows the fitting curve for determining b_{fit}, which produces a b_{fit} of 314.4253 nJ/(GW/cm^2)^2. Using $n_p = 3.334201$ and $n_s = 3.480402$ in Equation 44, the coherence length for this SHG process is 3.36 μm. With a thickness of 347 μm, this sample is 97.6 coherence lengths thick. With such a small L_c, the thickness interferes with d_{eff} calculations, as shown below. Entering this b_{fit} value and an incident angle of 9° into the d_{eff} calculation code, the resulting d_{eff} value is 314.92 pm/V. Dividing 313.32 pm/V by $\sqrt{3} \times 2\sqrt{2}$ results in a corrected d_{14} value of 63.96 pm/V. With the expected value for d_{14} being 107.7 pm/V, this value is about 40.6% too low.

This discrepancy can be rectified by looking at the errors. The errors based on the angle of incidence are 4.6% and 5.9%, which is not enough to correct the d_{14} value. However, Figure 65 shows the d_{14} values when the thickness is changed by

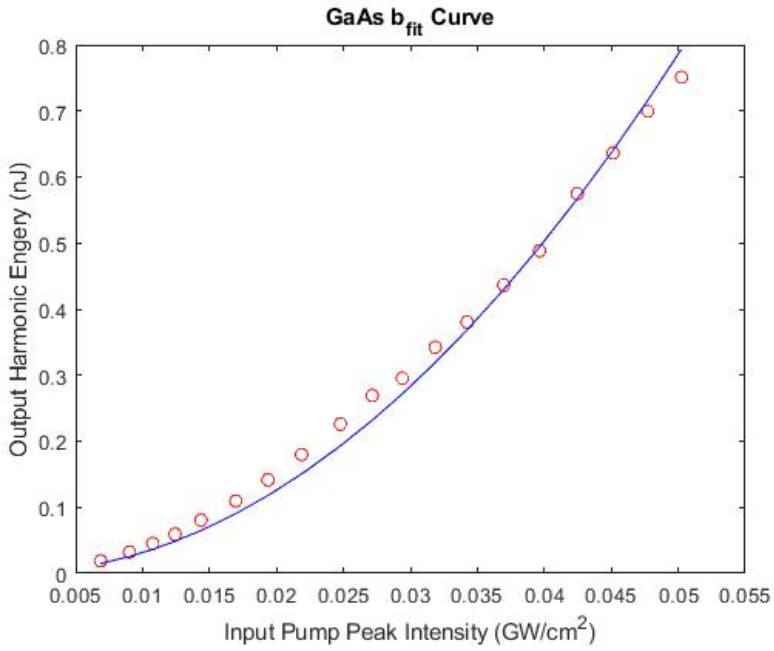

Figure 64: Plot of b_{fit} curve for GaAs. The red circles are the data points collected, and the blue line is the fitting curve from Equation 53.

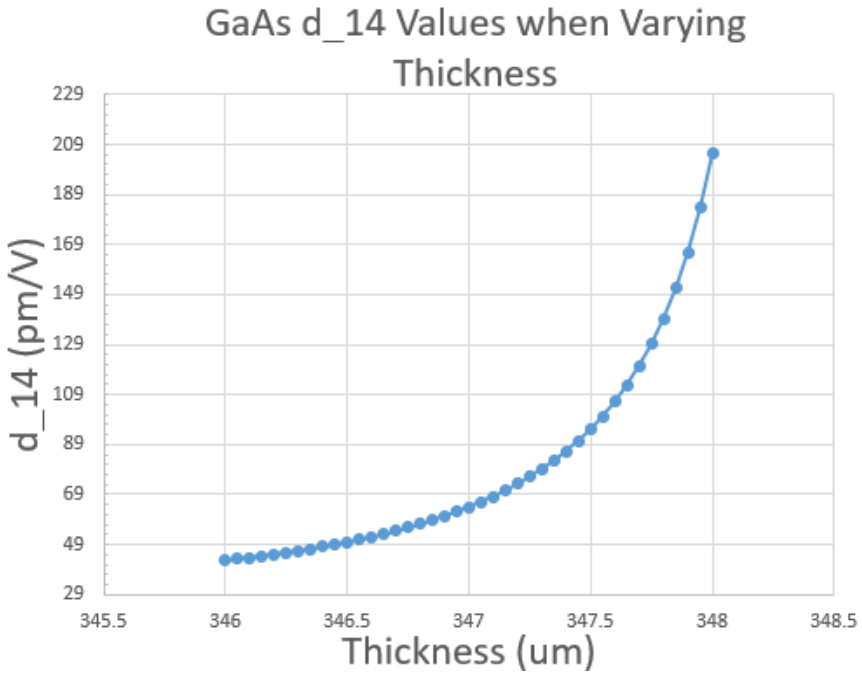

Figure 65: Plot of d_{14} values for GaAs based on thickness. The thickness is varied between ± 1 μm, substituted into Equation 57, divided by $\sqrt{3} \times 2\sqrt{2}$, and plotted.

± 1 μm. A d_{14} of 107.7 pm/V corresponds to an L of about 347.6 μm, well within the margin of error from the profilometer. By observation, the error is substantial based on thickness, since d_{14} starts to rapidly increase by as the thickness increases to 348 μm. This graph highlights one of the limiting factors of this method: the sample being close to an even number of coherence lengths thick. With a more accurate measurement of L, this error could be reduced significantly.

4.1.6 Maker Fringe Summary

Table 7 summarizes the results obtained from the Maker Fringe experiment.

Table 7: d_{eff} and d_{14} Values Obtained from the Maker Fringe Experiment

	ZnSe	GaAs	GaP[b]	$GaAs_{0.602}P_{0.398}$	$GaAs_{0.74}P_{0.26}$	$Sn_2P_2S_6$
d^c_{eff} pm/V	53.35	110.8	133.9	X[d]	14.50	0.02294[e]
d_{14} pm/V	30.22	63.96	77.30	X[d]	8.371[e]	N/A[f]
Miller's d_{14} pm/V	35[g]	107.7[g]	53.1[g]	N/A[h]	N/A[h]	N/A[f]

a: Pump wavelength at 2090 nm.
b: Presented in Appendix D.4.1.
c: $2\sqrt{2}$ scaling factor applied.
d: Sample damaged before data collected.
e: Value unreliable; much lower than it should be.
f: Does not have d_{14}. Other d-coefficients not calculated.
g: Within uncertainty errors from calculated d_{14}.
h: Does not have one, due to not being characterized at other wavelengths.

4.2 Z-Scan Results

The pump for Z-Scan experiment was set to 1550 nm, allowing the comparison of the β values between GaAs and the $GaAs_xP_{1-x}$ ternaries. As mentioned in Chapter 3.2, the laser system used in the Z-Scan experiment was not stable for most

of the runs, initially seeing frequent power drops upwards of 20% and eventually up to 60% by the end of testing. Except for two GaAs runs completed prior to the pump instability issue, every run was conducted with this issue. Due to time constraints, the OPA system could not be realigned to make the laser stable, affecting all the data runs. Since the properties determined here are intensity based, the pump instability greatly affects the ability to determine them accurately.

With the setup moved the day after the last run was completed, some runs were never attempted, namely the CA runs on the ternary samples and SPS. Another Z-Scan setup was not available in time for any follow-up runs, so the few runs collected are all that can be analyzed. Also due to time constraints, the focus point z_0 and the size of the beam waist w_0 were not measured, making them fit parameters along with β and n_2. In general, the translation stage was not moved in between runs, but it will be noted whenever the stage was moved. The intent was to use the GaAs sample to determine z_0 and w_0 and use the determined values for the other samples. This is attempted, but not usable, as will be explained in Section 4.2.1. For the runs that were determined to be unable to have a proper fit, a default z_0 is chosen and the data are shown without a fit.

Towards the end of testing, it was observed that the z-translation stage was not perfectly aligned with the propagation of the beam. This misalignment negatively impacted the samples with poor surface qualities (the ternaries and SPS). For well-polished samples, the misalignment is not an issue, but for poorer quality samples like the ternaries, the misalignment significantly affects the data. Since the sample is also moving in the x- or y-direction (or both) as it is moving down the z-axis, the place the beam enters the sample moves. As the sample moves, the beam encounters new defects or damaged regions, or it no longer irradiates the same defects or damaged regions it previously did. When this scenario happens, the T_N graph will deviate from

the expected shape for the OA and the CA runs, an example being the asymmetric nature of the OA $GaAs_{0.602}P_{0.398}$ runs shown in Section 4.2.3.

The rest of this section covers the results obtained for the Z-Scan experiment. The GaAs runs completed before the pump instability are presented first, as they validate the performance of the Z-Scan setup when laser is stable. The OA ZnSe and GaP runs are presented next, as these runs will be used in the analysis of the OA SPS runs, presented afterwards. The last part of this section will cover the OA $GaAs_xP_{1-x}$ runs and explain why the data collected is unusable. Additional runs are located in Appendix D.

4.2.1 Z-Scan Setup Verification

Before any pump instability issues occurred, two OA GaAs runs were conducted on the larger GaAs sample, shown in Figures 66 and 67. Both of these fits use the same w_0 value of 38.90 μm, but use z_0 values of 19.07 mm and 19.61 mm, respectively, due

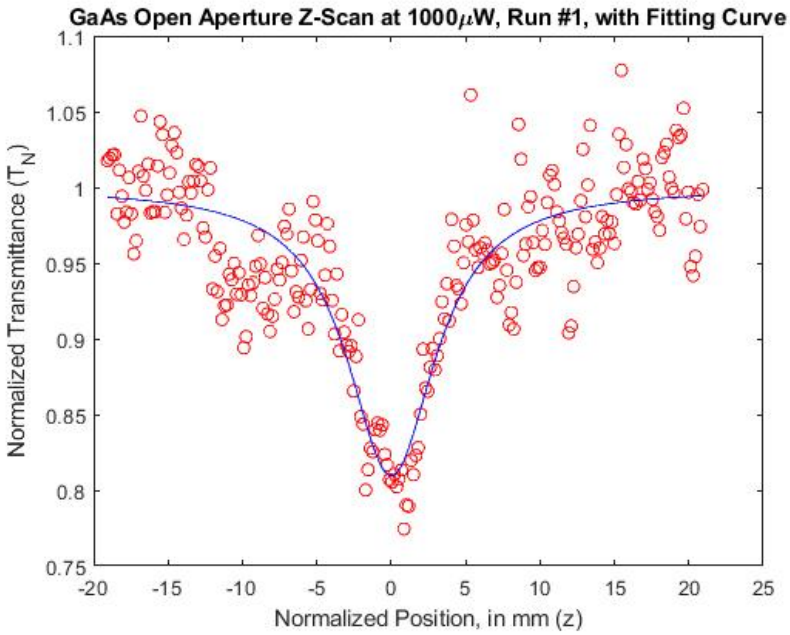

Figure 66: GaAs open aperture Z-Scan Run #1 at 1000 μW. The red circles are the collected data, and the blue line is the fit Equation 71.

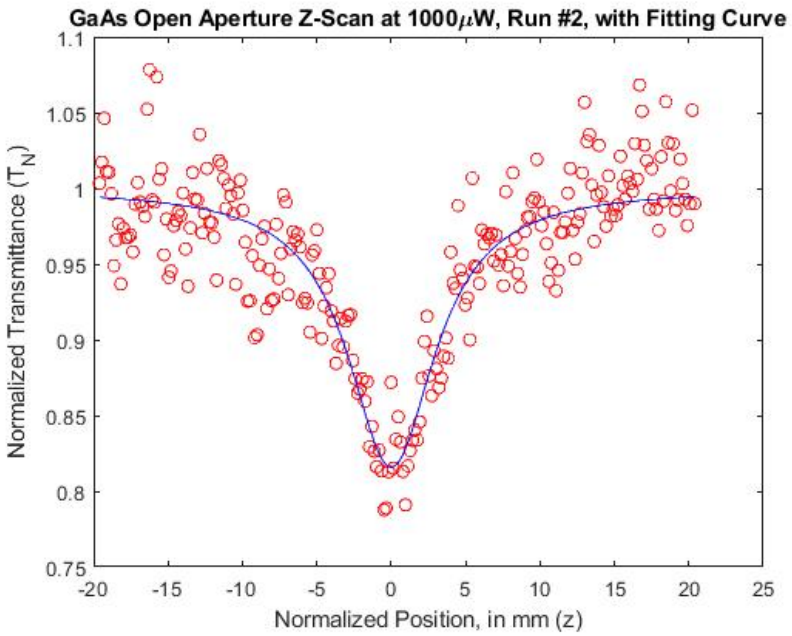

Figure 67: GaAs open aperture Z-Scan Run #2 at 1000 μW. The red circles are the collected data, and the blue line is the fit Equation 71.

to the translation stage being moved in between the runs. The pump itself was not altered between the runs, hence the same beam waist value. The β values obtained from the fits are 12.28 cm/GW and 11.73 cm/GW, respectively. These values are close to the theoretical β values for GaAs at 1550 nm, shown in Figure 68, which is Figure 2 modified to showcase the theoretical β value at 1550 nm [5]. Thus, this Z-Scan setup is valid, when the pump is stable.

4.2.2 Open Aperture ZnSe, GaP, and SPS

This subsection covers ZnSe and GaP which have been recorded in literature to not have an appreciable β value at 1550 nm, and SPS whose data plots are similar to the plots for ZnSe and GaP.

4.2.2.1 Open Aperture ZnSe and GaP

Figures 69 and 70 show the plots for the two OA runs done for ZnSe, accomplished

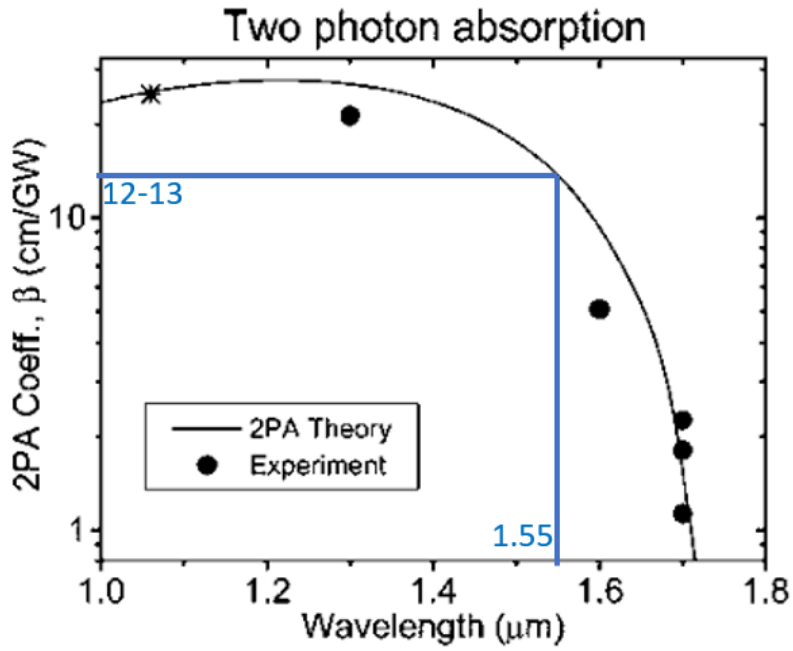

Figure 68: Nonlinear absorption in GaAs at 1550 nm. The theoretical two photon absorption value β at 1550 nm is between 12 and 13 cm/GW. *This figure is modified from [5].*

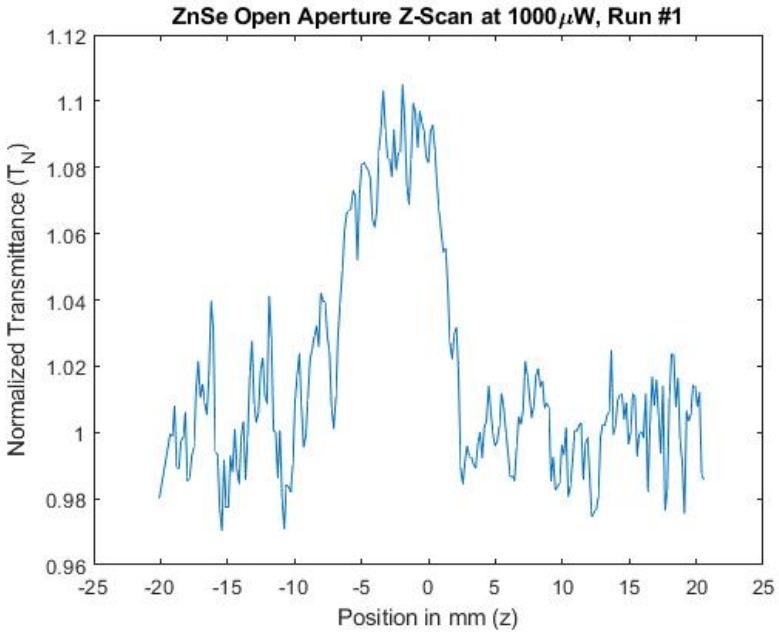

Figure 69: ZnSe open aperture Z-Scan Run #1. The blue line is the normalized collected data.

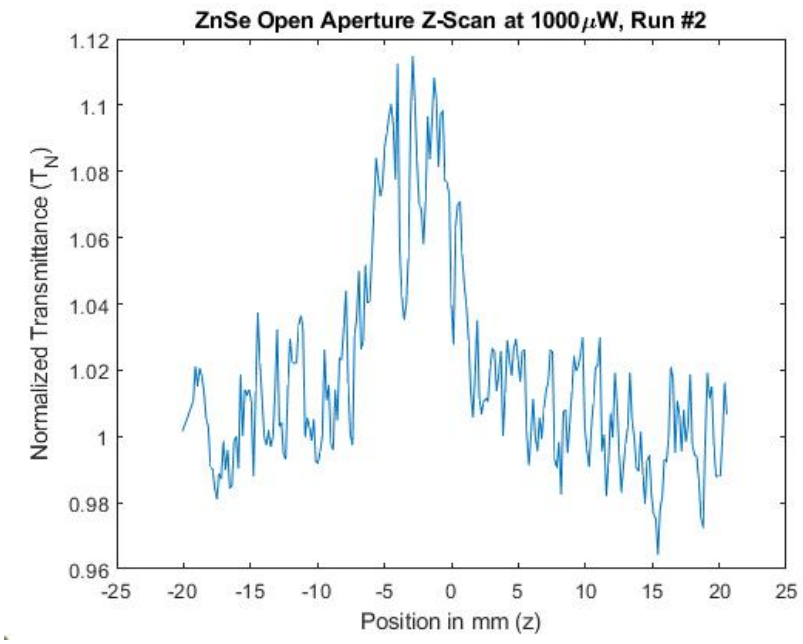

Figure 70: ZnSe open aperture Z-Scan Run #2. The blue line is the normalized collected data.

after the OA GaAs runs, which showed that the pump instability affected the curve of the graph. The OA ZnSe runs will be examined as is because there is a hill where the dip should be. A flat graph would indicate that β is negligible, whereas the hill indicates a negative β value (negative 2PA). Since negative two photon absorption does not make sense, these graphs were not fitted. The hills are possibly due to some surface defect on the ZnSe sample or due to the pump instability since the hills occur near the focus. Even though they are noisy, these graphs then indicate that β is likely negligible or within the noise for ZnSe at 1550 nm, in agreement with what was presented in Chapter 2.3.4 [50].

As the last sample tested, only two OA runs of GaP were conducted, one at 200 μW (Figure 71) and one at 1000 μW (Fiugre 72). During these runs, the pump continued to increase in instability, frequently dropping in power by upwards of 60%. The 200 μW run is relatively flat, with the $\pm$8% fluctuations in T_N being caused by the unstable pump. The 1000 μW run resembles the ZnSe OA runs

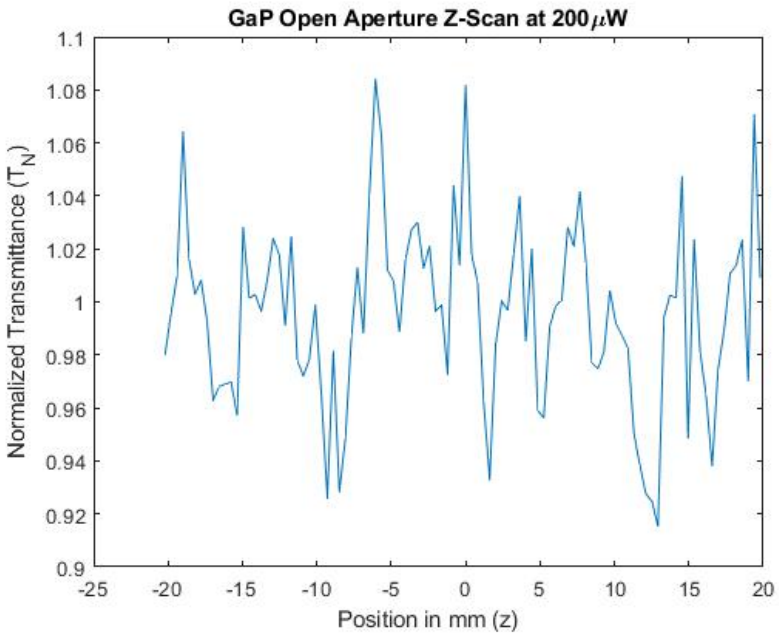

Figure 71: GaP open aperture Z-Scan Run at 200 μW. The blue line is the normalized collected data.

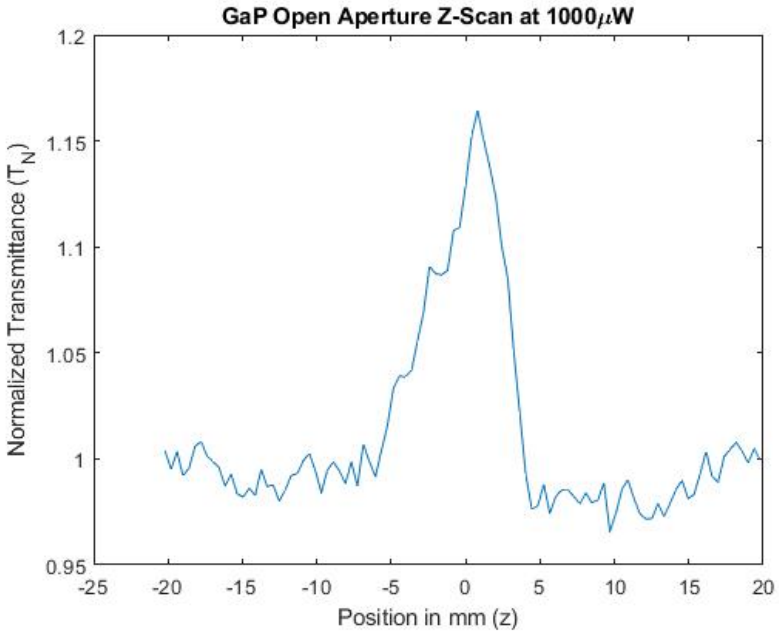

Figure 72: GaP open aperture Z-Scan run at 1000 μW. The blue line is the normalized collected data.

(Figures 69 and 70), with the higher T_N maximum for GaP possibly being attributed to the greater pump instability . Like with ZnSe, Figures 71 and 72 show that GaP likely has a negligible β value at 1550 nm, in agreement with [38].

4.2.2.2 Open Aperture $Sn_2P_2S_6$

Seven OA SPS runs were recorded, four at 1 mW and three at 5 mW. Figure 73 is Run #4 completed at 1 mW, while Figure 74 is Run #3 of the 5 mW runs. The other runs produced similar graphs at the same intensities, and are presented in Appendix D4.2. The 1 mW runs are noisy and asymmetrical, but are relatively flat with hills around z_0 rather than valleys. These are a result of the pump instability, the defects on the sample, and the translation stage not being perfectly aligned. The 5 mW runs are very similar to the 1 mW runs, except they all have one or two data points substantially lower than the rest, all occurring at the same z value. While this may indicate that SPS has an appreciable β value, T_N at that

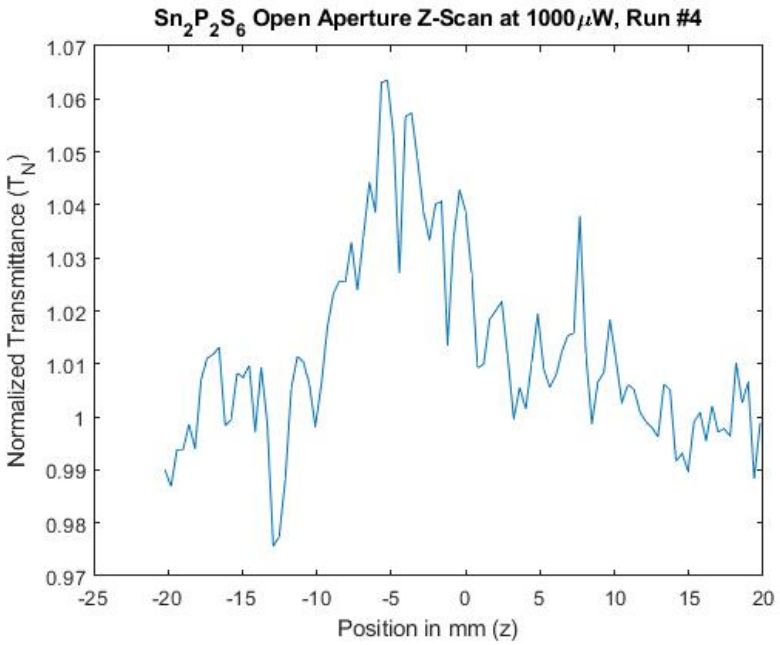

Figure 73: $Sn_2P_2S_6$ open aperture Z-Scan Run #4 at 1000 μW. The blue line is the normalized collected data.

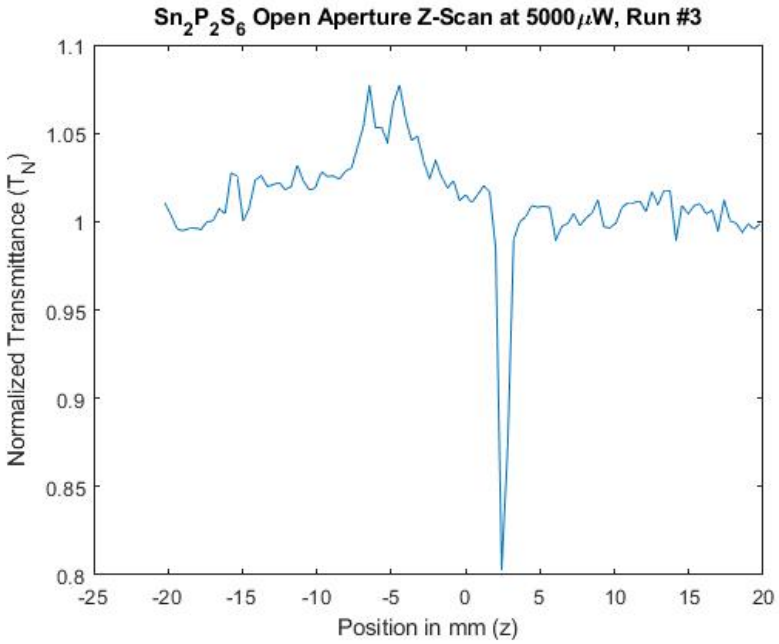

Figure 74: $Sn_2P_2S_6$ open aperture Z-Scan Run #3 at 5000 μW. The blue line is the normalized collected data. The minimum point resulted from interference on the sample surface.

point decreases across the three runs and T_N does not slowly approach the low point for the z values around it as it should if β were appreciable. Both of these observations indicated that something else was affecting the data, so the sample was slightly moved for a follow-up run, for which this low point did not occur (this particular run was accidentally not saved). Thus, that low point was likely the result of some interference on or in the SPS crystal. Since the SPS OA runs have features similar to the ZnSe and GaP OA runs, SPS does not appear to have an appreciable β value at 1550 nm, and if it does, the noise may be preventing its detection.

4.2.3 $GaAs_xP_{1-x}$ Ternaries

This final section encompasses OA runs performed on the ternaries. Unlike the runs in the first two sections, these runs were heavily affected by the pump instability and by the sample quality. The runs conducted in the Section 4.2.2 utilized the same

unstable pump, but since their β values were negligible or obscured by the noise, conclusions can be made from their data. The ternaries are expected to have β values at 1550 nm observable with an OA run. However, as will be discussed below, the data obtained could not be analyzed to determine β for either ternary.

Figures 75 and 76 show the only two runs saved for the $GaAs_{0.602}P_{0.398}$ sample. These were not the only two runs performed, but the only two saved since every other run performed on this sample resulted in similar or more asymmetric graphs. The sample was moved between runs to try to find an area on both sides of it where there would not be any defect interference, which never occurred. Given the nature of the OA runs, the graphs should be symmetrical since the beam is passing through the same area on the sample, but these graph are not close to being symmetrical. The asymmetrical plots indicate that the translation stage was not perfectly aligned with the propagation of the beam, as mentioned in Section 4.2. It was during these runs that the misalignment was first noticed. Since these graphs do not resemble an OA

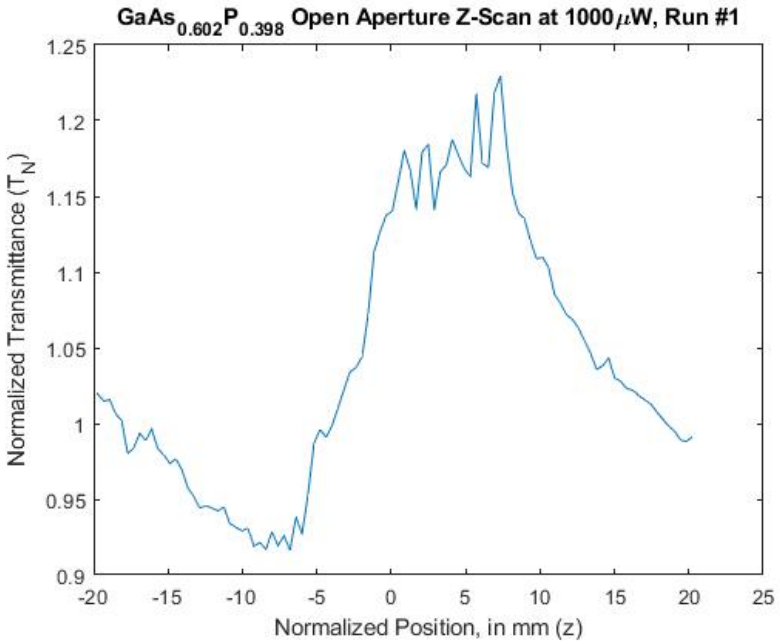

Figure 75: $GaAs_{0.602}P_{0.398}$ open aperture Z-Scan Run #1 at 1000 μW. The blue line is the normalized collected data.

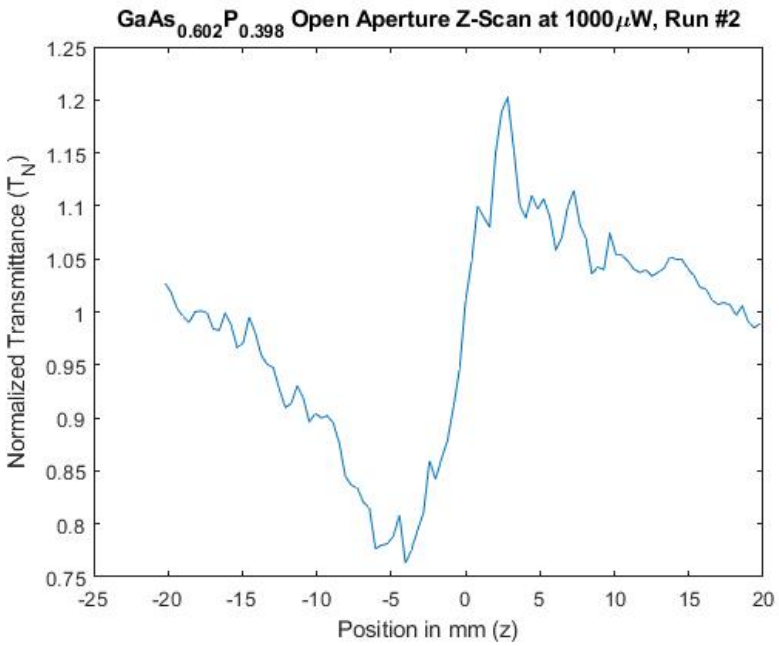

Figure 76: $GaAs_{0.602}P_{0.398}$ open aperture Z-Scan Run #1 at 1000 μW. The blue line is the normalized collected data.

run, nothing conclusive can be determined about β. Because there are many defects on both sides of the sample affecting the transmittance of the sample as it moved, the existence of an appreciable β cannot be confidently determined either.

The left part of Figure 76 looks like half of an OA run. However, the T_N low point is at least 3 mm to the right of the focus and is already at the minimum for Equation 71 to fit without creating an upwards spike in the middle. This dip could have been caused by the high number of surface defects instead of β. Attempting to fit this would require ignoring the quality of the sample and too much data manipulation to have any confident results.

Several runs were performed on the larger $GaAs_{0.74}P_{0.26}$ sample, with multiple runs performed when the pump power was 1000 μW (Figure 77), 400 μW (Figure 78), and 200 μW (Figure 79). The runs not presented in figures resulted in similar or more asymmetric graphs and are shown in Appendix D4.3. The sample was moved in between each run to try to locate an area on its surface that could

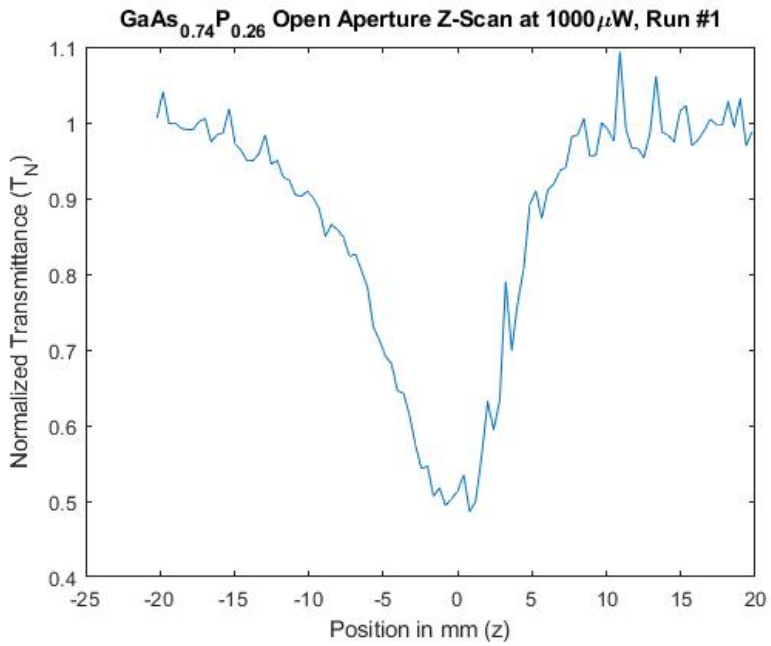

Figure 77: $GaAs_{0.74}P_{0.26}$ open aperture Z-Scan Run #1 at 1000 μW. The blue line is the normalized collected data.

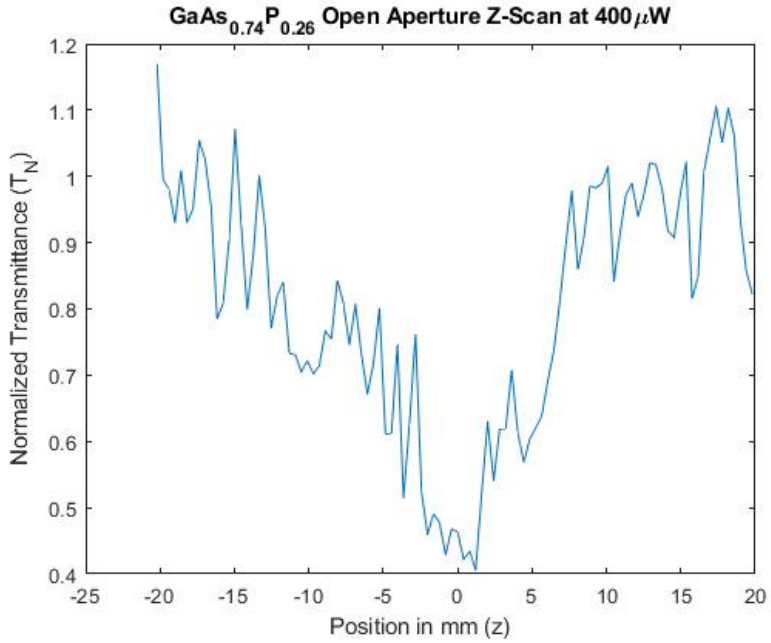

Figure 78: $GaAs_{0.74}P_{0.26}$ open aperture Z-Scan run at 400 μW. The blue line is the normalized collected data.

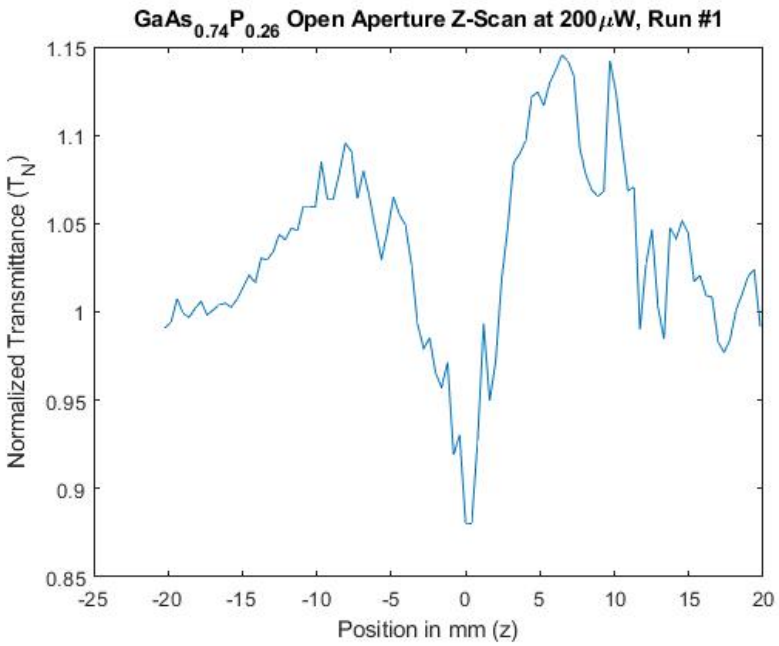

Figure 79: $GaAs_{0.74}P_{0.26}$ open aperture Z-Scan Run #1 at 200 μW. The blue line is the normalized collected data.

produce a favorable run, which never happened. For the 1000 μW and the 400 μW runs, they have the general OA shape to them; however, the minimum for each of these is around 50% T_N, which is substantially lower than the GaAs sample at 1000 μW (80%). Additionally, the 400 μW run drops as far as the 1000 μW runs, which obviously should not happen since 2PA is intensity dependent. The 200 μW runs hardly resemble the OA shape. Due to the inconsistencies in the data, none of these runs were even attempted to be fit to determine a β value. As with the $GaAs_{0.602}P_{0.398}$ samples, these inconsistencies arise from the pump irradiating different areas of the uneven surface as the sample is translated, and from the ever growing pump instability, which was reaching 55% during the later runs. Therefore, nothing conclusive can be determined about β at this wavelength for this ternary compound.

4.2.4 Z-Scan Summary

Table 8 summarizes the results obtained from the Z-Scan experiment.

Table 8: Two Photon Absorption β and Nonlinear Refractive Index n_2 Values Obtained from the Z-Scan Experiment

	ZnSe	GaAs	GaP	$GaAs_{0.602}P_{0.398}$	$GaAs_{0.74}P_{0.26}$	$Sn_2P_2S_6$
β cm/GW	0^c	$12.00^{d,e}$	0^c	X^f	X^f	0^c
$n_2 \times 10^{-5}$ cm^2/GW	1.196^g	$44.89^{g,h}$	X^i	X^i	X^i	X^i

a: Values at 1550 nm.
b: Pump unstable for measurements.
c: β value indistinguishable from noise.
d: Pump stable for these runs only.
e: Average of two values obtained: 12.28 and 11.73 cm/GW.
f: Poor sample quality prevented accurate measurement.
g: Presented in Appendix D.
h: Only positive n_2 obtained; more than double theoretical value.
i: No runs attempted.

V. Conclusions

This chapter will answer the research questions posed in Section 1.4, list the contributions made from this thesis, and discuss the areas of future research before concluding with an overall summary of the thesis.

5.1 Revisiting the Research Questions

1. Does $GaAs_xP_{1-x}$ allow access to higher d-coefficients similar to GaAs while having a lower β like GaP? If so, what stoichiometry best accomplishes this? These questions could not be answered in this thesis. Only two different stoichiometric samples were examined, but due to their poor surface qualities, neither were able to be accurately characterized for comparison with GaAs or GaP.

This answer does not mean that nothing was learned about the ternary samples. Both stoichiometries did produce SHG output in the Maker Fringe experiment. This shows that creating ternaries could result frequency conversion devices as good as and possibly better than those based on the binary compounds.

2. Can an effective method for measuring the d-coefficients of $Sn_2P_2S_6$ be developed for the Instensity-scan Method of the Maker Fringe experiment? While the data for $Sn_2P_2S_6$ did not yield any usable results, the method used to obtain d_{eff} is viable.

The method for measuring the d-coefficients starts with determining the transmitted pump angle and refractive indices for the pump and harmonic waves. Since this part can be cumbersome, a Microsoft Excel code was created to quickly determine the refractive indices. The next step is to input the angle and refractive indices into the same code used for the cubic crystals (Appendix B). Should the refractive indices be the same meaning it is phasematched, the sinc^2 term is set to 1. The code will then produce a d_{eff}, which must then be scaled by $2\sqrt{2}$ if this scaling factor has not

been resolved. To determine the individual d-coefficients, the experiment must be redone at multiple different orientations until enough data is collected. Redoing the experiment multiple times makes the I-scan Method less efficient than the Rotation Method, which could require as little as one data set to extract all the d-coefficients [11].

5.2 Contributions

- A working Maker Fringe experiment is now set up at AFRL/RY. Having this experimental setup at AFRL/RY will allow the continuation of this thesis and other research projects involving characterizing d-coefficient, especially the $GaAs_xP_{1-x}$ ternary compounds which are grown at AFRL/RY. The main tasks performed in setting up the experiment are listed below.
  - Modified the existing pump laser system to produce a pulsed beam.
  - Calculated the average power of the output from the collected output peak-to-peak Voltage.
  - Created LabView code for data collection and rotation mount control. Designed alternative methods for performing both should the code produce errors.
  - Adjusted pump train to reduce the fluence of the pump on the sample, allowing more samples like GaAs to be characterized with this setup.
- A coding error was identified in the d_{eff} calculation Excel worksheet. The specific error was using the wrong polarization for the SHG wave exiting the sample, which resulted in the incorrect percentage of the wave exiting the sample. Correcting this coding mistake will result in future analyses being more accurate.

- $Sn_2P_2S_6$ was demonstrated to not have appreciable 2PA at 1550 nm.
- Demonstrated $\chi^{(2)}$ frequency conversion in $GaAs_xP_{1-x}$ ternaries.
- Highlighted the limitations and sensitivities of both experiments (Maker Fringe and Z-Scan) for characterizing the $GaAs_xP_{1-x}$ ternaries and birefringent materials.
- A Microsoft Excel code was created to aide in calculating the refractive index of $Sn_2P_2S_6$ when transmitting a light wave at arbitrary angles of incidence.

5.3 Future Work and Recommendations

This section will discuss future work and recommendations related to this thesis, starting with the experimental setups and ending with the materials.

5.3.1 Maker Fringe Experiment

The experiment constructed during this thesis is not automated. With a newer oscilloscope, the SHG data collection can be accomplished using a computer via LabView. The LabView code could then automate the rotation mount, allowing for the Rotation Method to be efficiently performed. This automation would allow for more rotation runs to be performed on birefringent materials in less time, increasing the speed of d-coefficient measurements.

Another recommendation is to address the $2\sqrt{2}$ scaling factor that appeared in the calculations. Ideally, the source of this scaling factor would be found and corrected. But, if that cannot be done, then verify that the scaling factor is $2\sqrt{2}$. With only the ZnSe sample to confidently use, the scaling factor could be 2 instead of $2\sqrt{2}$.

Expand upon the $Sn_2P_2S_6$ refractive index code. Since future research will be examining similar crystals to $Sn_2P_2S_6$, having a code that calculates the refractive

index of these crystals is beneficial.

5.3.2 Z-Scan Experiment

For the Z-Scan experiment, the main recommendation is to not use housing units similar to the ones in Figure 40. The screws used to hold the sample in place is the main reason why many samples were damaged in this thesis. It is hard to determine if the sample is secured versus being slightly loose, often leading to the screw being tightened too much for the sample. This housing unit is secured to the translation stage via magnets. The problem with the magnets is that they can bring the housing unit down with a large enough force to cause a thin sample to break. Replacing the screws with something compressible and the magnets with screws should prevent accidentally damaging the samples while mounting them.

For smaller samples or samples with defects or surface damage, ensure the z-translation stage travels exactly parallel to the z-axis. Small deviations from this could result in the pump irradiating different imperfections or clipping the edge of the sample, leading to asymmetric plots like Figure 75. Also, if the pump starts acting unstable at any point, stop experimentation and correct the instability. This will ensure the data collect is much more reliable than if the pump is left unstable.

5.3.3 $GaAs_xP_{1-x}$ Ternaries

The $GaAs_xP_{1-x}$ ternaries are desired for use in the SWIR, MWIR, and possibly LWIR wavebands. However, experiments on the samples used in this thesis could not provide much information on their properties in the SWIR waveband. So, the first and most important action to take regarding the ternaries is to produce samples with polished, parallel surfaces and no interior defects. The poor surface quality prevented accurate characterization of the d_{14}-coefficients, nonlinear refractive index,

and two photon absorption for the ternary samples. The poor surface quality scattered the pump waves in both experiments, reducing the intensity of harmonic waves detected for the Maker Fringe experiment and creating too much noise for the Z-Scan experiment. Another issue with the poor surface quality is that two of the three samples were damaged in the Maker Fringe experiment before any significant data could be collected. With better quality samples, their NLO properties can be accurately determined and compared with GaAs and GaP.

With better quality samples, Z-Scan experiments can be performed effectively. However, for the Maker Fringe experiment, the thickness of the samples will still be a limiting factor due to the short coherence lengths of the ternaries. As the sample thickness approaches an even number of coherence lengths, the margin of error for d_{eff} increases significantly since the d_{eff} will reach unrealistically high values. Samples with short coherence lengths are more likely to be close to an even number of coherence lengths thick than samples with larger coherence lengths. To reduce the margin of error, a more accurate profilometer should be used to measure the thickness within 0.5 μm or less. If a more accurate profilometer cannot be acquired, then use multiple samples with similar but different thicknesses to ensure that at least one sample is not close to an even number of coherence lengths thick. Another way to reduce error due to thickness would be to polish the samples until their thickness is approximately an odd number of coherence lengths. However, polishing may not be an option if the samples are already thin. A third way to reduce the error would be to use a longer-wavelength pump. With a longer wavelength, the coherence lengths of the ternaries would be longer, reducing the possibility of the sample length being close to an even number of coherence lengths. Although, using a longer wavelength pump would require using Miller's Rule to approximate d_{14} for higher frequency interactions. The current Maker Fringe setup could still be used for birefringent materials and isotropic

materials with longer coherence lengths.

After the production of the ternary samples is improved, the next action is to produce different stoichiometric samples and characterize them. Since the goal of these ternaries is to reduce the β values for GaAs for wavelengths below 1800 nm, the characterizations would be performed at different wavelengths. Trends regarding d_{14}, n_2, and β values can then be observed to assist in determining which stoichiometry would produce the best d_{14} while reducing β.

5.3.4 $Sn_2P_2S_6$ and Related Crystals

SPS has had its d-coefficients, nonlinear refractive index, and 2PA coefficients characterized in the SWIR in literature. The next step would be to redo the n_2 and β characterizations in the MWIR and LWIR wavebands. Doing so will determine if there exists any part of those wavebands that are unsuitable for SPS lasers due to the presence of n_2 or β.

An effort at AFRL/RX is currently underway to dope SPS and crystals with similar composition ($Sn_2P_2Se_6$, $Pb_2P_2S_6$, and $Pb_2P_2Se_6$) with calcium, cadmium, or other elements. The goal of doping SPS is to improve upon the d-coeffiecients SPS already has. The goal of doping the other three similar crystals mentioned is to break their centrosymmetry to allow for $\chi^{(2)}$ nonlinearity. The initial dopants for all of these is calcium and cadmium, but others dopants will be explored should these prove unsuccessful in achieving the goals. Once grown, the next step would be to characterize the doped crystals. The crystals that are non-centrosymmetric should have their d-coefficients characterized by the Maker Fringe experiment and should determine where appreciable nonlinear refractive index or two photon absorption exists in the MWIR and LWIR wavebands with the Z-Scan experiment. Once characterized, these crystals could then be used to create MWIR or LWIR lasers, should their properties

be favorable for such. The centrosymmetric crystals should have their Curie Temperatures determined to assess if further doping could raise the Curie Temperature above room temperature.

5.4 Summary

This thesis examined two groups of materials for viability as coherent light sources in the SWIR, MWIR, and LWIR wavebands: $GaAs_xP_{1-x}$ ternary compounds and $Sn_2P_2S_6$. To help determine if these materials are viable, their nonlinear optical properties need to be characterized, namely d-coefficients, nonlinear refractive index, and two photon absorption. A Maker Fringe experiment was constructed to determine the d-coefficients via the Intensity-scan Method. The Maker Fringe setup and analysis method were verified using ZnSe, albeit with a scaling factor of $2\sqrt{2}$. While each experimental sample demonstrated second harmonic generation, the sample qualities were too poor to deduce any d-coefficients. For the other two properties, an existing Z-Scan method was used. However, issues with the pump stability and time of accessibility occurred. The pump instability combined with the sample quality prevented the determination of n_2 and β for the ternary compounds. Although, $Sn_2P_2S_6$ was demonstrated to not have appreciable two photon absorption at 1550 nm. This thesis laid the foundation for future characterization of $GaAs_xP_{1-x}$ ternary compounds and crystals with similar composition and structure to $Sn_2P_2S_6$.

Appendix A. d-Coefficient Calculations from d_{eff}

This Appendix will describe the different calculations used to determine the d-coefficients from d_{eff} for the cubic crystals.

The polarization equation (Equation 33) for cubic crystals is presented here:

$$\overrightarrow{P}(\omega_1) = 2\epsilon_0 \begin{pmatrix} 0 & 0 & 0 & d_{14} & 0 & 0 \\ 0 & 0 & 0 & 0 & d_{14} & 0 \\ 0 & 0 & 0 & 0 & 0 & d_{14} \end{pmatrix} \begin{pmatrix} E_x(\omega_2)E_x(\omega_3) \\ E_y(\omega_2)E_y(\omega_3) \\ E_z(\omega_2)E_z(\omega_3) \\ E_z(\omega_2)E_y(\omega_3) + E_y(\omega_2)E_z(\omega_3) \\ E_z(\omega_2)E_x(\omega_3) + E_x(\omega_2)E_z(\omega_3) \\ E_y(\omega_2)E_x(\omega_3) + E_x(\omega_2)E_y(\omega_3) \end{pmatrix}, \quad (81)$$

where $\omega_2 = \omega_3$ is the pump frequency and ω_1 is the harmonic frequency [4, 34]. Figure 80 is used to determine where the orientations of the x-, y-, and z-axes [34]. Every cubic sample is z-cut. So, the angle ϕ is the transmitted pump angle, calculated

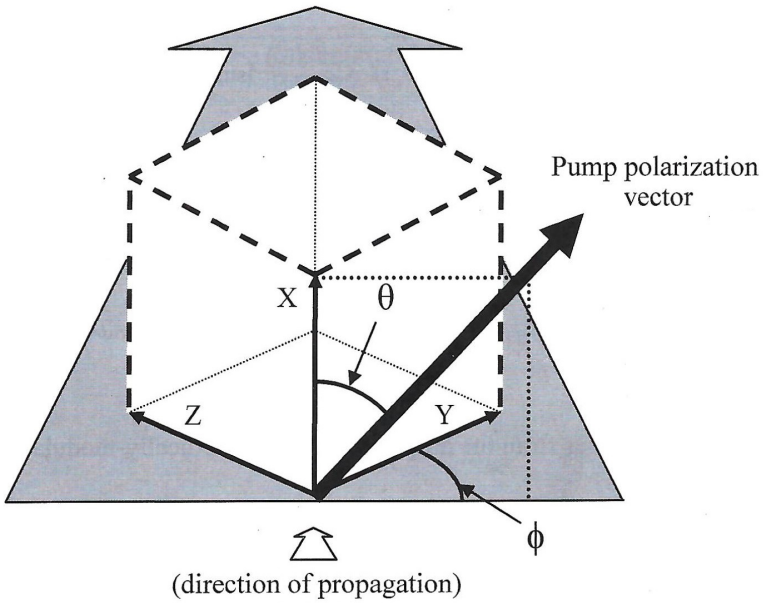

Figure 80: Orientation of cubic cells. This coordinate system is used for calculating d_{14} for the cubic materials. *This figure is modified from [34].*

from the incident pump angle using Snell's Law. The x-axis is picked to not have a dependence on ϕ, where the angle θ correctly orients the x-axis in relation to the pump polarization vector. Using Figure 80, the x-, y-, and z-components of the electric fields are [34]

$$E_x(\omega) = \cos(\theta)|E| \tag{82}$$

$$E_y(\omega) = \sin(\theta)\cos(\phi)|E| \tag{83}$$

$$E_z(\omega) = \cos(\theta)\sin(90^\circ + \phi)|E|, \tag{84}$$

Substituting Equations 82 through 84 into Equation 81 results in

$$\begin{pmatrix} P_x(\omega_s) \\ P_y(\omega_s) \\ P_z(\omega_s) \end{pmatrix} = 2\epsilon_0 d_{14} \begin{pmatrix} 2\sin(\theta)\cos(\theta)\cos^2(\phi) \\ 2\cos(\theta)\sin(\theta)\cos(\phi) \\ 2\cos(\theta)\sin(\theta)\cos(\phi) \end{pmatrix} |E_p|^2, \tag{85}$$

where ω_s is for the SHG wave and E_p is the electric field of the pump [4, 34]. Since most of the incident angles are small and the refractive indices are large, ϕ is less than 8° for all cubic samples. Since $\cos(8^\circ)$ is 0.99, $\cos(\phi)$ will be approximated as 1. Using the identity $2\sin(\theta)\cos(\theta) = \sin(2\theta)$, Equation 85 can be reduced to:

$$|\overrightarrow{P}(\omega_s)| = \sqrt{P_x^2(\omega_s) + P_y^2(\omega_s) + P_z^2(\omega_s)} \tag{86}$$

$$|\overrightarrow{P}(\omega_s)| = 2\epsilon_0 d_{14}\sqrt{3\sin^2(2\theta)}|E_p|^2 \tag{87}$$

$$|\overrightarrow{P}(\omega_s)| = 2\epsilon_0 d_{14}\sqrt{3}\sin(2\theta)|E_p|^2 \tag{88}$$

Comparing Equation 88 to Equation 34, d_{eff} is found below:

$$d_{eff} = d_{14}\sqrt{3}\sin(2\theta). \tag{89}$$

Since the sample was oriented for maximum SHG output, the $\sin(2\theta)$ term equals 1, leaving

$$d_{eff} = d_{14}\sqrt{3}. \tag{90}$$

Therefore, once d_{eff} is calculated for the cubic crystals, it is divided by $\sqrt{3}$ to obtain d_{14}.

Appendix B. Detailed Maker Fringe Calculations

The data analysis for the Maker Fringe experiment uses Microsoft Excel code developed by Shekhar Guha and Joel Murray from AFRL/RX, which will be explained in this Appendix. The code had been designed for analysis on $\bar{4}3m$ crystals (specifically GaAs, GaP, and others), but not for SPS, requiring modifications to the code. The first section will cover the part of the code that calculates d_{eff} line by line. The second section describes how the code was altered for the SPS calculations.

2.1 The d_{eff} Calculation Code

The figures shown in this section are screenshots of the Excel sheet used. The values seen in the figures are for the ZnSe sample.

The first two sections of the code are shown in Figure 81. The purple section is for user inputs, which is sample dependent. $b_{measured}$ is b_{fit}, which is calculated via Matlab. n_p and n_s are the refractive indices for the pump and the SHG wavelengths, calculated via Sellmeier equations or via Vegard's Law for the ternaries and listed in Section 3.3. The thickness was measured with the profilometer, and the angle of

Quantities	Values	Units	SI	
b_measured	6956.1	nJ/(GW/cm^2)^2	6.956E-32	
n_p	2.444954	Δn:	2.444954	
n_s	2.484092	0.039138	2.484092	
thickness	712	µm	7.12E-04	
angle inc	9.25	degrees	0.161442956	rad
T_p (0 if uncoated)	0	at pump AOI; 0<T<1		
T_s (0 if uncoated)	0	at SHG A-O-exit; 0<T<1		
lambda_p	2.09	µm	2.090E-06	
r0	97.45511787	µm	9.7455E-05	
t0	15794.7523	ps	1.58E-08	
pump parallel to plane of inc	TRUE			

Figure 81: Sections 1 and 2 of the d_{eff} calculation code. Note that the fourth column converts the values in the second column to SI units (or degrees to radians).

incidence is the one recorded for each run. Every sample was not coated, so the T_P and T_S parameters are zero; if the sample were coated, the values entered into these cell will prioritize the calculations made later. The blue section is the experiment setup parameters, which do not change for any of the runs. $lambda\_p$ is the pump wavelength. The $r0$ cell is for the beam waist measured $1/e$. $t0$ is the temporal pulse width, also measured $1/e$. The last entry in this section is for the polarization of the pump, which for this code can either be parallel or perpendicular. Since the pump is polarized along the x-axis and the sample is rotated about the y-axis (see Figure 33), the pump will always be polarized parallel to the plane of incidence; thus, for all these runs, this cell is set to "TRUE".

The next section of the code (Figure 82) contains some preliminary calculations to be used later. The pump angle in sample is calculated from the incident angle and n_p using Equation 3 [12]. The SHG angle in sample is the same as the pump's due to the materials being isotropic [4]. The SHG exiting angle is also calculated with Equation 3 [12]. The path length (L_p) takes into account the pump angle in the material, it being equal to $L/\cos(pump\_angle)$. The coherence length is calculated using Equation 44 and the user inputted pump wavelength and refractive indices. The next two entries set up for the sinc^2 calculation, where $sigma$ is just $(L_p/L_c)\times\pi$. Note that if L_p/L_c approaches an even integer, the sinc^2 goes to 0, which results in

angle in sample (pump)	3.76960804	degrees	0.065792072	rad
angle in sample (SHG)	3.76960804	degrees	0.065792072	rad
angle exit (SHG)	9.399402763	degrees	0.164050526	rad
path length	713.5437646	µm	7.1354376E-04	
coherence length	13.3502	µm	1.3350197E-05	
L_path / L_c	53.4482		53.4482	
sigma	167.9124205		1.6791242E+02	
sinc^2 (sigma/2)	8.2432E-05		8.2432E-05	

Figure 82: Section 3 of the d_{eff} calculation code. Note that the fourth column converts the values in the second column to SI units (or radians from degrees).

the code outputting unrealistically high values of d_{eff}.

The next four sections of the code are dedicated to calculating T and R for the pump and the SHG beams using the Fresnel equations. Figure 83 shows the calculations for T and R for the pump respectively, and Figure 84 shows the same calculations but for the SHG wave. The first two cells for each section calculates t or r for either the parallel or the perpendicular waves using Equations 4 through 7 [12]. The next cell in each section chooses which wave to use; since the the *pump parallel*

Pump entering sample	
t_p_par	0.578714264
t_p_perp	0.576068927
t_p	0.578714264
T_p (one surface)	0.827833298
T_p	0.827833298
Pump in sample	
r_p_par	-0.414929755
r_p_perp	0.423931073
r_p	-0.414929755
R_p (one surface)	0.172166702
R_p	0.172166702

Figure 83: Sections 4 and 5 of the d_{eff} calculation code.

SHG exiting sample	
t_s_par	1.437530796
t_s_perp	1.430596896
t_s	1.430596896
T_s (one surface)	0.814586313
T_s	0.814586313
SHG in sample	
r_s_par	0.421305332
r_s_perp	-0.430596896
r_s	-0.430596896
R_s (one surface)	0.185413687
R_s	0.185413687

Figure 84: Sections 6 and 7 of the d_{eff} calculation code.

to plane of inc cell is "TRUE" for all samples, the pump will always use the parallel wave calculations, and the SHG will always use the perpendicular wave calculations. The *(one surface)* cell measures T or R based on the cell directly above it, using Equations 8 and 9 [12]. The last cell in each of these four sections uses the value from the cell directly above it since no sample is coated.

The next section shown in Figure 85 is used to calculate multiple reflection corrections that may be applied at the end, with these multiple reflections being coherent (overlapping waves) or incoherent (not overlapping waves) [8]. F_p is the finesse parameter, used in calculating R_{coh} [8]. R_{inc} is the correction factor for multiple incoherent wave reflections, where the expression was rederived by Guha, Murray, *et al.* to not ignore the differences between the pump and the SHG waves:

$$\mathcal{R}_{inc} = \frac{1 + (R_p^2 R_s)}{(1 - R_s^2)(1 - R_p^4)} \tag{91}$$

where R_p and R_s are the Fresnel reflection coefficients (Equation 8) for the pump and the SHG waves respectively [8, 22]. R_{coh} is the overestimation correction factor due to multiple coherent reflections, with the differences between n_p and n_s neglected:

$$\mathcal{R}_{coh} = \frac{(n+1)^6(n^6 + 15n^4 + 15n^2 + 1)}{2048\pi n^6} \times \int_0^{\pi} \frac{dx}{[1 + F_p \sin^2(2x)][1 + F_p \sin^2 x]^2} \tag{92}$$

F_p	1.036271421
sqrt(R_inc)	1.020886602
sqrt(R_coh)	1.102797768
L*tan(theta_int) / w_x	3.4112E-01
completely incoherent?	FALSE
completely coherent	FALSE

Figure 85: Section 8 of the d_{eff} calculation code.

where F_p is the finesse parameter from before and $n = n_p = n_s$ [8]. The next entry is used to determine if a correction factor should be included, with

$$\frac{L\tan(\theta_{int})}{w_x} = \frac{L_p\tan(\theta_{p-int})}{\sqrt{2}w_0} \tag{93}$$

with θ_{p-int} being the interior pump angle [48]. If either side of Equation 93 is greater than one, then the completely incoherent correction should be applied; if Equation 93 much less than one, then the completely coherent correction should be applied [48]. However, both the "completely incoherent?" and the "completely coherent" cells were FALSE for every cubic crystal examined in this thesis, so these corrections were not applied to them.

The last section calculates d_{eff} and d_{14} (see Figure 86). The *b_true* value is from Equation 56 [22]. d_{eff} is calculated the same as Equation 57, using the corresponding cells from the earlier sections [22]. d_{14} calculations are included in this code, but with the orientations of the samples being different from the ones required in the code, the method provided in Appendix A will be used instead. The last three lines implement the coherent and incoherent corrections to d_{eff} and d_{14}, regardless of which one is relevant.

b_true (AR or UNC)	12592.1765		1.25922E-31	
d_eff	**148.8406145**	**pm/V**	1.48841E-10	m/V
Is (100)?	TRUE			
d14 [if (100)]			3.16839E-10	
d14 [if (110)]			1.289E-10	
d14	**316.8386806**	**pm/V**	3.16839E-10	
Multiple Reflection correction				
	no correction	incoherent	coherent	
d_eff	148.8406145	145.7954431	134.9663727	
d14	316.8386806	310.3563901	287.3044269	

Figure 86: Section 9 of the d_{eff} calculation code. The code does not account for significant digits.

2.2 SPS Modifications

Since SPS is a birefringent material, the most efficient frequency conversion will happen when it is phasematched. For SPS to be phasematched, $\Delta k = 0$, so using Equation 38

$$0 = n_s\omega_s - n_p\omega_p - n_p\omega_p \tag{94}$$

$$0 = n_s(2\omega_p) - 2n_p\omega_p \tag{95}$$

$$2n_p\omega_p = 2n_s\omega_p \tag{96}$$

$$n_p = n_s. \tag{97}$$

The refractive indices for both waves are 2.7716, determined using the method in Appendix C.

Inputting the same value for n_p and n_s causes the L_c calculation to divide by 0 (see Figure 87), affecting the rest of the calculations. Since the coherence length is not a factor when phasematched and is only used when calculating the sinc^2 term, only the sinc^2 cell is modified in Section 3 of the code. The sinc^2 cell is set to 1 since $\text{sinc}^2(0)$=1. The "angle in sample (SHG)" cell was left unchanged since the the pump

angle in sample (pump)	6.401449947	degrees	0.111726378	rad
angle in sample (SHG)	6.401449947	degrees	0.111726378	rad
angle exit (SHG)	18	degrees	0.314159265	rad
path length	1602.994514	µm	1.6029945E-03	
coherence length	#DIV/0!	µm	#DIV/0!	
L_path / L_c	#DIV/0!		#DIV/0!	
sigma	#DIV/0!		#DIV/0!	
sinc^2 (sigma/2)	1		1	

Figure 87: Section 3 of the d_{eff} calculation code, modified for $Sn_2P_2S_6$ calculations. The refractive indices for the pump and harmonic waves being the same results in the dividing by 0 errors seen, which normally also applies to the sinc^2(sigma/2) cell. The sinc^2(sigma/2) cell was manually changed to 1.

and SHG divergence was ignored.

The rest of the code remains the same. Since Poynting vector walkoff is ignored, the SHG angle in the sample is not altered from the pump's angle. The calculated d_{eff} is then used to determine the multiple d-coefficients.

Appendix C. Refractive Index Calculations for the SPS Crystal

This appendix will address the method used to calculate the refractive indices for the SPS crystal, since it is biaxial. A Microsoft Excel code has been created to assist in the calculations. This method can also be applied to other biaxial crystals.

3.1 Coordinate System Transformation Method

The method used to determine the refractive index for the SPS crystal was published by Yin *et al.* in 2007 [54]. This method uses coordinate system transformations to realign the k-vector parallel to a z-axis, allowing the refractive index ellipse to be within an x-y plane for ease of calculations. The method will be rederived here, since the article contains some math errors likely due to translation and publishing errors.

Before any calculations, Figure 30 is used to relate the cut of the SPS sample (abc-coordinate system) to the refractive index coordinate system ($x_1x_2x_3$) [45]. The x_1-, x_2-, and x_3-axes do not have to be ordered such that $n_1 < n_2 < n_3$, where n_1 is the refractive index for the x_1-axis, n_2 for x_2, and n_3 for x_3. Once related, the propagation angles θ and ϕ are determined (see Figure 88). Figure 88 shows the k-vector of a wave in relation to the crystal's refractive index coordinate system; for SPS, the xyz-coordinate system shown here is the $x_1x_2x_3$-coordinate system in Figure 30 [54]. Figure 89 is the same as Figure 88 except the refractive index ellipse is drawn perpendicular to the k-vector and effects from Poynting vector walkoff are included [54]. The relationships between S and k and between E and D are illustrated in Figure 10. From Figure 89, the refractive indices for the "slow" and the "fast" waves correspond to the intersection of the E_1 and E_2 with the ellipse, respectively. The fast-wave experiences a lower refractive index, and the slow-wave a higher n. The following calculations are to move the ellipse shown in Figure 89 from existing

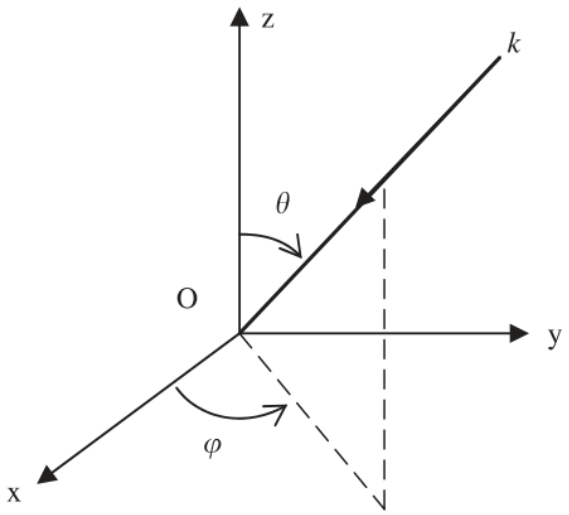

Figure 88: Light wave's k-vector in relation to the refractive index coordinate system of a biaxial crystal. The light wave is traveling at some arbitrary propagation direction with respect to the refractive index coordinate system, with θ being the angle between the z-axis and the k-vector and φ being the angle between the x-axis and the k-vector within the x-y plane. *This figure is from [54].*

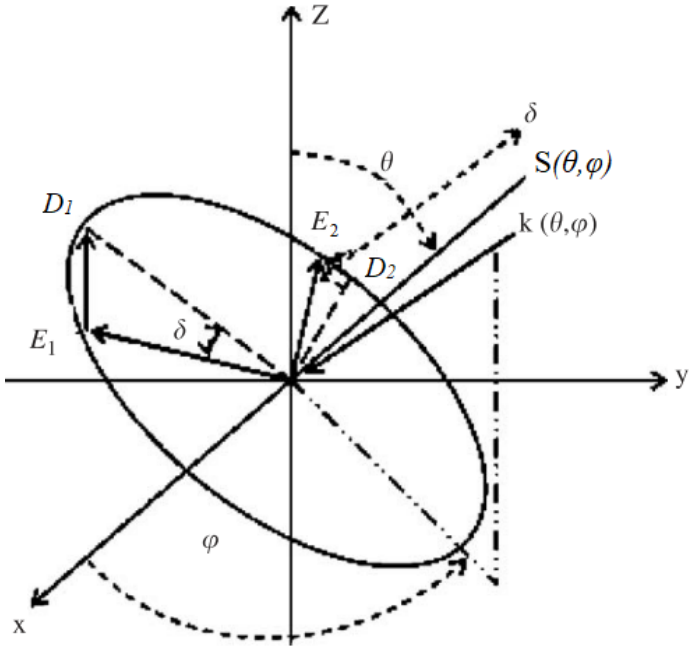

Figure 89: Refractive index ellipse for arbitrary k-vector in a biaxial crystal. The angle δ is the Poynting vector walkoff angle, which deviates the electric fields of the slow-wave (E_1) and the fast-wave (E_2) from the major and minor axis of the ellipse. *This figure is modified from [54].*

in a three-dimensional space to a two-dimensional plane.

To calculate the refractive index of wave travelling within a biaxial crystal, the equation for an ellispoid is used:

$$\frac{x^2}{n_1^2} + \frac{y^2}{n_2^2} + \frac{z^2}{n_3^2} = 1, \tag{98}$$

where n_1, n_2, and n_3 are the refractive indices along the x-axis, y-axis, and z-axis, respectively [4, 54]. The relationship between n_1, n_2, and n_3 does not matter for this method, allowing it to be used with the SPS coordinate system in Figure 30. The first coordinate system transformation involves rotating the k-vector about the z-axis by φ [54]. The relationship between the two coordinate systems is

$$\begin{pmatrix} x \\ y \\ z \end{pmatrix} = \begin{pmatrix} \cos\varphi & -\sin\varphi & 0 \\ \sin\varphi & \cos\varphi & 0 \\ 0 & 0 & 1 \end{pmatrix} \begin{pmatrix} x' \\ y' \\ z' \end{pmatrix}. \tag{99}$$

Equation 99 results in $x = x'\cos\varphi - y'\sin\varphi$ and $y = x'\sin\varphi + y'\cos\varphi$. Substituting these into Equation 98 gives

$$\begin{aligned}(x')^2\left(\frac{\cos^2\varphi}{n_1^2} + \frac{\sin^2\varphi}{n_2^2}\right) + (y')^2\left(\frac{\sin^2\varphi}{n_1^2} + \frac{\cos^2\varphi}{n_2^2}\right) \\ + x'y'\sin(2\varphi)\left(\frac{1}{n_2^2} - \frac{1}{n_1^2}\right) + \frac{(z')^2}{n_3^2} = 1.\end{aligned} \tag{100}$$

The next coordinate system transformation involves rotating about the y′-axis by θ, which moves the refractive index ellipse entirely into the x″y″-plane [54]. The

relationship corresponding to this transformation is

$$\begin{pmatrix} x' \\ y' \\ z' \end{pmatrix} = \begin{pmatrix} \cos\theta & 0 & \sin\theta \\ 0 & 1 & 0 \\ -\sin\theta & 0 & \cos\theta \end{pmatrix} \begin{pmatrix} x'' \\ y'' \\ z'' \end{pmatrix}. \tag{101}$$

Substituting the x′ and z′ values from Equation 101 into Equation 100 gives

$$\begin{aligned} &(x'')^2 \left[\left(\frac{\cos^2\varphi}{n_1^2} + \frac{\sin^2\varphi}{n_2^2} \right) \cos^2\theta + \frac{\sin^2\theta}{n_3^2} \right] \\ &+ (y'')^2 \left(\frac{\sin^2\varphi}{n_1^2} + \frac{\cos^2\varphi}{n_2^2} \right) \\ &+ (z'')^2 \left[\left(\frac{\cos^2\varphi}{n_1^2} + \frac{\sin^2\varphi}{n_2^2} \right) \sin^2\theta + \frac{\cos^2\theta}{n_3^2} \right] \\ &+ x''y'' \sin(2\varphi) \cos\theta \left(\frac{1}{n_2^2} - \frac{1}{n_1^2} \right) \\ &+ y''z'' \sin(2\varphi) \sin\theta \left(\frac{1}{n_2^2} - \frac{1}{n_1^2} \right) \\ &+ x''z'' \sin(2\theta) \left[\left(\frac{\cos^2\varphi}{n_1^2} + \frac{\sin^2\varphi}{n_2^2} \right) - \frac{1}{n_3^2} \right] = 1. \end{aligned} \tag{102}$$

With this coordinate system complete, the refractive index ellipse is now within the x″y″-plane. As such, there is no z″ component of the ellipse. Thus, z″ = 0, simplifying Equation 102 to

$$\begin{aligned} &(x'')^2 \left[\left(\frac{\cos^2\varphi}{n_1^2} + \frac{\sin^2\varphi}{n_2^2} \right) \cos^2\theta + \frac{\sin^2\theta}{n_3^2} \right] \\ &+ (y'')^2 \left(\frac{\sin^2\varphi}{n_1^2} + \frac{\cos^2\varphi}{n_2^2} \right) \\ &+ x''y'' \sin(2\varphi) \cos\theta \left(\frac{1}{n_2^2} - \frac{1}{n_1^2} \right) = 1. \end{aligned} \tag{103}$$

To simplify the equations going forward, the following substitutions are used:

$$A = \left(\frac{\cos^2\varphi}{n_1^2} + \frac{\sin^2\varphi}{n_2^2}\right)\cos^2\theta + \frac{\sin^2\theta}{n_3^2}, \tag{104}$$

$$B = \frac{\sin^2\varphi}{n_1^2} + \frac{\cos^2\varphi}{n_2^2}, \tag{105}$$

$$C = \sin(2\varphi)\cos\theta\left(\frac{1}{n_2^2} - \frac{1}{n_1^2}\right). \tag{106}$$

With these substitutions, Equation 103 becomes

$$A(x'')^2 + B(y'')^2 + Cx''y'' = 1. \tag{107}$$

One final coordinate system transformation accounts for Poynting vector walkoff [54]. Looking at Figure 89, the electric fields E_1 and E_2 are misaligned from the long- and short-axes of the ellipse by the Poynting vector walkoff angle δ, where E_1 and E_2 are the electric fields for the slow-wave and the fast-wave, respectively. By rotating about the z'' by the walkoff angle δ, the following relationship is used:

$$\begin{pmatrix} x'' \\ y'' \\ z'' \end{pmatrix} = \begin{pmatrix} \cos\delta & -\sin\delta & 0 \\ \sin\delta & \cos\delta & 0 \\ 0 & 0 & 1 \end{pmatrix} \begin{pmatrix} x''' \\ y''' \\ z''' \end{pmatrix}. \tag{108}$$

Substituting the x''' and y''' values from Equation 108 into Equation 107 gives

$$\begin{aligned} &(x''')^2\left[A\cos^2\delta + B\sin^2\delta + \frac{1}{2}C\sin(2\delta)\right] \\ &+ (y''')^2\left[A\sin^2\delta + B\cos^2\delta - \frac{1}{2}C\sin(2\delta)\right] \\ &+ x'''y'''\left[-A\sin(2\delta) + B\sin(2\delta) + C\cos(2\delta)\right] = 1. \end{aligned} \tag{109}$$

Since the equation for this ellipse is $(x''')^2/(n_1''')^2 + (y''')^2/(n_2''')^2 = 1$, the x''' y'''

term must equal zero [54]. Doing so allows the calculation of δ:

$$tan(2\delta) = \frac{-C}{B-A} \tag{110}$$

$$tan(2\delta) = \frac{-\sin(2\varphi)\cos\theta\left(\frac{1}{n_2^2}-\frac{1}{n_1^2}\right)}{\left(\frac{\sin^2\varphi}{n_1^2}+\frac{\cos^2\varphi}{n_2^2}\right)-\left[\left(\frac{\cos^2\varphi}{n_1^2}+\frac{\sin^2\varphi}{n_2^2}\right)\cos^2\theta+\frac{\sin^2\theta}{n_3^2}\right]}. \tag{111}$$

Should there be no walkoff or walkoff is ignored, $\delta = 0$. The refractive index values for this new ellipse (n_1''' and n_2''') are [54]

$$\begin{aligned}\frac{1}{n_1'''} = \quad & \left[\left(\frac{\cos^2\varphi}{n_1^2}+\frac{\sin^2\varphi}{n_2^2}\right)\cos^2\theta+\frac{\sin^2\theta}{n_3^2}\right]\cos^2\delta \\ & +\left(\frac{\sin^2\varphi}{n_1^2}+\frac{\cos^2\varphi}{n_2^2}\right)\sin^2\delta+\frac{1}{2}\sin(2\varphi)\cos\theta\sin(2\delta)\left(\frac{1}{n_2^2}-\frac{1}{n_1^2}\right);\end{aligned} \tag{112}$$

$$\begin{aligned}\frac{1}{n_2'''} = \quad & \left[\left(\frac{\cos^2\varphi}{n_1^2}+\frac{\sin^2\varphi}{n_2^2}\right)\cos^2\theta+\frac{\sin^2\theta}{n_3^2}\right]\sin^2\delta \\ & +\left(\frac{\sin^2\varphi}{n_1^2}+\frac{\cos^2\varphi}{n_2^2}\right)\cos^2\delta-\frac{1}{2}\sin(2\varphi)\cos\theta\sin(2\delta)\left(\frac{1}{n_2^2}-\frac{1}{n_1^2}\right).\end{aligned} \tag{113}$$

The refractive indices written in Equations 112 and 113 are the same as in [54], but the walkoff angle presented in Equation 111 is different from [54].

3.2 Accounting for the Indicatrix α

As mentioned in Section 2.3.3, the indicatrix α of SPS (see Figure 30) is wavelength dependent, altering the locations of the axes for the x-z plane between the pump and harmonic waves [45]. This change in α between the pump and harmonic waves is accounted for in $\Delta\alpha = \alpha_p - \alpha_s$, where α_p is the indicatrix for the pump and α_s is the indicatrix for the harmonic wave. The indicatrix for the pump is larger due to dispersion, so $\Delta\alpha$ is a positive value [45]. When accounting for α, the pump wave uses Equations 111 through 113 without any changes, but for the harmonic wave, substitute θ with $\theta - \Delta\alpha$ for Equations 111 through 113.

Figure 90 shows the coordinate system of the harmonic wave in relation to the pump wave. The solid axes are the x- and z-axes for the harmonic wave, and the dashed axes are the x- and z-axes for the pump wave. The difference between the two coordinate systems is a rotation about the y-axis by $\Delta\alpha$. The angles θ and φ are still in relation to the pump axes, not to the harmonic axes. Instead of re-deriving the equations, an explanation of what occurs will be presented. This method can be applied if the indicatrix is within the x-z, x-y, or y-z plane of crystal's refractive index coordinate system. If α is not within the x-z plane, reorient the axes to place α within the new x-z plane and adjust θ and φ accordingly.

For the first transformation from xyz to x′y′z′ for the harmonic wave, the rotation occurs about the (z+$\Delta\alpha$)-axis by φ (see Figure 91). This rotation places the k-vector within the x′z′-plane. The angle between the k-vector and the (z′+$\Delta\alpha$)-axis is still θ, and the angle between the k-vector and the z′-axis is $\theta - \Delta\alpha$. For the second

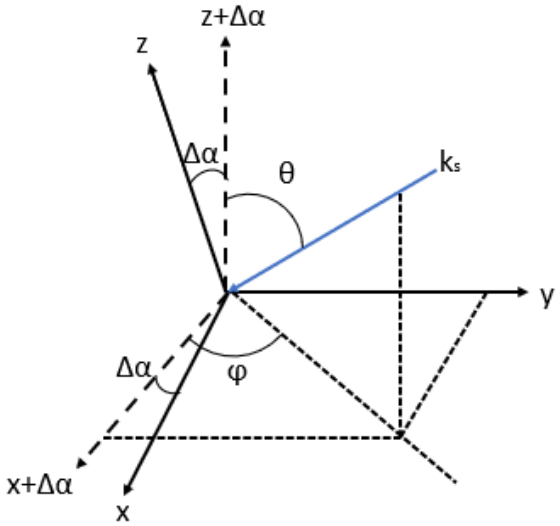

Figure 90: Refractive index coordinate systems for $Sn_2P_2S_6$ for pump and harmonic wavelengths. The xyz-axes correspond to the harmonic wave and the (x+$\Delta\alpha$)y(z+$\Delta\alpha$)-axes correspond to the pump wave, where $\Delta\alpha$ is the difference in indicatrix angles between the pump and harminic waves. k_s is the k-vector for the harmonic wave.

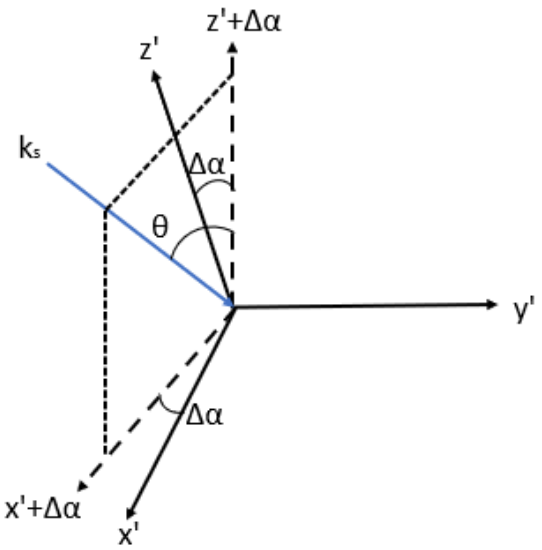

Figure 91: New refractive index coordinate systems for $Sn_2P_2S_6$ for pump and harmonic wavelengths. The x′y′z′-axes correspond to the harmonic wave and the (x′+$\Delta\alpha$)y′(z′+$\Delta\alpha$)-axes correspond to the pump wave, where $\Delta\alpha$ is the difference in indicatrix angles between the pump and harmonic waves. k_s is the k-vector for the harmonic wave.

transformation, the rotation occurs about the y′-axis by $\theta - \Delta\alpha$. This aligns the k-vector with the z′′-axis. The (x′′+$\Delta\alpha$)- and (z′′+$\Delta\alpha$)-axes are now removed from consideration, as the k-vector will no longer be rotated about the pump's axes. The rest of the calculations are the same from here on.

Appendix D. Additional Experimental Results

This Appendix compiles the Maker Fringe and Z-Scan experimental runs that were not addressed in the thesis proper due to either redundancy or irrelevance.

4.1 GaP Maker Fringe Run

Unfortunately for the GaP sample, its L_p/L_c parameter is 70.05, meaning that its length is very close to an even integer number of coherence lengths. This leads to the sinc^2 term to approach zero in the denominator of Equation 57, repeated here:

$$d_{eff} = \sqrt{\frac{b\lambda_p^2 n_p^2 n_s c\epsilon_0}{(2\sqrt{2}\pi^{7/2})L^2 w_0^2 t_0 sinc^2(\frac{\sigma}{2})}}.$$

This results in an unrealistically large d_{eff}. Before altering the thickness, the corrected d_{14} value is 77.30 pm/V, but by looking at Figure 92, it grows to the absurd value of 3151 pm/V as the sinc^2 term approaches 0. The expected d_{14} value is 53.1 pm/V, which can be obtained on both sides of the spike. The analysis method used currently does not have a workaround for this scenario, so no conclusions can be made on the d_{14} coefficient. Due to time constraints, another GaP sample could not be obtained for another run.

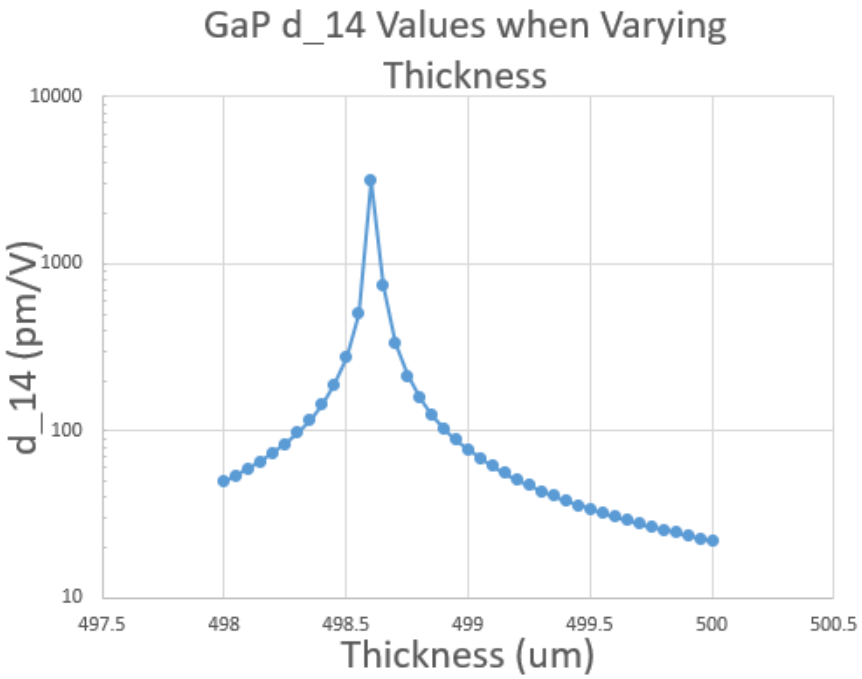

Figure 92: Plot of d_{14} values for GaAs based on thickness. The thickness is varied between ± 1 μm, substituted into Equation 57, divided by $\sqrt{3} \times 2\sqrt{2}$, and plotted. Note that the vertical axis is in log scale.

4.2 Additional $Sn_2P_2S_6$ Open Aperture Z-Scan Runs

This section shows the plots for the other three 1mW and the other two 5mW OA runs mentioned in Section 4.2.2.2. With the general shapes of these graphs being similar to Figures 73 and 74, these were not presented in Chapter 4.

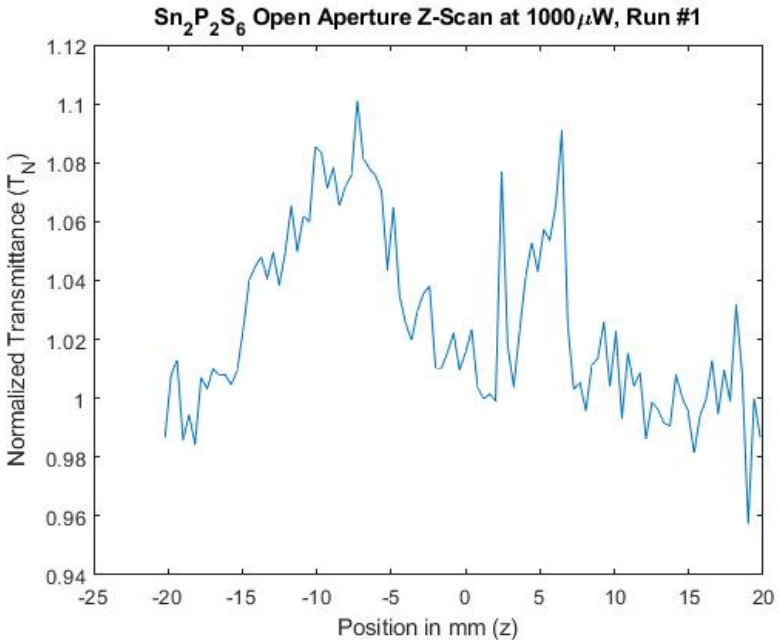

Figure 93: $Sn_2P_2S_6$ open aperture Z-Scan Run #1 at 1000 μW. The blue line is the normalized collected data.

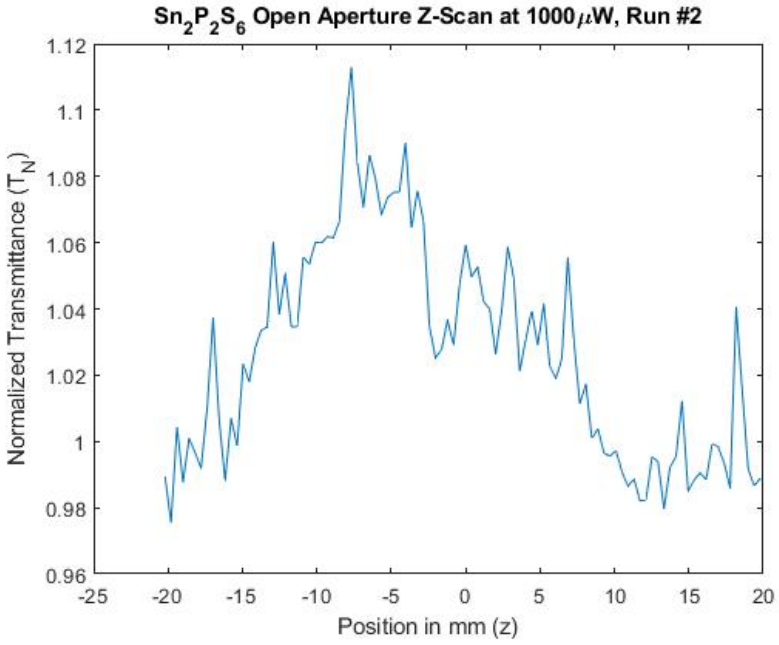

Figure 94: $Sn_2P_2S_6$ open aperture Z-Scan Run #2 at 1000 μW. The blue line is the normalized collected data.

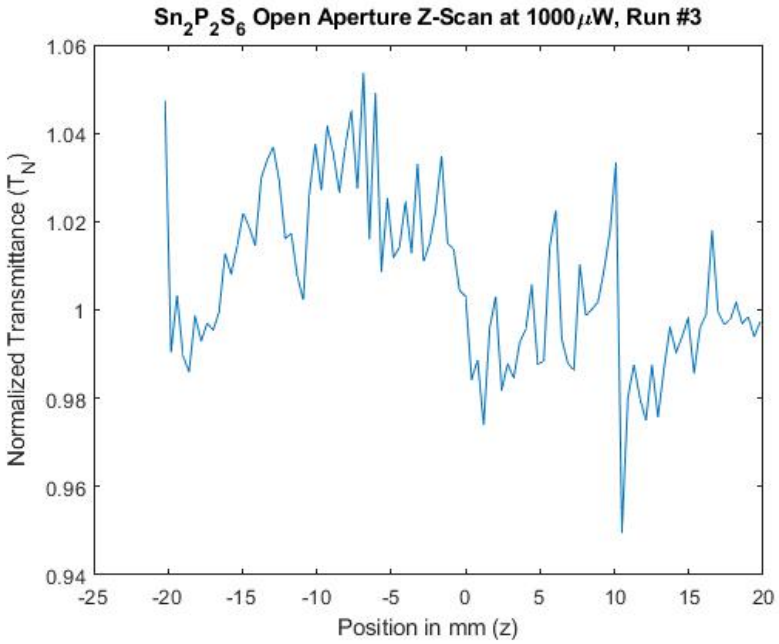

Figure 95: $Sn_2P_2S_6$ open aperture Z-Scan Run #3 at 1000 μW. The blue line is the normalized collected data.

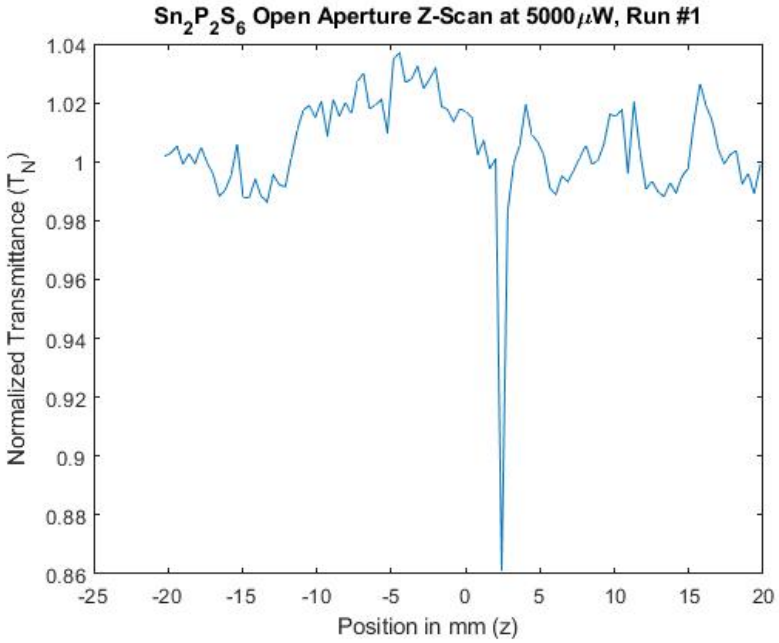

Figure 96: $Sn_2P_2S_6$ open aperture Z-Scan Run #1 at 5000 μW. The blue line is the normalized collected data. The minimum point resulted from interference on the sample surface.

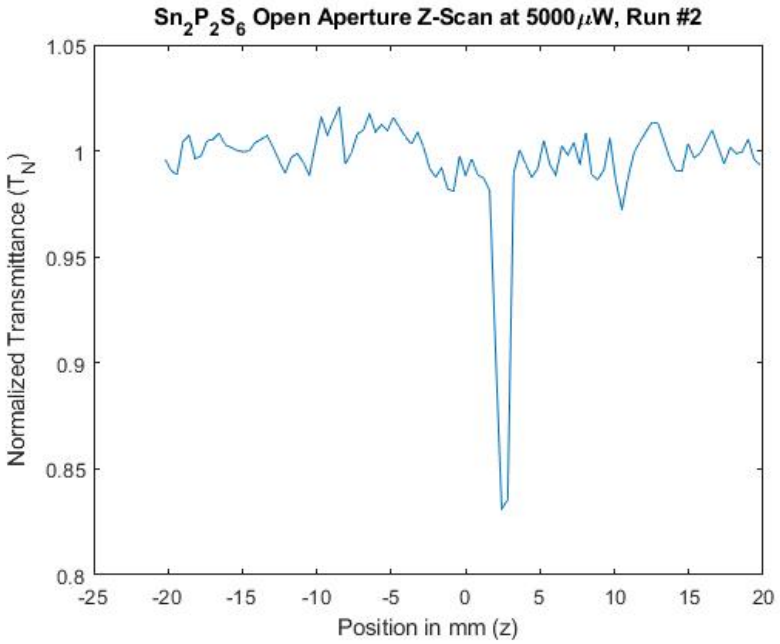

Figure 97: $Sn_2P_2S_6$ open aperture Z-Scan Run #2 at 5000 μW. The blue line is the normalized collected data. The minimum point resulted from interference on the sample surface.

4.3 Additional $GaAs_{0.74}P_{0.26}$ Open Aperture Z-Scan Runs

This section shows the plots of the two $GaAs_{0.74}P_{0.26}$ OA runs not presented in Chapter 4, one at 1000 μW (Figure 98) and one at 200 μW (Figure 99). These two runs added no additional information to the discussion, hence their placement here.

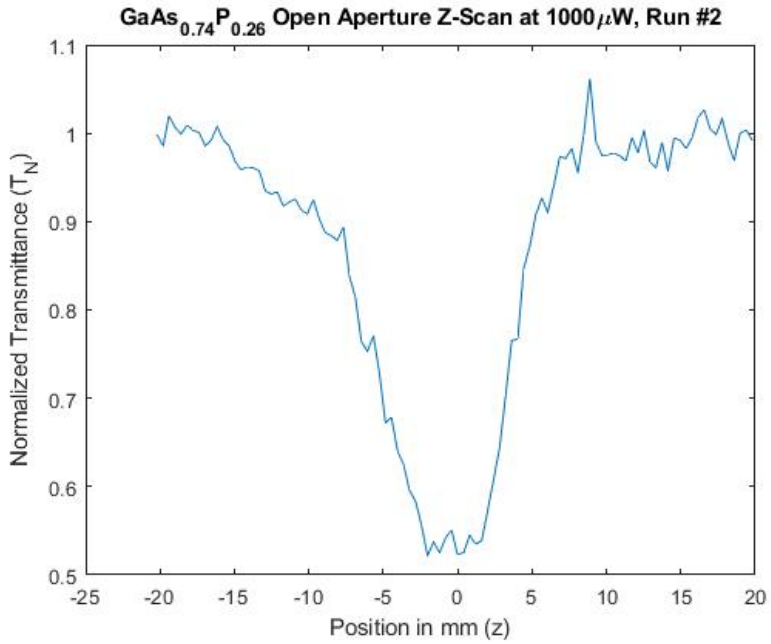

Figure 98: $GaAs_{0.74}P_{0.26}$ open aperture Z-Scan Run #2 at 1000 μW. The blue line is the normalized collected data.

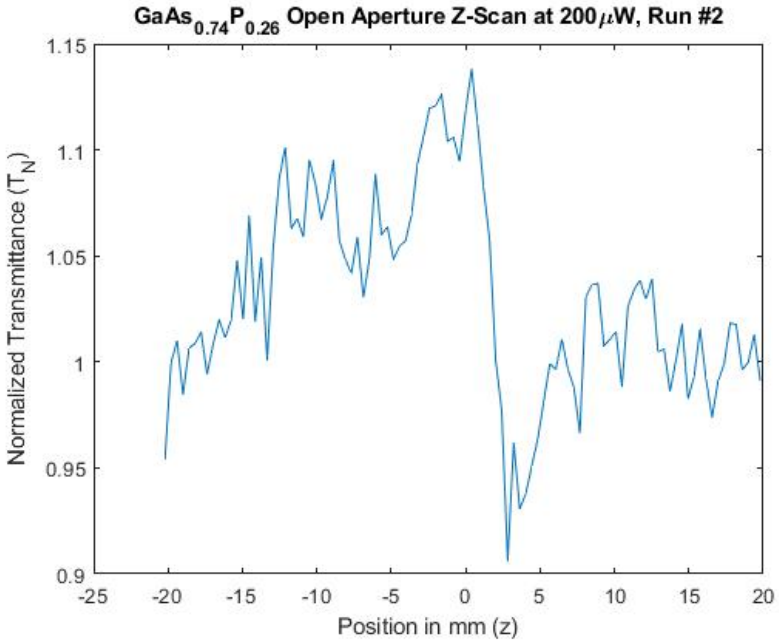

Figure 99: $GaAs_{0.74}P_{0.26}$ open aperture Z-Scan Run #2 at 200 μW. The blue line is the normalized collected data.

4.4 GaAs Z-Scan Runs with Unstable Pump

Other than the runs analyzed in Section 4.2.1, all GaAs runs were conducted while the pump was unstable. Multiple OA runs were conducted with the unstable pump, but Figure 100 shows the only analyzable OA run done at 200 μW, since the higher power runs reduced T_N too low. The best fit for this data used a beam waist of 36.59 μm instead of 38.90 μm. With the pump instability, a 6% drop in beam waist size is reasonable. However, the β value obtained from this fit is 29.05 cm/GW, almost three times the theoretical value. As such, this run is unreliable, and its β value should not be used.

In addition to the OA runs, three 200 μW CA GaAs runs were performed (Figures 101, 102, and 103). For these runs, the only parameter that was calculated from the fit equation is n_2. These runs used the w_0 value of 36.59 μm determined from the 200 μW run and a realistic β value of 12 cm/GW, which is the average of the two β values obtained in Section 4.2.1. By observation, these fits are poor since

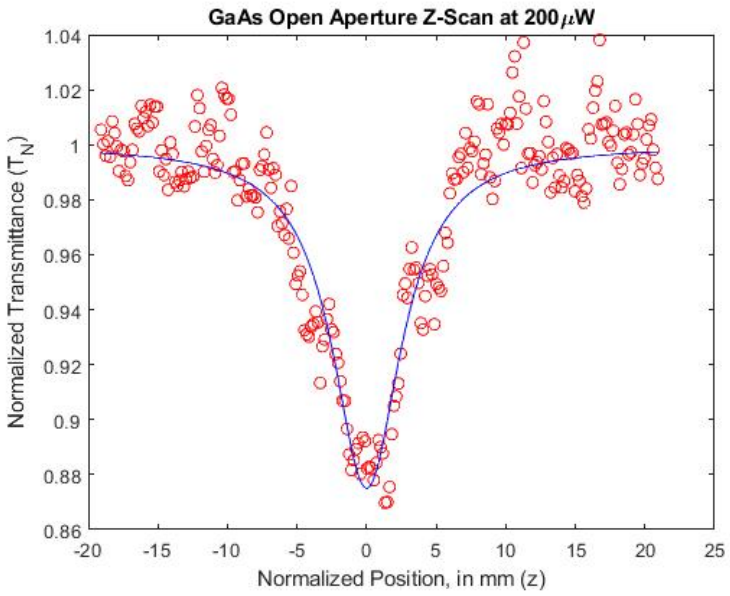

Figure 100: GaAs open aperture Z-Scan run at 200 μW. The red circles are the collected data, and the blue line is the fit Equation 71.

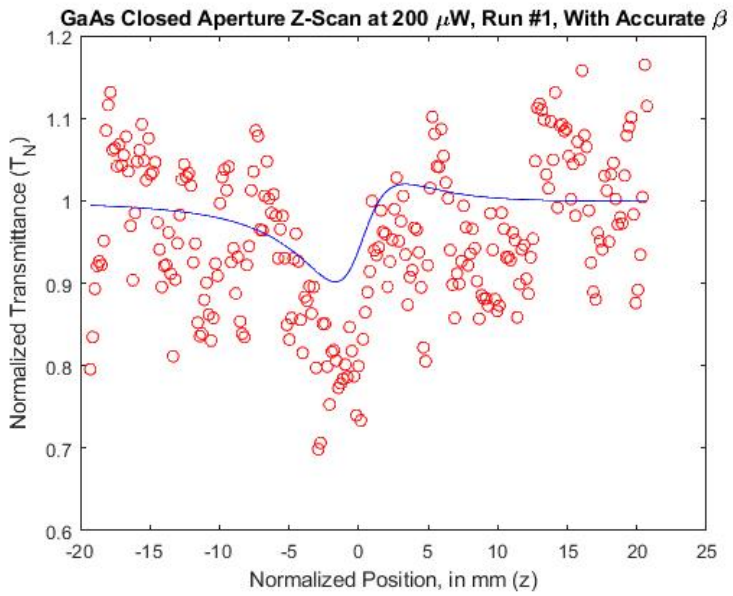

Figure 101: GaAs closed aperture Z-Scan Run #1 at 200 μW with realistic two photon absorption coefficient. The red circles are the collected data, and the blue line is the fit Equation 80.

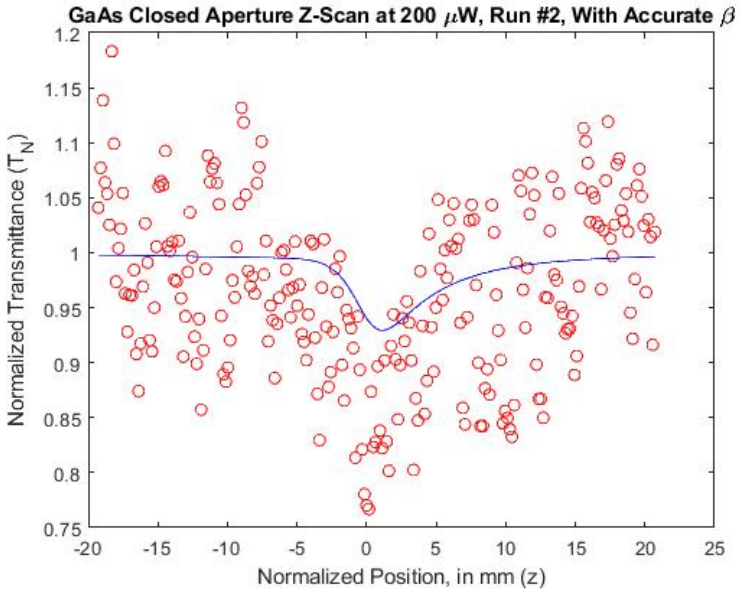

Figure 102: GaAs closed aperture Z-Scan Run #2 at 200 μW with realistic two photon absorption coefficient. The red circles are the collected data, and the blue line is the fit Equation 80.

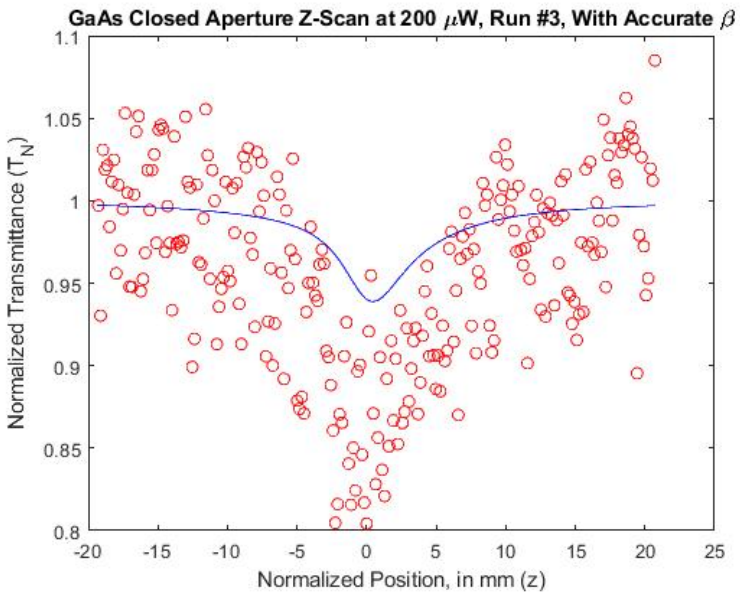

Figure 103: GaAs closed aperture Z-Scan Run #3 at 200 μW with realistic two photon absorption coefficient. The red circles are the collected data, and the blue line is the fit Equation 80.

they do not follow the data. Runs 2 and 3 have an additional problem in that the n_2 value it produces is negative (-1.891 $\times$ 10^{-4} cm^2/GW and -6.004$\times 10^{-4}$ cm^2/GW), contrary to the positive values shown in Figure 27. The n_2 value for Run 1 is 4.488 $\times$ 10^{-4} cm^2/GW, more than double of what it should be, but with such a poor fit, this result is unreliable.

These CA runs have better-looking fits when using the β value from the 200 μW OA run (29.05 cm/GW), as shown in Figures 104, 105, and 106 for Runs 1, 2, and 3, respectively. Run 1 has a better fit, but its fitted n_2 value is 4.490 $\times$ 10^{-4} cm/GW, which is about the same as from the lower β fit. Runs 2 and 3 still have negative n_2 values at -1.889×10^{-4} cm/GW and -5.981$\times 10^{-4}$ cm/GW, which are also about the same as with the lower β fits.

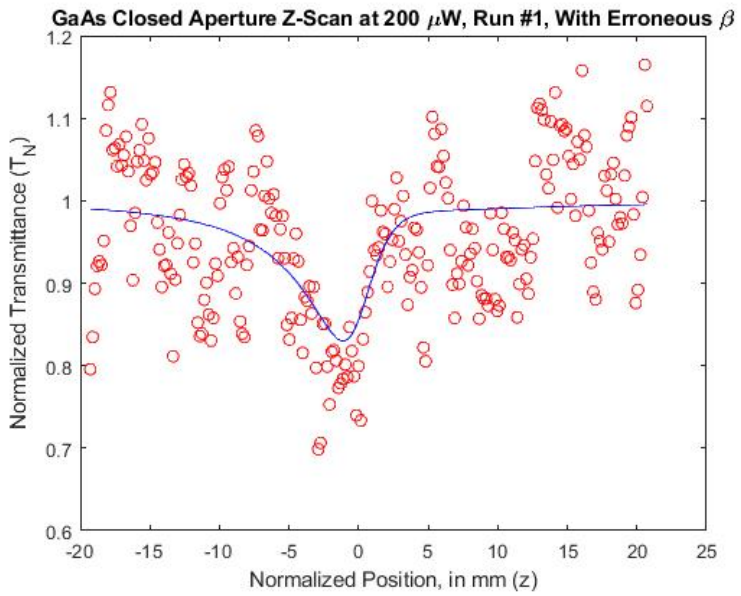

Figure 104: GaAs closed aperture Z-Scan Run #1 at 200 μW with unrealistic two photon absorption coefficient. The red circles are the collected data, and the blue line is the fit Equation 80.

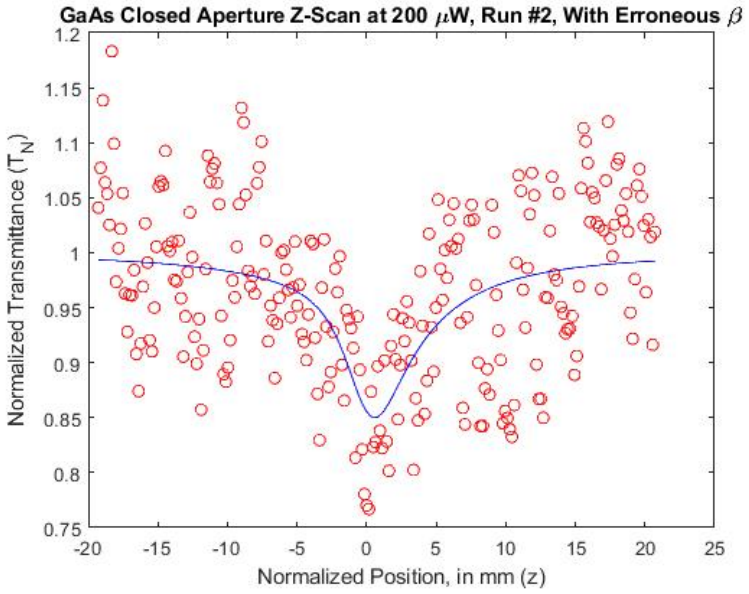

Figure 105: GaAs closed aperture Z-Scan Run #2 at 200 μW with unrealistic two photon absorption coefficient. The red circles are the collected data, and the blue line is the fit Equation 80.

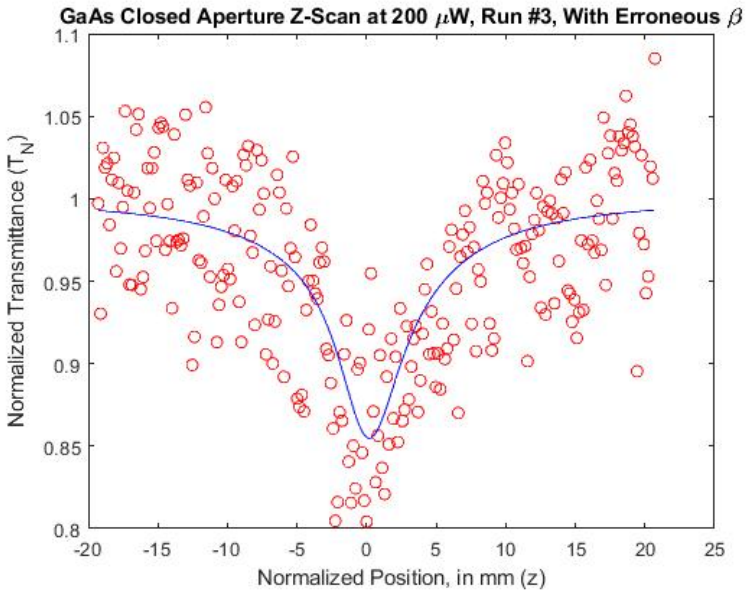

Figure 106: GaAs closed aperture Z-Scan Run #2 at 200 μW with unrealistic two photon absorption coefficient. The red circles are the collected data, and the blue line is the fit Equation 80.

4.5 ZnSe Closed Aperture Z-Scan Runs

There were two ZnSe CA runs accomplished: one at 1 mW and one at 4 mW. Figure 107 shows the run completed at 1 mW. The graph is relatively flat but very noisy, with no side being noticeably higher than the other as expected in a CA run. Thus, this graph suggests that ZnSe has at 1550 nm an n_2 value within the noise. However, Figure 108 shows that ZnSe does have a significant n_2 value at 1550 nm, but it requires a higher intensity to detect it.

The second CA run increased the pump average power to 4 mW. The fit shown in Figure 108 uses a β of 0 cm/GW, an α of 0.1676 cm^{-1}, and the same w_0 value of 36.59 μm as the GaAs CA runs performed prior to the ZnSe CA runs. Interestingly, this fit results in an n_2 value of 1.196×10^{-5} cm^2/GW, close to the theoretical value of 10^{-5} cm^2/GW, [49].

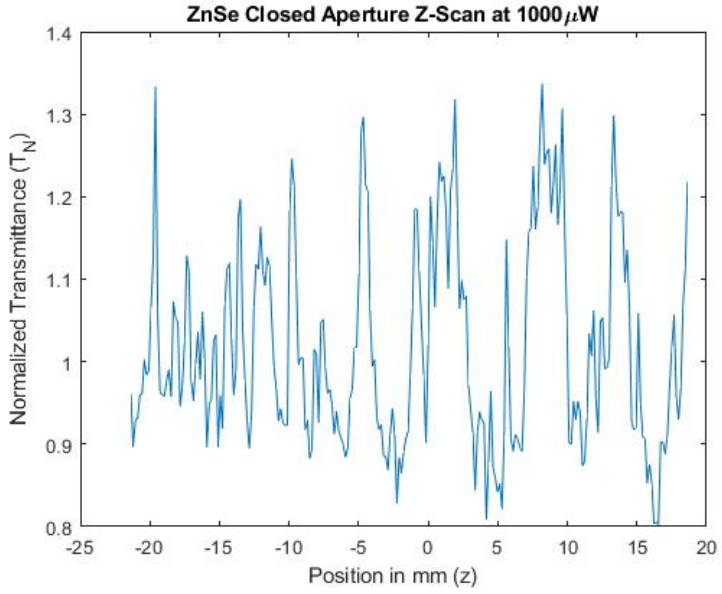

Figure 107: ZnSe closed aperture Z-Scan run at 1000 μW.

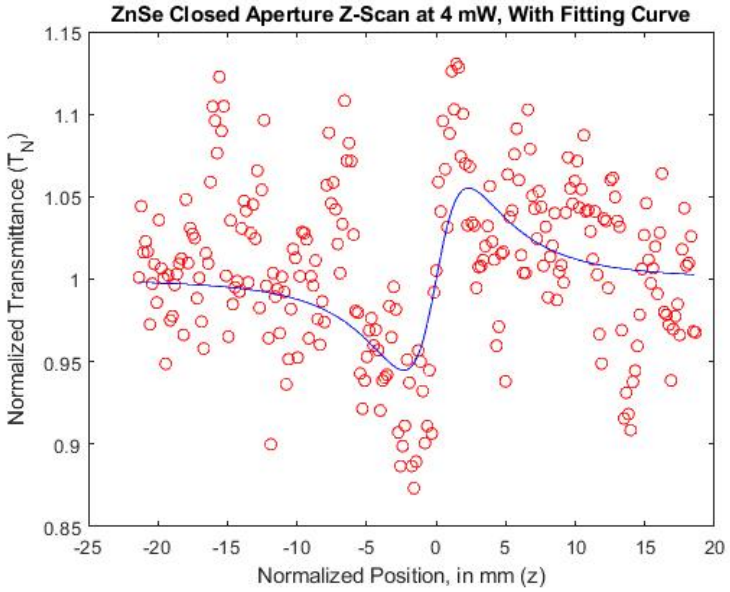

Figure 108: ZnSe closed aperture Z-Scan run at 4000 μW. The red circles are the collected data, and the blue line is the fit Equation 80.

Bibliography

1. P. F. McManamon and A Ataei. "Progress and Opportunities in the Development of Nonmechanical Beam Steering for Electro-optical Systems". *Opt. Eng.*, 58(1), 2019.

2. Y. Leng. *Materials Characterization: An Introduction to Microscopic and Spectroscopic Methods*. Wiley-VCH Verlag GmbH & Co., 2nd edition, 2013.

3. Michael Susner. Research Materials Engineeer, AFRL/RXAPE, Wright-Patterson Base OH. Personal Correspondence. 13 July 2021.

4. Peter E. Powers and Joseph W. Haus. *Fundamentals of Nonlinear Optics*. CRC Press: Taylor and Francis Group, 2nd edition, 2017.

5. W. C. Hurlbut, K. L. Vodopyanov, P. S. Kuo, M. M. Fejer, and Yun-Shik Lee. "Multi-photon absorption and nonlinear refraction of GaAs in the mid-infrared". *Optics Letters*, 32(6):668–670, 2007.

6. Robert C Hoffman and Andrew G Mott. "Measurement of the Two-photon Absorption Coefficient of Gallium Phosphide (GaP) Using a Dispersion-minimized Sub-10 Femtosecond Z-scan Measurement System". *Army Research Laboratory*, ARL-TR-615(September):1–18, 2012.

7. J. H. Bechtel and W. L. Smith. "Two-photon absorption in semiconductors with picosecond laser pulses". *Physical Review B*, 13(8):3515–3522, 1976.

8. Ichiro Shoji, Takashi Kondo, Ayako Kitamoto, Masayuki Shirane, and Ryoichi Ito. "Absolute scale of second-order nonlinear-optical coefficients". *Journal of the Optical Society of America B*, 14(9):2268–2294, 1997.

9. T. Skauli, K. L. Vodopyanov, T. J. Pinguet, A. Schober, O. Levi, L. A. Eyres, M. M. Fejer, J. S. Harris, B. Gerard, L. Becouarn, E. Lallier, and G. Arisholm. "Measurement of the nonlinear coefficient of orientation-patterned GaAs and demonstration of highly efficient second-harmonic generation". *Optics Letters*, 27(8):628, 2002.

10. A. A. Said, M. Sheik-Bahae, D. J. Hagan, T. H. Wei, J. Wang, J. Young, and E. W. Van Stryland. "Time-resolved Z-scan measurements of optical nonlinearities". *Journal of Optical Society of America B*, 9:405, 1992.

11. D. Haertle, M. Jazbinsek, G. Montemezzani, and P. Gunter. Nonlinear optical coefficients and phase-matching conditions in Sn2P2S6. *Optics Express*, 13(10):3765–3776, 2005.

12. E. Hecht. *Optics*. Pearson Education, Inc., 5th edition, 2017.

13. W. Callister and D. Rethwisch. *Materials Science and Engineering: An Introduction*. John Wiley & Sons, Inc., 8th edition, 2010.

14. Rüdiger Paschotta. "Conflicting Definitions of s & p Polarizations". *RP Photonics AG*, 3 March 2012. Retrieved on 3 March 2022.

15. J. A. Bastin, E. W. J. Mitchell, and J. Whitehouse. "Use of an Integrating Sphere to Distinguish Between Absorption and Scattering in Solids". *British Journal of Applied Physics*, 10:412–416, 1959.

16. D. A. Kleinman. "Nonlinear Dielectric Polarization in Optical Media". *Physical Review*, 126(6):1977–1979, 1962.

17. George F. Koster et al. *Properties of the Thirty-Two Point Groups*. M.I.T. Press, Cambridge, MA, 1st edition, 1963.

18. C. Giacovazzo et al. *Fundamentals of Crystallography.* Oxford University Press, 3rd edition, 2011.

19. B.E. Douglas et al. *Concepts and Models of Inorganic Chemistry.* John Wiley & Sons, Inc., 3rd edition, 1994.

20. Robert C Miller. "Optical Second Harmonic Generation in Piezoelectric Crystals". *Applied Physics Letters*, 5(1):17–19, 1964.

21. R.C Miller, W. A. Nordland, and P. M. Bridenbaugh. "dependence of second-harmonic-generation coefficients of linbo$_3$ on melt composition". *Journal of Applied Physics*, 42:4145–4147, 1971.

22. Joel Murray. Research Physicist, AFRL/RX, Wright-Patterson Base OH. Personal Correspondence. 24 January 2022.

23. Mansoor Sheik-Bahae, Ali A. Said, Tai Huei Wei, David J. Hagan, and E. W. Van Stryland. "Sensitive Measurement of Optical Nonlinearities Using a Single Beam". *IEEE Journal of Quantum Electronics*, 26(4):760–769, 1990.

24. M Sheik-Bahae, A.A. Said, and E.W. Van Stryland. "High-Sensitivity, Single-Beam n_2 Measurements". *Optics Letters*, 14(17):955, 1989.

25. P. D. Maker, R. W. Terhune, M. Nisenoff, and C. M. Savage. "Effects of Dispersion and Focusing on the Production of Optical Harmonics". *Physical Review Letters*, 8(1):21–22, 1962.

26. N. Bloembergen and P. S. Pershan. "Light Waves at the Boundary of Nonlinear Media". *Physical Review*, 128(2):606–622, 1962.

27. J. Jerphagnon and S. K. Kurtz. "Maker Fringes: A Detailed Comparison of Theory and Experiment for Isotropic and Uniaxial Crystals". *Robotics and Automation Magazine*, 41(4):1667–1681, 1970.

28. P. Pavlides and D. Pugh. "General Theory of Maker Fringes in Crystals of Low Symmetry". *Journal of Physics: Condensed Matter*, 3(8):967–988, 1991.

29. Warren N. Herman and L. Michael Hayden. "Maker Finges Revisited: Second-Harmonic Generation from Birefringent or Absorbing Materials". *Journal of the Optical Society of America B*, 12(3):416–427, 1995.

30. Joel M. Murray, Research Physicist, Air Force Research Laboratory. "Observation of second-harmonic reflection." Photonics West. San Fransisco CA. 6 Februrary 2019.

31. T. Skauli, P. S. Kuo, K. L. Vodopyanov, T. J. Pinguet, O. Levi, L. A. Eyres, J. S. Harris, M. M. Fejer, B. Gerard, L. Becouarn, and E. Lallier. "Improved dispersion relations for GaAs and applications to nonlinear optics". *Journal of Applied Physics*, 94(10):6447–6455, 2003.

32. Eric W. Van Stryland and Mansoor Sheik-Bahae. "Z-scan Measurements of Optical Nonlinearities". *Characterization Techniques and Tabulations for Organic Nonlinear Materials*, pages 655–692, 1998.

33. Marco Vivacqua, Daniel Espinosa, and Antônio Martins Figueiredo Neto. "Application of the Z-scan Technique to Determine the Optical Kerr Coefficient and Two-photon Absorption Coefficient of Magnetite Nanoparticles Colloidal Suspension". *Journal of Applied Physics*, 111(113509):1–5, 2012.

34. Michael D. Harm. *Development of a TM:HO:YLF-Laser-Pumped-Orientation-Patterned Gallium Arsenide Optical Parametric Oscillator.* MS Thesis,

AFIT/GEO/ENP/02-01. Graduate School of Engineering and Management, Air Force Institute of Technology (AU), Wright-Patterson Base OH, March 2002.

35. "Gallium Arsenide (GaAs)". *Crystan Ltd.*, 2012. Retrieved on 2 March 2022.

36. J. Václavík and D. Vápenka. "Gallium Phosphide as a material for visible and infrared optics". *EPJ Web of Conferences*, 48:1–4, 2013.

37. Jean Wei, Joel M. Murray, Jacob O. Barnes, Douglas M. Krein, Peter G. Schunemann, and Shekhar Guha. "Temperature dependent Sellmeier equation for the refractive index of GaP". *Optical Materials Express*, 8(2):485–490, 2018.

38. Kelley Rivoire, Ziliang Lin, Fariba Hatami, W. Ted Masselink, and Jelena Vučković. "Second harmonic generation in gallium phosphide photonic crystal nanocavities with ultralow continuous wave pump power". *Optics InfoBase Conference Papers*, 17(25):22609–22615, 2009.

39. Dalziel J Wilson, Katharina Schneider, Simon Hönl, Miles Anderson, Yannick Baumgartner, Lukas Czornomaz, Tobias J Kippenberg, and Paul Seidler. "Integrated gallium phosphide nonlinear photonics". *Nature Photonics*, 14:57–62, 2020.

40. A. R. Denton and N. W. Ashcroft. "Vegard's Law". *Physical Review A*, 43(6):3161–3164, 1991.

41. A. Anema, A.A. Grabar, and Th. Rasing. "The Nonlinear Optical Properties of $Sn_2P_2S_6$". *Ferroelectrics*, 183:181–183, 1996.

42. Zhuang Li, Jiyong Yao, and Yicheng Wu. "Chalcophosphates: A Treasure House of Infrared Nonlinear Optical Materials". *Crystal Growth and Design*, 20(11):7550–7564, 2020.

43. D. Haertle, G. Caimi, A. Haldi, G Montemezzani, P. Gunter, A.A. Grabar, I.M. Stoika, and Yu.M. Vysochanskii. "Electro-Optical Properties of $Sn_2P_2S_6$". *Optics Communications*, 215:333–343, 2003.

44. C. D. Carpentier and R. Nitsche. "Vapour Growth and Crystal Data of the Thio(Seleno)-Hypodiphosphates $Sn_2P_2S_6$, $Sn_2P_2Se_6$, $Pb_2P_2S_6$, $Pb_2P_2Se_6$ and Their Mixed Crystals". *Mat. Res. Bull*, 9:401–410, 1974.

45. D. Haertle, A. Guarino, J. Hajfler, G. Montemezzani, and P. G¨nter. "Refractive indices of $Sn_2P_2S_6$ at visible and infrared wavelengths". *Optics Express*, 13(6):2047, 2005.

46. E. M. Gavrushchuk. "Polycrystalline zinc selenide for IR optical applications". *Inorganic Materials*, 39(9):883–899, 2003.

47. William J. Tropf. "Temperature-dependent refractive index models for BaF_2, CaF_2, MgF_2, SrF_2, LiF, NaF, KCI, ZnS, and ZnSe". *Optical Engineering*, (5):1369–1373, 1995.

48. I. Shoji, T. Kondo, and R. Ito. "Second-order nonlinear susceptibilities of various dielectric and semiconductor materials". *Optical and Quantum Electronics*, 34(8):797–833, 2002.

49. Magali Durand, Aurélien Houard, Khan Lim, Anne Durécu, Olivier Vasseur, and Martin Richardson. "Study of filamentation threshold in zinc selenide". *Optics Express*, 22(5):5852–5858, 2014.

50. Qianliang Li, Walter Perrie, Zhaoqing Li, Stuart P Edwardson, and Geoff Dearden. "Two-photon absorption and stimulated emission in poly-crystalline Zinc Selenide with femtosecond laser excitation". *Opto-Electronic Advances*, 5(1):1–12, 2022.

51. Bum Ku Rhee, Jin Seob Byun, and E. W. Van Stryland. "Z scan using circularly symmetric beams". *Journal of the Optical Society of America B*, 13(12):2720, 1996.

52. M. Yin, H.P. Li, S.H. Tang, and W. Ji. "Determination of nonlinear absorption and refraction by single Z-scan method". *Applied Physics B: Lasers and Optics*, 70(4):587–591, 2000.

53. Vladimir Tassev. Senior Research Physicist, AFRL/RY, Wright-Patterson Base OH. Personal Correspondence. 18 January 2022.

54. Xin Yin, Shaojun Zhang, and Zhaobing Tian. "Refractive indices of biaxial crystals evaluated from the refractive indices ellipsoid equation". *Optics and Laser Technology*, 39(3):510–513, 2007.

Acronyms

2PA two photon absorption. 31

AFRL Air Force Research Laboratory. 6

CA closed aperture. 40

DFG Difference Frequency Generation. 3

DoD Department of Defense. 1

e-waves extraordinary waves. 16

EO electro-optical. 6

FWHM Full Width Half Max. 13

GaAs gallium arsenide. 1

GaP gallium phosphide. 1

LWIR long-wave IR. 2

MWIR mid-wave IR. 2

NLO nonlinear optics. 4

OA open aperture. 40

o-waves ordinary waves. 16

OPA Optical Parametric Amplification. 3

OPG Optical Parametric Generation. 3

QPM quasi-phase matching. 29

SFG Sum Frequency Generation. 3

SHG Second Harmonic Generation. 3

SWIR short-wave IR. 2

REPORT DOCUMENTATION PAGE

Form Approved
OMB No. 0704–0188

1. REPORT DATE *(DD–MM–YYYY)*	2. REPORT TYPE	3. DATES COVERED *(From — To)*
22–03–2022	Master's Thesis	Sept 2020 — Mar 2022

4. TITLE AND SUBTITLE

Determination of Nonlinear Optical Properties for Gallium Arsenide Phosphide Ternary Compounds and for Tin Thiohypodiphosphate

5a. CONTRACT NUMBER

5b. GRANT NUMBER

5c. PROGRAM ELEMENT NUMBER

6. AUTHOR(S)

Peter F. Norris

5d. PROJECT NUMBER

5e. TASK NUMBER

5f. WORK UNIT NUMBER

7. PERFORMING ORGANIZATION NAME(S) AND ADDRESS(ES)

Air Force Institute of Technology
Graduate School of Engineering and Management (AFIT/EN)
2950 Hobson Way
WPAFB OH 45433-7765

8. PERFORMING ORGANIZATION REPORT NUMBER

AFIT-ENG-MS-22-M-051

9. SPONSORING / MONITORING AGENCY NAME(S) AND ADDRESS(ES)

Air Force Research Laboratory
Sensor's Directorate
2241 Avionics Circle
WPAFB OH 45433-7765

10. SPONSOR/MONITOR'S ACRONYM(S)

AFRL/RYDH

11. SPONSOR/MONITOR'S REPORT NUMBER(S)

12. DISTRIBUTION / AVAILABILITY STATEMENT

DISTRIBUTION STATEMENT A:
APPROVED FOR PUBLIC RELEASE; DISTRIBUTION UNLIMITED.

13. SUPPLEMENTARY NOTES

14. ABSTRACT

The Department of Defense and the commercial sector rely on coherent light sources to emit light that transmits through the atmosphere. Nonlinear optical effects in crystalline materials can be used to generate the laser waves, but certain nonlinear effects negatively impact the performance of laser generating materials. This thesis focuses on characterizing nonlinear optical properties for gallium arsenide phosphide ternary compounds and for tin thiohypodiphosphate. The Maker Fringe experiment is used to determine the d-coefficients of the materials, which describe the magnitude of the nonlinear response of the material. The Z-Scan experiment is used to calculate the nonlinear refractive index and the two photon absorption of the material. This thesis summarizes the pertinent theory surrounding nonlinear optics and the characterization experiments. The Maker Fringe experiment was constructed and verified as a part of this thesis, allowing the setup to be used for future research. The gallium arsenide phosphide ternary compounds were demonstrated to be able to frequency convert. $Sn_2P_2S_6$ was demonstrated to not have appreciable two photon absorption at 1550 nm.

15. SUBJECT TERMS

Nonlinear optics, linear optics

16. SECURITY CLASSIFICATION OF:			17. LIMITATION OF ABSTRACT	18. NUMBER OF PAGES	19a. NAME OF RESPONSIBLE PERSON
a. REPORT	b. ABSTRACT	c. THIS PAGE			Lt Col James M. Sattler, AFIT/ENG
U	U	U	UU	166	19b. TELEPHONE NUMBER *(include area code)* (937) 255-3636 x 4382; james.sattler@afit.edu